Thesis for the Degree of Doctor of Philosophy

Cryogenic thermal noise behavior in release-free optomechanical crystals

Johan Kolvik



CHALMERS

Quantum Technology Laboratory
Department of Michrotechnology and Nanoscience (MC2)
Chalmers University of Technology
Göteborg, Sweden, 2026

Cryogenic thermal noise behavior in release-free optomechanical crystals
Johan Kolvik

©Johan Kolvik, 2026

Acknowledgements, dedications, and similar personal statements in this thesis, reflect the author's own views.

ISBN 978-91-8103-478-3
Doktorsavhandlingar vid Chalmers tekniska högskola
Ny serie nr 5935
ISSN 0346-718X

Chalmers University of Technology
Michrotechnology and Nanoscience (MC2)
Quantum Technology Laboratory
SE-412 96 Göteborg, Sweden
Phone: +46 (0) 31 772 1000

Front cover illustration: *Foreground*: Release-free optomechanical crystal. *Background*: Optical fiber-chip coupler consisting of angle-cut fiber and on-chip grating coupler.

Printed in Sweden by
Reproservice
Chalmers University of Technology
Göteborg, Sweden, September 2026

To you, somewhere beyond the sea...

Cryogenic thermal noise behavior in release-free optomechanical crystals

Johan Kolvik
Quantum Technology Laboratory
Department of Michrotechnology and Nanoscience (MC2)
Chalmers University of Technology

Abstract

Noise is an ever-present reality of the world we live in. From the non-deterministic movement of matter to the fluctuations of the physical fields surrounding us, noise is the ultimate adversary of all things pure. Noise limits the fidelity of information transfer, particularly for quantum signals relying on coherence. Yet at sufficiently low temperatures, ambient thermal noise is suppressed to a level where even quantum signals can maintain coherence, making them available for technological applications. Modern cryogenic technologies enable access to environmental temperatures of 10 mK, allowing quantum-coherent transfer and processing of signals with carrier frequencies in the GHz range.

A technology that operates in this regime is the optomechanical crystal: a nanofabricated device that supports high-quality resonances for both optical and acoustic fields and enables coherent coupling between the two. Through the optomechanical interaction, the acoustic mode can serve as a universal bus for the optical field, coherently linking it to other nonlinear systems, such as superconducting qubits – thereby enabling quantum microwave-to-optical transduction. As with many quantum systems, however, device performance is constrained by excess noise. In optomechanical crystals, this noise primarily stems from optical absorption combined with insufficient thermal anchoring. Achieving robust quantum-level operation in future devices therefore requires a detailed understanding and careful mitigation of these noise mechanisms.

This thesis makes progress toward overcoming optical-absorption-induced noise in optomechanical crystals by (I) introducing a new class of optomechanical devices with superior thermal anchoring: the *release-free* optomechanical crystal; and (II) carefully investigating its noise performance and potential for microwave-to-optical transduction. The results presented in this thesis contribute to the understanding of noise limits in silicon optomechanical crystals and showcase the release-free platform as a viable alternative for on-chip, low-noise optomechanics.

Keywords: Release-free silicon optomechanical crystal, optomechanics, cryogenic silicon thermometry, single-phonon counting.

Acknowledgement

What an extraordinary journey it's been. When attempting to look back on this experience, many simultaneous feelings and impressions flood the senses, making it hard to properly sift through and make sense of it all. Only one thing is certain: finishing this thesis would have been hopeless weren't it for all the help I've received along the way. In the following, I will attempt the impossible and thank everyone that made the path of the PhD walkable.

First and foremost, I give my warmest thanks to my family. Being there to offload when things look grim is one thing, but what's more is providing me with the unyielding notion that I'm supported in whatever I do. Me pursuing science was never the goal. That freedom set me on my own path – one that I look forward to keep treading in years to come.

Next, I thank everyone that got me into science. Although an intrinsic curiosity has always been with me, proper catalysis have been crucial for sparking my scientific courage. To that end, I thank everyone in the LB-gang, with special mentions to Ludvig and Carl with whom I found my academic footing. I also thank the Wieczorek lab which during the writing of my master thesis was my first point of contact with research. A special thanks to Witlef without whom I might not have applied for the PhD position and who continues to inspire to this day.

Building a laboratory from scratch is an adventure that few PhD students have the privilege to experience, but it's simply not possible without help. I thus thank the fantastic MC2 staff which helped the lab along the way: Ximena on facilities, Karin on invoicing and procurements (and lost power meters), Ulf and Martin on IT, Lars who's always ready

by the CNC machine, and the NFL staff with special mentions to Niclas, Petra, Mattias, and Mats who disarmed the dangers of the cleanroom.

I also want to thank the friends, organizations and colleagues who accepted me when being stuck in the lab and helped me take much needed breaks. Gosskören, Vers och Bärs, Spex, and Scrubben among others got me out of the lab; the QT mechanics group brought great lunches; and the colleagues at photonics were always a delight at the yearly kick-offs. Among the MC2 colleagues, I send special mentions to Awse for great travel company, Rasmus for unpacking quantum noise limits with me, and Erik with whom I shared the PhD home stretch – Kör hårt!

While on the topic of the PhD home stretch, I especially thank those who helped me get my PhD through the door. Thanks to Per Lundgren for understanding, Malin for organizing, Per Delsing for guidance, and Victor for approval. You made the last stretch possible. Here, I also extend another thanks to Witlef for his support to the group during the last months of my PhD.

With that I've come to the group. The team. QPL. Building this lab together is the proudest achievement of my professional career – writing this thesis is a close second. Setting up hardware and processes for research longevity has been a priceless experience and a true privilege while sharing it with you. Thanks to our postdocs: Liza, Pooja, and Mads, among whom I'm especially grateful to Mads. Thanks for reviewing the thesis, being there when I needed support, and for the great optomechanics discussions. Thanks next to David who taught me proper code and to Ebba for your enthusiasm. I wish both of you the best of luck.

Now to my closest peers. To Trond, thanks for sharing my office and for enthusiastically engaging in quantum physics discussions way over my head. To Joey, thanks for being there from the start. Your diligence and curiosity is unparalleled. To Paul, without you there would be no thesis. I will be forever grateful for your review of the thesis manuscript and for all you've done for the lab and our research. Finally, to Raphaël, thanks for trusting me with your first hire and for teaching me how to do proper research – if only it could last forever. I wish you all the best and look forward to seeing what bright futures you have in store.

Johan Kolvik
Göteborg, September 2026

Declaration of Transparency

This thesis was written by myself based on research conducted in a collaborative research environment. During the writing of the thesis, AI-powered spell- and grammar checking tools were used to revise the manuscript. Generative AI was allowed to give feedback on thesis prose which at times guided writing. Generative AI was occasionally used to write research-related code but was not used to generate data, figures or analysis.

Johan Kolvik
Göteborg, September 2026

Publications

This thesis is based on the work contained in the following papers:

[A] **Johan Kolvik**, Paul Burger, Joey Frey, Raphaël Van Laer, "Clamped and sideband-resolved optomechanical crystals", *Optica* **10**, 913-916, June, 2023. DOI: 10.1364/OPTICA.492143

[B] **Johan Kolvik**, Paul Burger, David Hambraeus, Trond H. Haug, Joey Frey, Mads. B. Kristensen, Raphaël Van Laer, "Optomechanical crystal in light-resilient quantum ground state", Preprint at `https://arxiv.org/abs/2510.15724`, October, 2025.
Manuscript submitted.

[C] Paul Burger, Joey Frey, **Johan Kolvik**, Raphaël Van Laer, "Release-free electro-optomechanical crystal modulator", *Optics Letters* **51**, 3886-3889, July, 2026. DOI: 10.1364/OL.597343

Other author contributions, not included in this thesis:

[D] Paul Burger, **Johan Kolvik**, Joey Frey, Raphaël Van Laer, "A transducer arrangement and a method for fabricating said transducer arrangement" *Swedish patent* SE2350347-7, March, 2023.

[E] Paul Burger, Joey Frey, **Johan Kolvik**, David Hambraeus, Raphaël Van Laer, "Design of a release-free piezo-optomechanical quantum transducer" *APL Photonics* 10, 010801, January, 2025.
DOI: 10.1063/5.0246075

Conference contributions by the author, not included in this thesis:

[F] **Johan Kolvik**, Paul Burger, David Hambraeus, Trond H. Haug, Joey Frey, Mads. B Kristensen, Raphaël Van Laer, "Light-resilient ground state operation in a release-free optomechanical crystal" *CLEO 2026* ATH4C.3, May, 2026.
DOI: 10.1364/CLEO_AT.2026.ATH4C.3

Acronyms

AOM	Acousto-optic modulator
BAW	Bulk acoustic wave
BOX	Buried oxide
BSBS	Backward stimulated Brillouin scattering
CME	Coupled mode equation
CW	Continuous wave
DUT	Device under test
ECDL	External cavity diode laser
EDA	Electronic defect absorption
EDFA	Erbium-doped fiber amplifier
EIT	Electromagnetically induced transparency
EMC	Electromechanical crystal
EOM	Electro-optic modulator
ESA	Electrical spectrum analyzer
FCA	Free carrier absorption
FGA	Forming gas annealing
FP	Fabry–Pérot
FSBS	Forward stimulated Brillouin scattering
FSR	Free spectral range
FWHM	Full-width-half-maximum
HF	Hydrofluoric acid
HSPD	High-speed photo-detector
ICP	Inductively coupled plasma
IL	Insertion loss

ITR	Interfacial thermal resistance
LN	Lithium-niobate
MB	Moving boundary
MEMS	Micro-electromechanical system
MFP	Mean-free-path
MO	Microwave-to-optical
MXC	Mixing chamber
OMC	Optomechanical crystal
PE	Photoelasticity
RF	Radio-frequency
RIE	Reactive ion etching
RWA	Rotating wave approximation
SAW	Surface acoustic wave
SNSPD	Superconducting nanowire single-photon detector
SOI	Silicon-on-insulator
SOS	Silicon-on-sapphire
SPDC	Spontaneous parametric down-conversion
TEM	Transmission electron microscopy
TIR	Total-internal-reflection
TLS	Two-level system
TPA	Two-photon absorption
VNA	Vector network analyzer
VOA	Variable optical attenuator
WGM	Whispering gallery mode

Contents

Abstract **v**

Acknowledgement **vi**

Declaration of Transparency **ix**

Publications **x**

Acronyms **xii**

1 Introduction **1**
1.1 Micro- and nanoscale mechanical elements 1
1.1.1 Light-interacting mechanical elements 2
1.2 The optomechanical crystal cavity 3
1.2.1 Microwave-to-optical transduction 4
1.2.2 Optical-absorption-induced thermal noise 5
1.3 This thesis 6

2 Interaction between light and nanoscale motion **9**
2.1 Optical and acoustic waves 10
2.1.1 Optical waves 10
2.1.2 Acoustic waves 11
2.1.3 Optical forces 13
2.2 Brillouin scattering 15
2.2.1 Interaction-free Hamiltonians 16

2.2.2 Interaction Hamiltonians . . . 18
2.2.3 Full dynamics . . . 19
2.3 Cavity optomechanics . . . 20
2.3.1 Cavity optomechanical Hamiltonians . . . 21
2.3.2 Coupling to thermal baths . . . 23
2.3.3 Cavity optomechanical dynamics . . . 23
2.3.4 Symmetries between optomechanical pictures . . . 25
2.4 Optomechanical consequences . . . 26
2.4.1 Thermomechanical scattering . . . 26
2.4.2 Optomechanical back-action . . . 29
2.4.3 Electromagnetically induced transparency . . . 30
2.4.4 Sideband asymmetry . . . 34

3 The release-free optomechanical crystal 37
3.1 Design . . . 38
3.1.1 Total internal reflection for acoustic waves . . . 38
3.1.2 Unpatterned release-free optomechanical waveguides 39
3.1.3 Patterned waveguides and the pinch mode . . . 42
3.1.4 Release-free optomechanical crystal cavities . . . 46
3.2 Fabrication . . . 48
3.2.1 Silicon dry-etching . . . 49
3.3 Room-temperature measurements . . . 53
3.3.1 Optical properties . . . 54
3.3.2 Mechanical properties . . . 55
3.3.3 Disorder in longer devices . . . 56

4 Laser-induced thermal noise at cryogenic temperatures 59
4.1 Laser-induced thermal noise . . . 60
4.1.1 Optical absorption in silicon . . . 60
4.1.2 Hot-bath model . . . 62
4.1.3 Phonon transport at millikelvin temperatures . . . 65
4.1.4 Thermal phonon dynamics . . . 68
4.1.5 The thermo-optic effect . . . 70
4.2 Measurement setup . . . 70
4.2.1 Dilution refrigerator setup . . . 71
4.2.2 Phase noise and pump filtering . . . 72
4.2.3 Single-photon detection and excess noise . . . 75
4.2.4 Acousto-optic pulsing . . . 77
4.3 Supplementary thermometry results . . . 77
4.3.1 Silicon-on-sapphire optical nonlinearities . . . 78

4.3.2 Silicon-on-sapphire continuous-wave noise 79
4.3.3 Silicon-on-sapphire ringdown 81
4.3.4 Suspended pinch-mode OMC 82

5 Release-free piezo-optomechanical transducer 87
5.1 Background 88
5.1.1 Phonons as transduction intermediaries 88
5.1.2 Piezoelectricity 89
5.2 Transducer theory 89
5.2.1 Piezo-optomechanical Hamiltonian 89
5.2.2 Transducer scattering parameters 90
5.3 Design 94
5.4 Room-temperature transduction 95
5.4.1 Continuous-wave microwave-to-optical transduction 96
5.4.2 Classical signal transmission 97

6 Conclusion & Future outlook 101

7 Summary of papers 105

A Supplementary Brillouin scattering theory 109
A.1 Amplitude envelope operators 109
A.2 Full scattering dynamics 110

B Supplementary derivations 113
B.1 Mathematical conventions 113
B.2 Solutions to the cavity optomechanical CMEs 114
B.3 Brillouin gain in 2D simulations 115
B.4 Unit cell optomechanical coupling 116
B.5 Phonon dynamics with thermal drive 117

Appended papers 129

CHAPTER 1

Introduction

1.1 Micro- and nanoscale mechanical elements

In an age increasingly defined by software, data, and artificial intelligence, the significance of technologies based on physical motion is easily overlooked. At the dawn of the computing age, Charles Babbage envisioned the Analytical Engine: an all-purpose computer with working principles based on the motion of mechanical elements, long before the invention of electricity-based transistors [1]. While never fully completed, the massive machine with its thousands of gears and levers would be a magnificent sight to behold – even now almost two centuries later.

The mechanical elements of today can be significantly more subtle, and some are integral to the technologies we interact with daily. Micro-electromechanical systems (MEMS) using micro-sized mechanical elements are widely applied in systems such as accelerometers in phones and satellites [2], beam-steering LiDAR for automotive [3], and filters for compact RF signal processing [4]. Mechanical elements are unique in their ability to interact strongly with many other physical systems, often thanks to the properties of the materials constituting the mechanical element's moving parts. Gravity pulls on anything with mass and magnetic materials are accelerated by magnetic fields, just to name a few. Oscillating electromagnetic fields such as optical light also affect objects' motion. This is described in the field of physics called *optomechanics*.

1.1.1 Light-interacting mechanical elements

Optomechanics details the interplay between optical light and the movement of mechanical objects. While dependent on the intensity of the interacting light, the optomechanical interaction is strongest when light is highly concentrated in tiny regions of space – making it especially interesting for micro- and nanoscale systems. A common application where light is tightly confined to a small region is the optical fiber. A single-mode optical fiber core for laser light with 1550 nm wavelength has a diameter on the order of a few micrometers, and when optical powers are high, light sometimes scatters off the thermal vibrations in the core in a process related to optomechanics called Brillouin scattering [5] (Fig. 1.1a). Brillouin scattering affects the transmitted power and spectral features of propagating light and can be regarded as both a desirable effect and an unintended nuisance. Since the first reported measurements in silica glass optical fibers [6], fiber-optic Brillouin scattering has been studied in many more exotic fiber systems with examples such as chalcogenide photonic crystal fibers [7] and liquid core fibers [8].

The rise of nanofabrication in the 21st century brought a new playing ground to the field of optomechanics [9]. The novel techniques allowed for microscale mechanical resonators with high frequencies and quality factors to be combined with optical cavities. Micro-scale mirrors on vibrating cantilevers [10] and membranes [11] could act as end mirrors in Fabry–Pérot cavities (Fig. 1.1b), while whispering-gallery mode resonators [12, 13, 14] confined optical and acoustic energy to microscale discs for increased interaction rates (Fig. 1.1c). From these resonant systems, the field of cavity optomechanics emerged in which light could be used to manipulate the state of mechanical motion. Through optomechanics, effects such as cooling of mechanical modes were observed [13, 11], further promising quantum-level operation in future implementations. The quantum regime was later breached in a microwave optomechanical system where GHz microwaves cooled a superconducting microscale drum capacitor close to its quantum ground state [15].

The list of micro- and nanoscale optomechanical systems is long, and every implementation has unique opportunities, strengths, and challenges [17]. However, the ever-present pursuit toward increased sensitivities calls for higher interaction rates, which are often achieved through more tightly confined optical and mechanical fields. The next advancement in 1550 nm nanoscale optomechanical systems thus took this concept one step further.

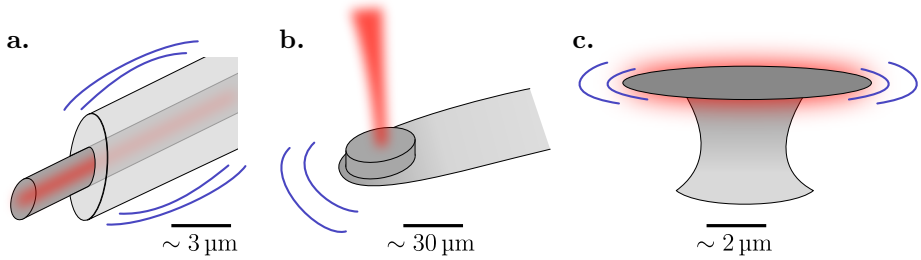


Figure 1.1: Simple schematics of systems with microscale mechanical elements interacting with light (red glow). Vibrational motion indicated in purple. **a.** Vibrations in the core material of optical fibers cause the guided light to scatter in an effect called Brilouin scattering [6, 7, 8]. **b.** A resonant optomechanical system can be formed with microfabricated membranes or cantilevers. With attached mirrors, the vibrational modes interact with light when implemented as end mirrors in Fabry–Pérot cavities [10, 11]. **c.** Microfabricated whispering-gallery-mode resonators in materials such as silicon confine both light and mechanical vibrations in all three dimensions for increased interaction rates [16].

1.2 The optomechanical crystal cavity

Through the precision of nanofabrication, periodic patterns on the scale of the wavelength of light can be used to precisely tailor the properties of optical waves. This had previously led to photonic crystal cavities which formed localized optical modes in thin dielectric slabs for controlling spontaneous emission in semiconductors [18]. In a natural happenstance, the wavelength of the near-infrared light and sound waves in the dielectric slabs are both on the order of 2 µm – owing to the 5-orders-of-magnitude difference in their propagation speed. This meant that the principles governing the photonic crystal cavity also could apply to acoustic vibrations. By designing simultaneous bandgaps for both optical and acoustic waves in high-index materials such as silicon, the optomechanical crystal cavity (OMC) was formed [19].

With its strong interaction, small mode volumes, and high optical and mechanical quality factors, the OMC has been widely studied in various experimental settings, and many different designs have been proposed to tackle specific problems posed by experimental conditions (Fig. 1.2). The main purpose of a majority of experiments is to use the coherent optomechanical coupling to manipulate the state of the OMC mechanical mode down to the quantum regime – as had been previously shown in the microwave domain [15]. This endeavor has proven fruitful and has

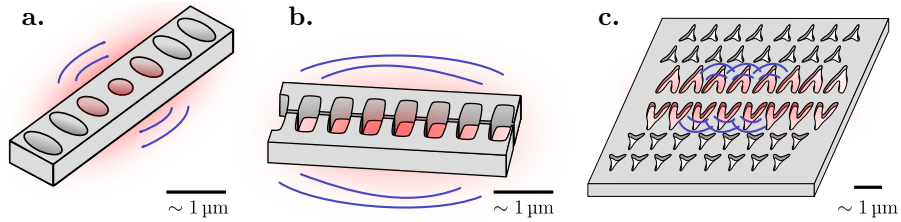


Figure 1.2: Simple schematics of suspended silicon optomechanical crystal cavities (OMCs). Vibrational motion indicated in purple. **a.** Classical suspended nanobeam OMC with elliptical holes. A "breathing"-style GHz mechanical motion couples to light guided within the nanobeam [26, 24, 21]. **b.** "Zipper"-style OMC. The nanobeam is split in half, leaving an air gap along the length of the nanobeam. The thin gap enables record-high coupling to MHz-range mechanical modes but also increases optical losses [27]. **c.** Two-dimensional "b-dagger"-style OMC designed for high coupling and low noise [28].

led to experiments such as laser cooling of GHz mechanical modes close to the quantum ground state [20, 21], remote mechanical entanglement [22], and the study of topological phonons [23], to name a few. The light field can also be manipulated by the interaction to create non-classical states in the optical domain [24, 25].

1.2.1 Microwave-to-optical transduction

The efficient coherent coupling between the near-infrared light and GHz acoustic waves brings opportunities beyond the optomechanical interaction. The prospect of a similarly efficient coupling between 1550 nm optics and GHz *microwaves* offers promises within both classical and quantum technologies [29, 30]. This steers active research into interconnecting devices sometimes referred to as microwave-to-optical (MO) transducers within the field of quantum technology. As direct electro-optical coupling generally requires strong optical pumping to reach appreciable interaction [31, 32], many currently explored approaches use an intermediary physical system as an alternative transduction path. By efficiently interacting with both domains, a multistage process can thus achieve stronger effective coupling between microwave and optical domains [30]. Among explored intermediary systems such as spin waves [33], Rydberg atoms [34, 35], ions [36], and vacancy centers [37, 38], we again find mechanical motion, which, as previously established, has a unique ability to couple strongly to many physical systems – including

optics and microwaves [39].

By functionalizing the OMC with a piezoelectric material, the mechanical mode can be driven by both optical light and GHz microwaves. With previously demonstrated operation in the quantum regime, the OMC-based approach is especially appealing for the quantum technology industry. Qubits realized by superconducting circuits are one of the promising avenues for realizing fault-tolerant quantum computation [40], but they face serious scaling challenges [41] that could be alleviated through remote entanglement achieved through MO transduction [42]. Research into MO transducers based on optomechanics has led to important achievements such as optical readout of superconducting qubits [43, 44] and microwave–optical photon entanglement [45, 46, 47]. But even though prospects for further progress with OMC-based quantum transducers are promising, there is a major challenge that has been hindering progress for OMCs in the quantum domain from the very first experiments: optical-absorption-induced thermal noise.

1.2.2 Optical-absorption-induced thermal noise

For quantum operation of an MO transducer, it is imperative that any thermal excitations are expelled from the system which would otherwise decohere sensitive quantum signals. For devices such as the OMC with its GHz acoustical frequencies, noise primarily enters from the thermal environment of the mechanical mode. Owing to the GHz frequencies, ground state operation can in principle be achieved by using modern cryogenic equipment reaching temperatures of 10 mK. However, when optical light used for operating the devices absorbs in the OMC material, the temperatures quickly rise beyond operational tolerances. For high-fidelity operation, this effect must thus be minimized.

The path toward low mode volumes and high optical and mechanical quality factors had led silicon OMC devices to be designed in a platform based on suspended nanobeams (Fig. 1.2a,b). This resulted in devices with small thermal capacity and limited pathways for efficient thermal conduction away from the optomechanically active region. A suspended nanobeam device would thus be even more susceptible to absorption-induced heating (Fig. 1.3a). Reducing the mechanical isolation by decreasing mechanical quality factors [48] and the designing of two-dimensional suspended OMCs [49, 28] (Fig. 1.2c) are two of the common approaches to this problem which have both shown recent success [50, 28, 25]. Despite this, thermal noise still limits the operation in

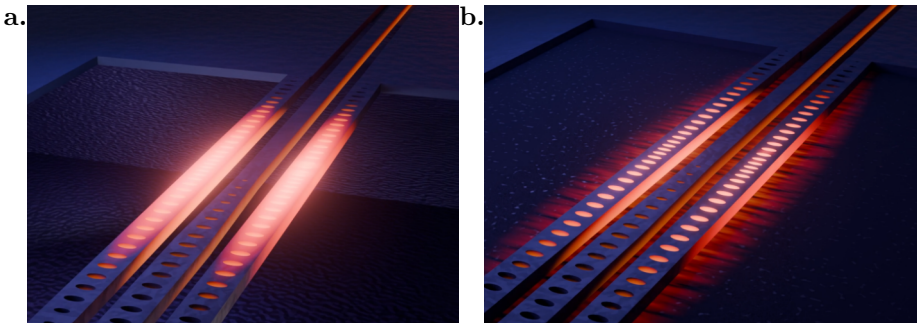


Figure 1.3: Artistic rendition of laser-induced thermal noise in OMCs. **a.** Two suspended OMCs on both sides of a bus waveguide. The device's suspended nature leads to heat buildup on optical pumping illustrated as red-hot glowing. **b.** Adding a substrate beneath the OMCs makes them *release-free*. The generated heat now conducts through the substrate, reducing the heat load on the OMCs at constant applied optical power.

many quantum implementations [50, 25]. This motivates the exploration of other approaches to reduce the effect of absorption-induced thermal noise in optomechanical crystals – bringing us to the contributions of this thesis.

1.3 This thesis

In this thesis, we approach the problem of optical-absorption-induced thermal noise in silicon optomechanical crystals through the exploration of a new design paradigm for silicon OMCs. Through careful design considerations, we fabricate *release-free* OMCs with a working principle that does not rely on suspending the device layer. This type of OMC device would therefore have firmer thermal anchoring to the chip bulk, making it more resistant to thermal noise buildup (Fig. 1.3b). In Paper A, we present a release-free OMC specimen at room temperature with optomechanical coupling $g_{\mathrm{om}}/(2\pi) \approx 500\,\mathrm{kHz}$ and mechanical quality factor limited by thermal scattering. At the time of publication, this was the first sideband-resolved release-free silicon optomechanical system with potential for quantum MO transduction.

In Paper B, we investigate the behavior of laser-induced thermal noise in the release-free devices when cooled down to cryogenic temperatures of 10 mK. We show that when comparing release-free devices to conventional suspended nanobeam OMCs, the release-free devices show

increased robustness to the thermo-optic nonlinearity as well as tolerating significantly more optical power at a constant noise level below one phonon. We further study the time dynamics of the thermal noise in both suspended and release-free OMCs and identify noise components with both fast and slow decay dynamics. Although slowly decaying noise currently limits performance, we run pulsed experiments with average noise < 0.5 phonons at 100 kHz repetition rate and 5 % scattering rate.

With the distant goal of remote entanglement between distant superconducting qubits, we implement a release-free OMC into a full MO transducer and present the results of room temperature measurements in Paper C. With this first-generation device, we measure MO transduction both in continuous wave and pulsed operation with an efficiency limited by the impedance matching to the 50 Ω microwave feedline.

The thesis contributes to the understanding of laser-induced thermal noise in silicon optomechanical systems, a field of research with many currently open questions. With detailed investigations of noise dynamics for both suspended and release-free devices in two distinct material platforms, we provide a perspective that benefits low-noise silicon optomechanics in general – regardless of architectural implementation.

The thesis is outlined as follows: In Chapter 2, we give the background optomechanics and Brillouin scattering theory that is used in design and measurement of release-free OMCs. Chapters 3, 4, and 5 then follow with complementary context, theory, methods, and measurements for Papers A, B, and C, respectively. In Chapter 6, we summarize and conclude the research performed as part of this thesis work and look toward the future of release-free OMCs and MO transducers.

CHAPTER 2

Interaction between light and nanoscale motion

Interaction between light and matter is all around us and is one of the primary media through which we humans observe the universe. Light scattering off physical objects conveys information about the state of matter letting us infer positions and trajectories. This is natural to any living organism with eyes, but that light itself also *affects* the motion of macroscopic objects is harder to imagine. The effect was initially observed by Kepler who in 1619 noted that a comet's tail is repelled by the sun [51], but it was not until the invention of the laser before technological applications could be properly explored. Light's effect on the motion of physical objects is now a widely known phenomenon and is crucial to fields such as nanophotonics and fiber optic communication.

This chapter serves to provide much of the theoretical framework required to understand the results in this thesis with emphasis to provide a solid foundation in the physical mechanisms underpinning the optomechanical interaction. The chapter also describes the fundamental experimental techniques used to gauge a system's optomechanical properties.

2.1 Optical and acoustic waves

At its essence, optomechanics describes the interplay between two physical fields; one expressed in the forces between atoms of matter, and the other in the properties of the electromagnetic field. In this thesis we restrict ourselves by treating the acoustic field in solid matter exclusively, although optomechanics can be studied in other physical systems such as micro- [10, 11, 52] and macroscopic [53] moving mirrors and superfluid helium [54, 55, 56]. Although vastly different in physical appearance, the laws governing the two ingoing fields can be reduced to something near identical, save only for the values of shared properties. This is a beautiful notion that is at the heart of optomechanics, and will be further explored once introducing piezoelectricity in Chapter 5. To appreciate this symmetry, we will begin by giving a basic treatment of the electromagnetic and acoustic fields. While leaving detailed descriptions to masterful works such as those by Griffiths [57] and Auld [58], we proceed more modestly here with general concepts to provide context for further discussion.

2.1.1 Optical waves

We start with the optical part of optomechanics which shares its origin with electricity and interatomic forces as consequences of the electromagnetic field. The field itself is a physical property permeating all space described by the two vector quantities $\vec{E}$ and $\vec{B}$ representing electric field and magnetic field density, respectively. Being two faces of the same physical field, $\vec{E}$ and $\vec{B}$ have an intimate relation, both to each other and to electric charge and current which serve as the field's sources. The interaction is succinctly described in Maxwell's equations:

$$\begin{aligned} \nabla \cdot \vec{E} &= \rho/\varepsilon, \quad & \nabla \times \vec{E} &= -\frac{\partial \vec{B}}{\partial t}, \\ \nabla \cdot \vec{B} &= 0, & \nabla \times \vec{B} &= \mu \vec{J} + \mu\varepsilon \frac{\partial \vec{E}}{\partial t}. \end{aligned} \tag{2.1}$$

In the above – and throughout the thesis – we restrict ourselves to linear, homogeneous and isotropic media with permittivity $\varepsilon = \varepsilon_{\mathrm{r}}\varepsilon_0$. This gives the constitutive relation $\vec{D} = \varepsilon\vec{E}$ where $\vec{D}$ is the electric displacement field. In addition, we have permeability $\mu = \mu_{\mathrm{r}}\mu_0$, charge density ρ, and current density $\vec{J}$. These equations are the foundation to rich fields of physics, and when omitting the source terms $\rho, \vec{J}$, Eqs. (2.1) can be

combined and formed into two separate *wave* equations

$$\nabla^2\vec{E} = \varepsilon\mu\frac{\partial^2\vec{E}}{\partial t^2}, \quad \nabla^2\vec{B} = \varepsilon\mu\frac{\partial^2\vec{B}}{\partial t^2}. \tag{2.2}$$

These equations describe the evolution of the electromagnetic field in time and space as waves propagating with the speed $c = (\varepsilon\mu)^{-1/2}$. Here we also encounter the refractive index, an important material property defined by $n = c_0/c$ where $c_0 = (\varepsilon_0\mu_0)^{-1/2} \approx 3 \cdot 10^8\,\mathrm{m\,s^{-1}}$ is the speed of light given by the permittivity (ε_0) and permeability (μ_0) of vacuum. In a non-magnetic material where $\mu = \mu_0$, the refractive index is given directly by the material's relative permittivity $n = (\varepsilon/\varepsilon_0)^{-1/2} = \sqrt{\varepsilon_r}$.

The wave nature of the electromagnetic field allows it to act as an efficient carrier for information and energy. Sending and receiving information through light or electrical pulses lays the foundation to both how we view the world and much of the technology that we develop. In recent history, the field of photonics has revolutionized how we communicate across the globe. Through the use of optical fibers that cleverly exploit total internal reflection to guide light, fast and long-distance communication is made possible, forming the backbone of the global internet. Even more recently, the power of low-loss and high coherence that optical frequencies provide has been scaled down to chip-size with the rise of nanofabrication; bringing photonics to smartphones and data centers alike.

2.1.2 Acoustic waves

The second part of optomechanics is the one concerning the motion of matter. When thinking about moving objects, it is common to imagine a solid object moving through space with non-zero center-of-mass velocity and acceleration. Although this way of describing the mechanical degree of freedom also leads to the results derived in later sections, we will start this discussion from a more microscopic viewpoint. All solid objects consist of one or several materials which in turn are made up of atoms sitting in a rigid structure. Even if the macroscopic object itself is at rest, the atoms of its materials can move with respect to each other and interact with the electromagnetic waves we introduced previously.

Though all materials consist of discrete and point-like atoms in more or less structured order, it is convenient to treat their motion with continuous fields. When an object deforms, the material volume redistributes in space from its original position. Consider an infinitesimal volume

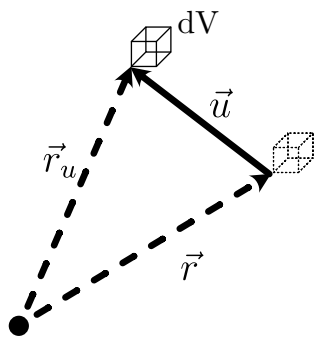


Figure 2.1: The volume dV with displacement $\vec{u}$ is moved from its equilibrium position $\vec{r}$ to the displaced position $\vec{r}_u$.

dV with equilibrium position $\vec{r}$ (Fig. 2.1). When the object deforms, dV moves to a new position $\vec{r}_u$ and we can define its *displacement* $\vec{u} = \vec{r}_u - \vec{r}$. The displacement field $\vec{u}$ serves as the free variable in the study of acoustic motion and is governed by the following relations

$$\begin{aligned} &\varrho \frac{\partial^2 \vec{u}}{\partial t^2} = \nabla \cdot \overline{\sigma} + \vec{F}, && \overline{\sigma} = \overline{\overline{c}} : \overline{S}, \\ &\nabla_{\mathrm{s}} \vec{u} = \overline{S}, && (\nabla_{\mathrm{s}} \vec{f})_{ij} := \frac{1}{2}\left(\frac{\partial f_i}{\partial r_j} + \frac{\partial f_j}{\partial r_i}\right). \end{aligned} \tag{2.3}$$

The top left equation of Eqs. (2.3) is Newton's second law, stating that the acceleration of dV depends on the material's density ϱ, the divergence of the second-order stress tensor $\overline{\sigma}$ and applied force density $\vec{F}$. To find the stress tensor, we use the constitutive relation (top right of (2.3)), which relates stress to the strain $\overline{S}$ through $\overline{\overline{c}}$ which is the fourth-order stiffness tensor[1,2]. Note that we here have omitted viscosity. Finally, $\overline{S}$ links back to the displacement $\vec{u}$ through the symmetric gradient ∇_{s} which is defined in the bottom right equation of Eqs. (2.3).

Although slightly more mathematically complex than Maxwell's equations (Eqs. (2.1)), Eqs. (2.3) can still grant valuable insights when considered in a simplified material system. For an isotropic material, the fourth-order stiffness tensor is simplified and reduces to $c_{ijkl} = \lambda \delta_{ij}\delta_{kl} + \mu(\delta_{ik}\delta_{jl} + \delta_{il}\delta_{jk})$, where δ_{ij} is the Kronecker delta and λ and μ are stiffness coefficients. Using this relation together with the constitutive relation

[1] $(\overline{\overline{a}} : \overline{b})_{ij} := a_{ijkl} b_{kl}$ in Einstein's compact notation.

[2] This constitutive relation is a generalization of Hooke's law.

and the definition of strain, Newton's second law for $\vec{F} = 0$ takes the following form

$$(\mu + \lambda)\nabla(\nabla \cdot \vec{u}) + \mu\nabla^2\vec{u} = \varrho\frac{\partial^2\vec{u}}{\partial t^2}. \tag{2.4}$$

Eq. (2.4) shares many features with the wave equation for electromagnetic waves (Eq. (2.2)). Indeed, this is also a wave equation with the added feature that it not only describes transverse waves with phase velocity $c_\mathrm{t} = \sqrt{\mu/\varrho}$, but also supports longitudinal waves with phase velocity $c_\mathrm{l} = \sqrt{(\lambda + 2\mu)/\varrho}$.

The wave nature of the acoustic field is retained for realistic materials with more complexity, allowing acoustic vibrations to propagate throughout solid materials much like the electromagnetic field travels through space. This forms a symmetry between our fields of interest which is a defining feature of optomechanics. The result is that parallels and analogues can be found between the fields that can help in describing observations. One such parallel is total internal reflection which is most commonly thought of as a concept within the study of optics. We will later see that this phenomenon also applies to acoustics and that it is crucial for the release-free optomechanical crystals (Sec. 3.1.1).

2.1.3 Optical forces

Having introduced the physical fields, it is now time to study how they interact. But before we move on, we comment briefly on terminology.

Studying the literature for descriptions on the optomechanical interaction is made confusing due to the many different forms of terminology one can encounter [59]. One of the main sources of confusion is that two distinct viewpoints – with associated terminology – are offered on how to understand the interactions' origins. In the first viewpoint, the interaction stems from *optical forces* imparted upon physical objects; while the other describes the interaction through the electromagnetic energy which is *perturbed* by acoustic deformation in dielectric materials. However, for lossless optical forces, these viewpoints are simply two sides of the same coin and can be fully consolidated. Optical forces acting on a physical object results in mechanical work, and thus move energy between the electromagnetic and acoustic fields. Therefore, due to the conservation of energy, one can derive the optical forces as gradient of the electromagnetic energy with respect to physical motion.

While describing the same underlying concept, it is up to personal preference on which perspective one takes. Therefore, we will for now

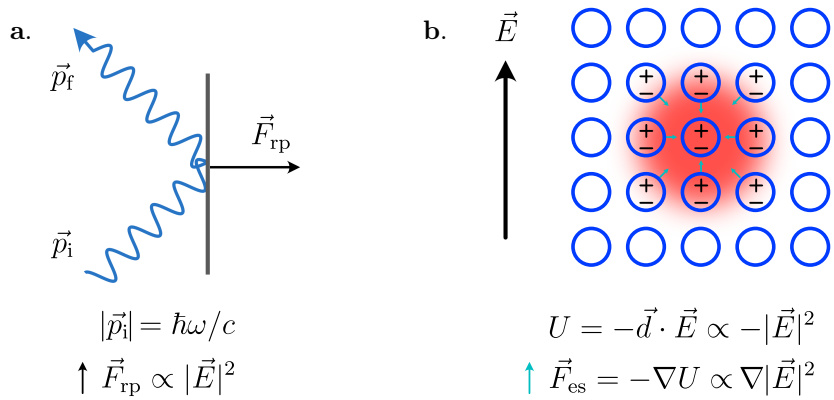


Figure 2.2: Optical forces. **a.** Radiation pressure is exerted by optical photons reflecting off physical objects through the change in their momentum $\Delta\vec{p} = \vec{p}_\mathrm{f} - \vec{p}_\mathrm{i}$. The force $\vec{F}_\mathrm{rp}$ experienced by the object is proportional to the photon flux determined by the electric field intensity for a traveling wave. **b.** A lattice of atoms that act like dipoles in an electric field with dipole moment $\vec{d}$ and potential energy U. The electrostriction force $\vec{F}_\mathrm{es}$ is proportional to electric field intensity gradients.

proceed with the force perspective as it suits well for building basic intuition for the interactions' origins. In the following, we will mainly discuss the two dominant optical forces in silicon optomechanics: Radiation pressure and photoelasticity. For a complete treatment including the roto-optic effect, and moving polarization, see Ref. [5].

Radiation pressure originates from the momentum carried by the waves of the electromagnetic field. The effect can easily be imagined through the wave-particle duality of quantum mechanics which allows us to see light-waves as particles with wave-momentum $p = \hbar\omega/c$. Here $\hbar$ is Planck's reduced constant and ω is the light angular frequency. For the electromagnetic field, the quantized particles are called photons which impart impulses to solid objects as they reflect (Fig. 2.2a). Although each photon impulse is weak, the collective effect of many photons can be strong, especially in nanoscale structures. Even macroscopic objects can be significantly impacted by strong light sources which is the working principle of solar sail propulsion [60].

The second relevant interaction is rooted in the dielectric properties of solid materials. When a dielectric particle-like object is placed in an electric field, the electric charges of the material are redistributed to balance the electromagnetic forces. This electrically polarizes the particle,

making it act as an electric dipole with its dipole moment proportional to the electric field. A dipole in an electric field is naturally pulled towards regions of space with stronger electric field where it minimizes its potential energy (Fig. 2.2b). This is the working principle of optical tweezers which traps dielectric objects in an electric field with strong intensity gradients [61]. Now, in a solid material the atoms themselves act as dipoles in strong electric fields. An electric field gradient will therefore cause atoms to redistribute in their lattice causing mechanical stress in the material. This stress is commonly termed *electrostriction* and is the second dominant interaction in silicon optomechanics.

With a basic understanding for the relevant interactions as optical forces, it is now time to formalize them mathematically. However, describing the interactions in terms of perturbations to the electromagnetic energy is more convenient to the Hamiltonian description that we will adopt in coming sections. We will thus change the viewpoint for the rest of the thesis in which the radiation pressure is the gradient of the moving boundary (MB) interaction while electrostriction is the consequence of photoelasticity (PE).

2.2 Brillouin scattering

To properly continue the discussion from here, we must make an important distinction about the types of waves we study. Due to both technical and historic reasons, the study of interacting optical and acoustic waves have different names and terminology depending on them being either traveling or stationary. The traveling wave picture is described by *Brillouin scattering* while stationary/resonant fields are more commonly associated with *cavity optomechanics*. Although both pictures describe the same physics, they come with different ways of thinking about the optomechanical system. Since both pictures have clear relevance for this work, we will continue with introducing both pictures, starting with Brillouin scattering.

The notion that light scatters on thermal sound waves in transparent media was originally proposed by Léon Brillouin in 1922 [62]. Although the phenomenon was attributed to Brillouin through its naming, the Soviet physicist Leonid Mandelstam also played a central role in the theory's development [63]. Regardless of the original conceptualist, the theory has since its formulation excelled in describing the interaction between light and sound in several different media, especially when the

fields are confined to propagate close together in a common waveguide. This has been particularly important after the invention of the laser, the optical fiber, and, in later years, the field of integrated nanophotonics in which optomechanical interactions can be exceptionally strong.

The full description detailing the time evolution of overlapping acoustic and optical waves is most commonly formulated in terms of a set of coupled mode equations (CME). The derivation of the CMEs has been given in several previous works and will not be repeated in full here [5, 59], but a brief overview sets the stage and introduces several important concepts for the following discussion.

2.2.1 Interaction-free Hamiltonians

Although only a subset of Brillouin scattering experiments is performed to observe quantum effects, the derivation of the CMEs is commonly treated quantum mechanically. This allows the theory to describe quantum effects such as vacuum fluctuations while still making it available for classical interpretation at will. The quantum description arrives at the dynamics through Heisenberg's equation of motion

$$\frac{\partial \hat{O}}{\partial t} = \frac{i}{\hbar}[\hat{H}_{\mathrm{tot}}, \hat{O}]. \tag{2.5}$$

Here, $\hat{O}$ is a field operator (either acoustic or electromagnetic) and the total system Hamiltonian

$$\hat{H}_{\mathrm{tot}} = \hat{H}_{\mathrm{EM}} + \hat{H}_{\mathrm{M}} + \hat{H}_{\mathrm{OM}} \tag{2.6}$$

is compiled of optical (EM), acoustic (M) and optomechanical (OM) contributions. The goal is thus to formulate the Hamiltonians in terms of field operators of the ingoing physical fields and apply Eq. (2.5).

We begin by restricting the analysis to a waveguide system with translational symmetry along the z-direction (Fig. 2.3). In such symmetry, we can express the ingoing fields as

$$\begin{aligned} \vec{E}(\vec{r}, t) &= \sum_n \int \mathrm{d}k \hat{a}_{nk}(t) \exp(ikz) \vec{E}_{nk}(x, y) + \mathrm{h.c.}, \\ \vec{u}(\vec{r}, t) &= \sum_m \int \mathrm{d}q \hat{b}_{mq}(t) \exp(iqz) \vec{u}_{mq}(x, y) + \mathrm{h.c.}, \end{aligned} \tag{2.7}$$

where h.c. stands for hermitian conjugate. Here we assume that the electromagnetic (acoustic) fields can be decomposed in a set of orthogonal

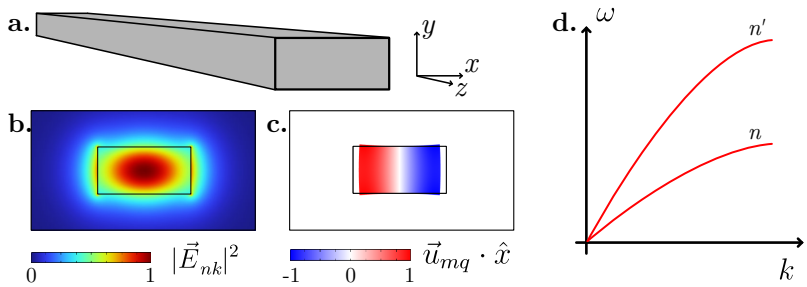


Figure 2.3: Optomechanical waveguide mode decomposition. **a.** Simple example of a rectangular waveguide guiding optical and acoustic fields along the z-axis. **b**, **c**. Examples of normalized transverse mode profiles for optical ($\vec{E}_{nk}$) and acoustic fields ($\vec{u}_{mq}$). The acoustic field is displayed with displacement. **d**. Optical band diagram displaying the waveguide-supported modes of the electric field in Eq. (2.7). Acoustic spectrum follows analogously.

eigenmodes with field annihilation operators $\hat{a}_{nk}$ ($\hat{b}_{mq}$) at wavevector k (q), where n (m) denotes the mode index. Each mode has a transverse mode profile given by $\vec{E}_{nk}$ ($\vec{u}_{mq}$) with appropriate normalization to give the field operators unit $\sqrt{\mathrm{m}}$. Being quantum mechanical field operators, $\hat{a}_{nk}$ and $\hat{b}_{mq}$ follow equal-time commutation relations

$$\begin{aligned}[\hat{a}_{nk}(t), \hat{a}^\dagger_{n'k'}(t)] &= \delta_{nn'}\delta(k-k'),\\ [\hat{b}_{mq}(t), \hat{b}^\dagger_{m'q'}(t)] &= \delta_{mm'}\delta(q-q'),\end{aligned} \tag{2.8}$$

with $\delta(x)$ being the delta distribution. The decomposition Eq. (2.7) immediately gives familiar expressions for the interaction-free Hamiltonians

$$\begin{aligned}\hat{H}_{\mathrm{EM}}(t) &= \sum_n \int \mathrm{d}k \hbar\omega_{nk}\hat{a}_{nk}(t)^\dagger \hat{a}_{nk}(t),\\ \hat{H}_{\mathrm{M}}(t) &= \sum_m \int \mathrm{d}q \hbar\Omega_{mq}\hat{b}_{mq}(t)^\dagger \hat{b}_{mq}(t),\end{aligned} \tag{2.9}$$

where ω_{nk} and Ω_{mq} denote frequencies of the optical and acoustic modes, including any potential dispersion. We also have that $\hat{a}_{nk}(t)^\dagger\hat{a}_{nk}(t)\mathrm{d}q$ ($\hat{b}_{mq}(t)^\dagger\hat{b}_{mq}(t)\mathrm{d}k$) describes the number operator for the photonic (phononic) mode with mode profile $\vec{E}_{nk}$ ($\vec{u}_{mq}$) at time t. Note that we in Eq. (2.9) leave out vacuum fluctuations since they do not add to the following dynamics.

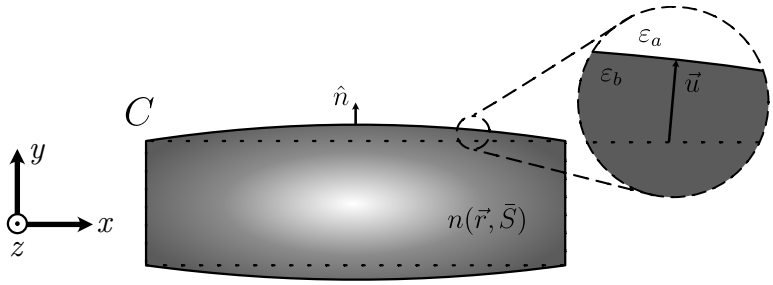


Figure 2.4: Simplified view of a cross section in the integration domain of Eqs. (2.10). An acoustic wave with displacement field $\vec{u}$ gives rise to a strain distribution $\overline{S}$. Through photoelasticity the strain locally changes the refractive index n of the bulk material while the material spatial extent is perturbed by the displacement field $\vec{u}$. Difference in material permittivity along the edge gives rise to a moving boundary contribution.

2.2.2 Interaction Hamiltonians

Having introduced the interaction-free Hamiltonians, we now turn to the interaction term $\hat{H}_{\mathrm{om}}$. As touched upon in Sec. 2.1.3, this term can be thought of as a complement to the optical Hamiltonian where acoustic waves are thought of as perturbations to the material properties of the light-bearing medium. In this picture, the acoustic waves cause both variation in the bulk refractive index through photoelasticity and alter the physical extent of medium through moving its boundaries (Fig. 2.4). We split up the perturbation in electromagnetic energy of these two effects through $\hat{H}_{\mathrm{OM}} = \hat{H}_{\mathrm{PE}} + \hat{H}_{\mathrm{MB}}$ which expressed in the ingoing field variables have the forms [64]

$$\begin{aligned}
\hat{H}_{\mathrm{PE}}(t) &= \frac{\varepsilon_0 n^4}{2} \int \mathrm{d}^3\vec{r} E_i(\vec{r},t) E_j(\vec{r},t) p_{ijkl} S_{kl}(\vec{r},t), \\
\hat{H}_{\mathrm{MB}}(t) &= \frac{1}{2} \int_C \mathrm{d}^2\vec{r} [\hat{n} \cdot \vec{u}(\vec{r},t)] \\
&\quad \times \left[(\varepsilon_a - \varepsilon_b) |\hat{n} \times \vec{E}(\vec{r},t)|^2 - (\varepsilon_a^{-1} - \varepsilon_b^{-1}) |\hat{n} \cdot \vec{D}(\vec{r},t)|^2 \right].
\end{aligned} \tag{2.10}$$

The photoelastic term is governed by the photoelastic tensor p_{ijkl} which determines a material's refractive index shift under applied strain S_{ij} and is integrated in the bulk. The moving boundary effect however, is evaluated at the two-dimensional boundary C between materials where $\hat{n}$ is the normal unit vector pointing from material b to material a with permittivities ε_a and ε_b, respectively.

2.2.3 Full dynamics

Armed with the Hamiltonians (2.9) and (2.10), we can now apply (2.5) to find the full Brillouin scattering dynamics. However, we will here spare the reader from most technical details as they serve little to provide further context to the results in this thesis and can furthermore be found in firmer rigor elsewhere [5]. The most important formalities and assumptions can however be found in App. A.

The process of obtaining the CMEs from (2.5) starts by noting the nonlinearity of the interaction Hamiltonians (2.10). The nonlinearity results in a three-wave-mixing interaction between any two optical modes and one acoustic mode. Even though all optical and mechanical modes can be considered for coupling, conservation laws and input conditions allows for a truncation in the modal spectrum. The CMEs are thus commonly formulated for one pair of optical modes interacting with one acoustic mode. In the terminology of Brillouin scattering, the two optical modes are labeled pump (p) and Stokes (s) fields, mirroring that of Raman scattering. The reduced form of the Brillouin CMEs thus follows as

$$v_{\mathrm{p}}^{-1}\partial_t\hat{a}_{\mathrm{p}} + \partial_z\hat{a}_{\mathrm{p}} = -ik_{\mathrm{p}}\hat{a}_{\mathrm{p}} - i\tilde{g}_0\hat{a}_{\mathrm{s}}\hat{b}_{\mathrm{m}}, \tag{2.11}$$

$$v_{\mathrm{s}}^{-1}\partial_t\hat{a}_{\mathrm{s}} \pm \partial_z\hat{a}_{\mathrm{s}} = -ik_{\mathrm{s}}\hat{a}_{\mathrm{s}} - i\tilde{g}_0\hat{a}_{\mathrm{p}}\hat{b}_{\mathrm{m}}^{\dagger}, \tag{2.12}$$

$$v_{\mathrm{m}}^{-1}\partial_t\hat{b}_{\mathrm{m}} \pm \partial_z\hat{b}_{\mathrm{m}} = -iq_{\mathrm{m}}\hat{b}_{\mathrm{m}} - i\tilde{g}_0\hat{a}_{\mathrm{p}}\hat{a}_{\mathrm{s}}^{\dagger}. \tag{2.13}$$

We first note that the mode operators for pump ($\hat{a}_{\mathrm{p}}$), Stokes ($\hat{a}_{\mathrm{s}}$) and acoustic ($\hat{b}_{\mathrm{m}}$) fields now represent flux-normalized amplitude envelope operators and have units $\mathrm{s}^{-1/2}$. These are annihilation operators for photons and phonons at time t and *position* z along the waveguide in each respective mode (App. A). For each mode, we have also introduced group velocities $v_{\mathrm{p/s/m}}$ and wavenumbers $k_{\mathrm{p/s}}, q_{\mathrm{m}}$. For the wavenumbers, a phase-matching condition $k_{\mathrm{p}} = k_{\mathrm{s}} + q_{\mathrm{m}}$ is assumed which will play a major role in the description of release-free optomechanical crystals in Chapter 3. The propagation direction of pump and Stokes fields can either be co- or counter-propagating which is represented by the $\pm$ sign in (2.12) and (2.13). The coupling rate $\tilde{g}_0$ describes the strength of the three-wave mixing interaction and is obtained through overlap integrals of the transverse fields. The coupling is also commonly described in terms of the Brillouin gain $\mathcal{G}$ which is the primary metric used in Sec. 3.1.2 and Sec. 3.1.3 (see App. A for more details).

Eqs.(2.11)-(2.13) describe an interaction with many different con-

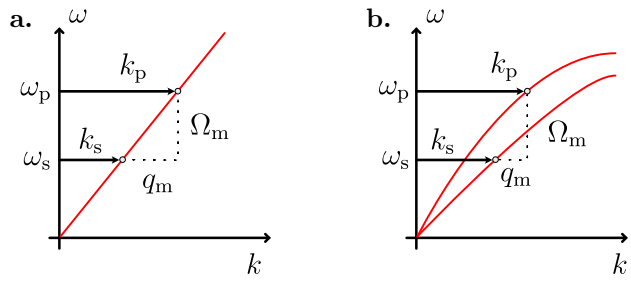


Figure 2.5: Optical band diagrams depicting Brillouin scattering with co-propagating pump and Stokes waves. **a.** Intramodal scattering where both interacting optical modes occupy the same spatial mode (red line) **b**. Intermodal scattering provides coupling between two disparate spatial modes. For both processes, momentum and energy conservation require $k_\mathrm{p} - k_\mathrm{s} = q_\mathrm{m}$ and $\omega_p - \omega_s = \Omega_m$.

figurations. Apart from pump and Stokes fields being either co- or counter-propagating, they can also inhabit the same or different spatial modes. While momentum and energy conservations are respected, mixing between optical modes in both differing and the same spatial mode is permitted, given that no spatial symmetries are broken in the process (Fig. 2.5). Despite the many different versions, all types of Brillouin scattering achieve the same fundamental phenomenon: establishing a channel for coherent energy transfer between the optical and acoustic domains. This property is what mediates transfer of information across five orders of magnitude in frequency, a feature that is highly sought after in both classical and quantum technologies.

2.3 Cavity optomechanics

In the last section, we studied the interplay between optical and acoustic waves traveling together in translationally invariant waveguides. Even though the optomechanical crystals of this thesis can be fully understood in this waveguide picture, they have additional properties that allows for a slightly more elegant description. The relevant property is the spectral distribution – or the bandwidth – of the device. A simple waveguide is a broadband device that can be operated in an as large part of the band diagram that material properties allow (Fig. 2.3). An optomechanical crystal on the other hand is a resonant system, technically acting as a filter for optical and acoustic waves, permitting only a narrow band

of excitation frequencies and wavelengths. The sacrifice in bandwidth is repaid in amplified interaction strength and robustness to fabrication imperfections, both of which are well received properties for many relevant applications.

For resonant optomechanical systems, the theory of *cavity optomechanics* is well-developed and applies to a plethora of different physical implementations ranging from optical microtoroids [65, 13, 16], silica microspheres [66], Fabry–Pérot (FP) cavities with moving mirrors [11, 52, 67], microwave resonators with moving capacitor plates [15], and more. The theory has been well-established since late 2000's and has predicted a plethora of effects on both classical and quantum levels. As in the previous section, the derivations leading to applicable results are already well-covered in previous work [17] and will only be covered here to the extent that it introduces useful concepts for further discussion.

2.3.1 Cavity optomechanical Hamiltonians

We start the discussion by considering two quantum harmonic oscillators, one embodying the optical degree of freedom and the other one the mechanics. We assume that these two oscillators have unperturbed resonance frequencies ω_o and ω_m for optics and mechanics, respectively, where $\omega_\mathrm{o}/2\pi \sim 194\,\mathrm{THz}$ and $\omega_\mathrm{m}/2\pi \sim 5\,\mathrm{GHz}$ for the majority of this thesis. Being a quantum description, we assign annihilation operators to the two oscillators that follow standard commutation relations

$$\begin{aligned}[\hat{a}, \hat{a}^\dagger] &= 1, \\ [\hat{b}, \hat{b}^\dagger] &= 1,\end{aligned} \tag{2.14}$$

where we here follow the notation of the last sections and take $\hat{a}$ for optics and $\hat{b}$ for mechanics. To model the coupling between these modes, we proceed as in the previous section and view the mechanics as a perturbation of the energy in the optical mode. Adopting the working principles of a standard FP-cavity with a movable mirror (Fig. 2.6), we linearize the optical frequency dependence on displacement x according to

$$\omega_\mathrm{o} \to \omega_\mathrm{o} + \hat{x}\left.\frac{\partial \omega_\mathrm{o}}{\partial x}\right|_{x=0} = \omega_\mathrm{o} + g_\mathrm{om}(\hat{b} + \hat{b}^\dagger), \tag{2.15}$$

where $\hat{x} = x_\mathrm{zpf}(\hat{b} + \hat{b}^\dagger)$ is the mechanical oscillator's position operator with zero-point fluctuations x_zpf. The coupling strength is determined through the zero-point optomechanical coupling rate $g_\mathrm{om} =$

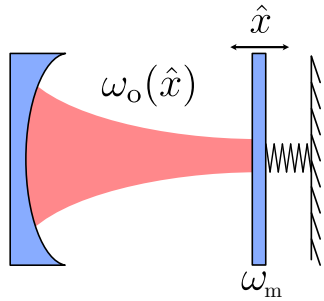


Figure 2.6: Basic optomechanical FP-cavity. The right mirror oscillates at ω_m with position $\hat{x} = 0$, affecting the optical resonance frequency $\omega_\mathrm{o}(\hat{x})$.

$x_\mathrm{zpf}\partial_x\omega_\mathrm{o}|_{x=0}$. Using Eq. (2.15) the standard Hamiltonian for harmonic oscillators immediately turns into

$$\hat{H}_\mathrm{tot}/\hbar = \omega_\mathrm{o}\hat{a}^\dagger\hat{a} + \omega_\mathrm{m}\hat{b}^\dagger\hat{b} + g_\mathrm{om}\hat{a}^\dagger\hat{a}(\hat{b} + \hat{b}^\dagger), \tag{2.16}$$

which contains much of the relevant physics[3]. However, the interaction Hamiltonian is most commonly linearized in the optical field by assuming a strong coherent optical pump such that $\hat{a} = \overline{a} + \delta\hat{a}$ where $\overline{a}$ is the strong pump amplitude. We assume $\overline{a} \in \mathbb{R}$ w.l.o.g. such that $\overline{a} = \sqrt{n_\mathrm{c}}$ where $n_\mathrm{c} = \langle\hat{a}^\dagger\hat{a}\rangle$ is the average optical photon population in the optical cavity. While the terms quadratic in $\overline{a}$ leads to a static shift in $\hat{x}$, they do not contribute to the dynamics. We thus only keep terms linear in $\overline{a}$ and arrive at the linearized interaction Hamiltonian[4]

$$\hat{H}_\mathrm{int,lin} = \hbar g_\mathrm{om}\sqrt{n_\mathrm{c}}(\hat{a} + \hat{a}^\dagger)(\hat{b} + \hat{b}^\dagger). \tag{2.17}$$

The strong optical pump is assumed to have an angular frequency ω_l with a detuning with respect to the optical mode $\Delta = \omega_\mathrm{l} - \omega_\mathrm{o}$. By moving to frame rotating at ω_l, the operator products in Eq. (2.17) rotates either fast or slow depending on the value of Δ. When $\Delta = \omega_\mathrm{m}$, we have that $\hat{a}^\dagger\hat{b}^\dagger, \hat{a}\hat{b}$ are stationary while $\hat{a}^\dagger\hat{b}, \hat{a}\hat{b}^\dagger$ rotate at $\pm 2\omega_\mathrm{m}$. For this detuning, the latter terms are thus removed in a rotating wave approximation (RWA) while the former are removed when $\Delta = -\omega_\mathrm{m}$ (see also App. B.2).

[3]Note that the sign of the interaction Hamiltonian is dependent on the coordinate system chosen for $\hat{x}$ and is thus arbitrary.

[4]Note that we in (2.17) get rid of the δ in the linearized cavity operator notation for later brevity.

2.3.2 Coupling to thermal baths

To complete the theoretical picture we have to introduce additional couplings for both optical and mechanical degrees of freedom which allows the system to interact with its surroundings. This is what introduces the system to loss, noise and external drive and is commonly modeled through input-output theory which we summarize briefly below. A more detailed description can be found in other works, see e.g. Ref. [68].

In input-output theory, the environment is modeled as one or several ensembles of harmonic oscillator modes that couple to one of the system's degrees of freedom. We take the optical mode as an example for which the dynamics are derived through the ensemble's (or bath's) annihilation operators $\{\hat{c}_n\}_{n=1}^{\infty}$ that are assumed to couple to the optical mode through

$$\hat{H}_{\text{int}} = -i\hbar \sum_n f_n \hat{a}^\dagger \hat{c}_n - f_n^* \hat{c}_n^\dagger \hat{a}, \tag{2.18}$$

with f_n being complex coupling coefficients. To properly analyze how this affects the dynamics of the optical cavity the Markovian approximation is taken which sets the coupling rates equal ($\sqrt{|f_n|^2} = f$) and assumes a constant frequency domain density of states (ρ_c) for the bath over the relevant range of frequencies. With these simplifications we can define input and output operators for the bath

$$\hat{a}_{\text{in}}(t) = \frac{1}{\sqrt{\rho_c}} \sum_n \hat{c}_n(t_0) e^{-i\omega_n(t-t_0)}, \quad \hat{a}_{\text{out}}(t) = \frac{1}{\sqrt{\rho_c}} \sum_n \hat{c}_n(t_1) e^{-i\omega_n(t-t_1)}, \tag{2.19}$$

where ω_n are the bath modes' oscillation frequencies and t_0 (t_1) are distant times before (after) relevant interactions. If the remaining system Hamiltonian (i.e. Eq. (2.17)) is independent of the bath modes, the input- and output-fields are related through

$$\hat{a}_{\text{out}}(t) = \hat{a}_{\text{in}}(t) - \sqrt{\kappa_c}\hat{a}(t), \tag{2.20}$$

where $\kappa_c = f^2\rho_c$. Eq. (2.20) is commonly referred to as the input-output relation and is a useful result for both predicting measured system responses and to hide complicated environment dynamics behind input fields with predefined properties.

2.3.3 Cavity optomechanical dynamics

Now we combine the linearized optomechanical Hamiltonian with the results of input-output theory to get the CMEs of cavity optomechanics

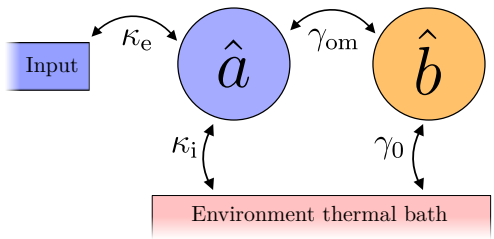


Figure 2.7: Basic optomechanical mode diagram. Optical and mechanical modes are denoted $\hat{a}$ and $\hat{b}$, respectively. The mechanical mode couples to the optics through the optomechanical scattering rate $\gamma_{om} = 4g_{om}^2/\kappa$ (Sec. 2.4.1) and to the thermal environment γ_0. Apart from its coupling to $\hat{b}$, $\hat{a}$ couples to the thermal environment with κ_i and to an input waveguide with κ_e.

as a set of quantum Langevin equations

$$\begin{aligned}\dot{\hat{a}} &= \left(i\Delta - \frac{\kappa}{2}\right)\hat{a} - i\sqrt{n_c}g_{om}(\hat{b}+\hat{b}^\dagger) + \sqrt{\kappa_e}\hat{a}_{in,e} + \sqrt{\kappa_i}\hat{a}_{in,i},\\ \dot{\hat{b}} &= -\left(i\omega_m + \frac{\gamma_0}{2}\right)\hat{b} - i\sqrt{n_c}g_{om}(\hat{a}+\hat{a}^\dagger) + \sqrt{\gamma_0}\hat{b}_{in,0}.\end{aligned} \tag{2.21}$$

Here, we moved into the rotating frame for the optical degree of freedom which rotates with the excitation laser frequency ω_l. This introduces the detuning parameter $\Delta = \omega_l - \omega_o$ into the equations which determines the dominant interaction. When taking the RWA in these equations, we remove $\hat{a}, \hat{b}$ from the interaction terms when $\Delta = \omega_m$ and $\hat{a}^\dagger, \hat{b}^\dagger$ when $\Delta = -\omega_m$.

We have also introduced two decay channels for the optics and one for the mechanics which we summarize below (Fig. 2.7):

- External (e) optical coupling allows for exciting and reading out the state of the optical cavity with rate κ_e,
- Internal (i) optical decay mainly accounts for inaccessible photon loss to the environment at rate κ_i,
- Internal decay through phonon loss with rate γ_0. Due to the relatively low mechanical frequency, this coupling is also a significant channel for input thermal noise.

Taken together, the two optical couplings give the total optical decay rate $\kappa = \kappa_e + \kappa_i$.

The temperatures of the environmental baths are defined via the autocorrelation functions for the input fields. Within the Markov approximation the autocorrelation functions are defined as

$$\begin{aligned}\langle \hat{a}_{\mathrm{in,e/i}}(t)\hat{a}^{\dagger}_{\mathrm{in,e/i}}(t')\rangle &= \delta(t-t'),\\ \langle \hat{a}^{\dagger}_{\mathrm{in,e/i}}(t)\hat{a}_{\mathrm{in,e/i}}(t')\rangle &= 0,\\ \langle \hat{b}_{\mathrm{in},0}(t)\hat{b}^{\dagger}_{\mathrm{in},0}(t')\rangle &= (n_0+1)\delta(t-t'),\\ \langle \hat{b}^{\dagger}_{\mathrm{in},0}(t)\hat{b}_{\mathrm{in},0}(t')\rangle &= n_0\delta(t-t'),\end{aligned} \tag{2.22}$$

where $\langle\cdot\rangle$ is the quantum mechanical expectation value and n_0 is the average bath population of thermal phonons at given temperature and oscillation frequency governed by Bose–Einstein statistics. The average bath photon number is assumed to be 0 throughout this thesis due to the high optical frequencies[5].

2.3.4 Symmetries between optomechanical pictures

When arriving at Eq. (2.21), we have presented CMEs for both stationary optomechanical cavities and for traveling optical and acoustic waves (Eq. (2.11)-(2.13)). At first glance these two pictures seems somewhat detached, although both theories treat optical waves and vibrations of some kind. However, these two pictures are intimately connected and one set of CMEs can be derived from the other given correct assumptions. It is not in the interest of this thesis to go into any significant depth no this discussion, but we will mention that the connection stems from mean-field envelope operators

$$\hat{\bar{a}}(t) = \frac{1}{L}\int_0^L \hat{a}(z,t)\mathrm{d}z. \tag{2.23}$$

In this description, boundary conditions $\hat{a}(0,t) = \hat{a}(nL,t)$ applies where $n \in \mathbb{Z}$ and L is the cavity round-trip length. This leads to the result

$$v_{\mathrm{p}}v_{\mathrm{s}}\frac{(\hbar\omega_{\mathrm{p}})\omega_{\mathrm{m}}}{4L}\left(\frac{\mathcal{G}}{Q_{\mathrm{m}}}\right) = g_{\mathrm{om}}^2, \tag{2.24}$$

which connects the optomechanical coupling g_{om} to the Brillouin gain coefficient $\mathcal{G}$ (for more details, see App. B.3). Newly introduced quantities are the pump frequency ω_{p} and the mechanical quality factor Q_{m}. The interested reader finds the full details in Ref. [69].

[5] Average 5 GHz phonon occupation at room temperature $\approx 1.2 \cdot 10^3$. Average 194 THz optical photon at room temperature $\approx 3.3 \cdot 10^{-14}$.

Before moving on to discuss the measurable consequences of the optomechanical coupling, we comment briefly on the relevance of the two different pictures of optomechanics to different parts of this thesis. Brillouin scattering is of primary interest when describing the design of the release-free optomechanical crystal cavity (OMC). Being waveguide systems, the concepts of pump and Stokes fields, moving-boundary and photoelastic interactions, and co-/counter-propagating waves are crucial for design and optimization of device properties.

When the OMC is designed and fabricated, however, it acts as a canonical cavity optomechanical system and does not require the concepts of Brillouin scattering to be understood in the lab. It is here that the cavity optomechanical picture is paramount to building intuition for the physical phenomena that experiments unveil.

2.4 Optomechanical consequences

With an established coupling between the optical and mechanical systems, we can now turn our attention to what effect this coupling has on the ingoing systems. These consequences of the optomechanical coupling mainly serve as tools to manipulate the properties or quantum states of the ingoing systems, but they also serve practical uses such as providing experimental gauges for the properties of the combined system. In this section we will introduce some effects that has been important for the work in this thesis. We base this discussion on the theory of cavity optomechanics which was introduced in Sec. 2.3.

2.4.1 Thermomechanical scattering

To properly begin this discussion, it is helpful to introduce the three-wave mixing formalism from Brillouin scattering (Sec. 2.2.3) into cavity optomechanics. Unlike the Brillouin scattering CMEs (Eq. (2.11)-(2.13)), the CMEs of cavity optomechanics (Eq. (2.21)) do not make it obvious that they describe the interaction between one mechanical and several optical frequencies. A way to visualize this is through Doppler shifting. Photons occupying the optical cavity can scatter off the movable mirror of the mechanical mode and are either shifted up or down in frequency depending on the mirror's current velocity (see Fig. 2.6).

We can make this more formal by thinking about the photons interacting directly with the phonons in the mechanical mode (Fig. 2.8). Two scenarios are of relevance here,

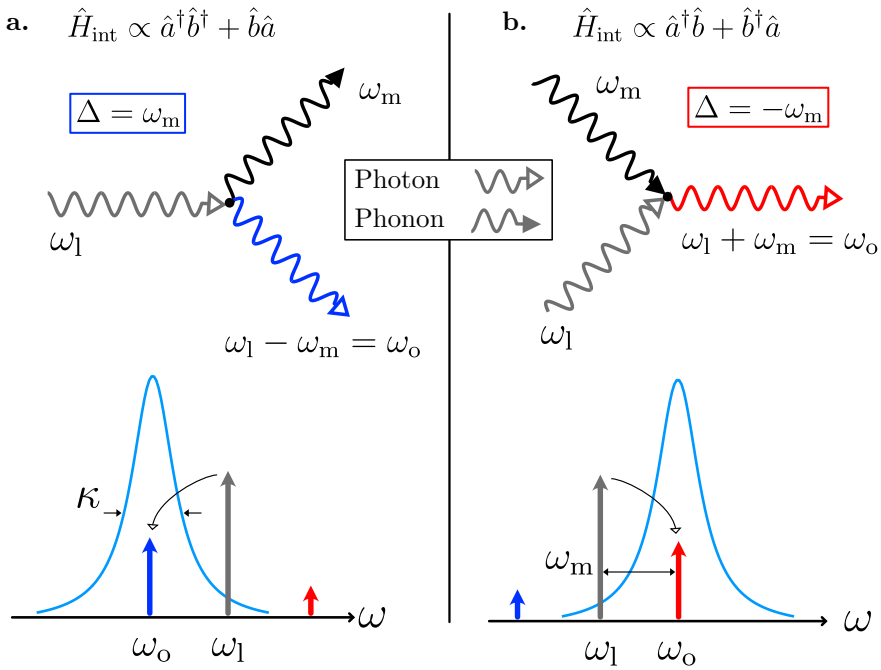


Figure 2.8: Three-wave mixing processes of optomechanics. The lower panels show optical spectra where the optical cavity density of states is used to single out the desired scattering process. **a.** Stokes scattering for which the two-mode squeezing Hamiltonian is dominant. This process dominates for blue detuning ($\Delta = \omega_{\rm m}$) and causes pump photons ($\omega_{\rm l}$) to generate entangled photon-phonon pairs. **b.** Anti-Stokes scattering which gives rise to a beam-splitter Hamiltonian. When red detuned ($\Delta = -\omega_{\rm m}$), pump photons are consumed along with mechanical phonons to generate upconverted anti-Stokes photons.

1. The input optical photon at frequency ω_l splits into an entangled particle-pair with a phonon at frequency ω_m and a (Stokes) photon at $\omega_\mathrm{l} - \omega_\mathrm{m}$,

2. The input photon combines with a phonon into an upconverted (anti-Stokes) photon at the sum frequency. This process transfers quantum information from the phonon to the upconverted photon.

The photons at the sum and difference frequencies can be thought of as optomechanical sidebands that carry information about the optomechanical interaction. With an optical cavity with narrow full-width-half-maximum (FWHM) κ such that $\kappa \ll \omega_\mathrm{m}$, we can actively choose which of the two scattering processes that dominates by placing the pump laser such that the desired sideband is resonant with the cavity (Fig. 2.8). This is equivalent to taking the RWA by choosing detuning $\Delta = \pm\omega_\mathrm{m}$ as discussed in Sec. 2.3.1.

Both types of scattering processes are stimulated on mechanical phonon occupancy, meaning that the more mechanical phonons present, the more sideband scattering events occur [70]. When $\Delta = \pm\omega_\mathrm{m}$ in the sideband resolved regime[6], the cavity optomechanical CMEs gives the base rate for this scattering event

$$\gamma_\mathrm{om} = \frac{4n_\mathrm{c}g_\mathrm{om}^2}{\kappa}, \tag{2.25}$$

which we call the *optomechanical scattering rate*. The total sideband photon flux inside the optical cavity can thus be estimated by $\gamma_\mathrm{om}n_\mathrm{m}$, where n_m is the average phonon occupation which is assumed to be $\gg 1$ at room temperature[7]. If $\gamma_\mathrm{om} \ll \gamma_0$, this allows for an estimation on the expected power P_om in the optical sideband created when pump light reflects off the optomechanical cavity

$$\begin{aligned} P_\mathrm{om} &\approx \hbar\omega_\mathrm{l}\gamma_\mathrm{om}n_\mathrm{m}\eta_\mathrm{o} \\ &\approx \hbar\omega_\mathrm{l}\Phi_\mathrm{in}n_\mathrm{m}\left(\frac{2\eta_\mathrm{o}g_\mathrm{om}}{\omega_\mathrm{m}}\right)^2 \\ &= P_\mathrm{in}n_\mathrm{m}\left(\frac{2\eta_\mathrm{o}g_\mathrm{om}}{\omega_\mathrm{m}}\right)^2. \end{aligned} \tag{2.26}$$

Here we used that $\omega_\mathrm{m} \ll \omega_\mathrm{l}$ and introduced the optical coupling efficiency $\eta_\mathrm{o} = \kappa_\mathrm{e}/\kappa$ expressing the probability that a sideband photon

[6] i.e. the limit when $\kappa \ll \omega_\mathrm{m}$.

[7] at cryogenic temperatures when $n_\mathrm{m} \sim 1$, the scattering is asymmetric for $\Delta = \pm\omega_\mathrm{m}$. This is covered in Sec. 2.4.4.

in the cavity is extracted into the input waveguide for detection. Finally, we use the sideband-resolved expression for $n_c \approx \Phi_{in}\kappa_e/\omega_m^2$ with Φ_{in} being the input optical photon flux (see App. B). Taking the ratio P_{om}/P_{in} yields the relative power in the optomechanical sideband which depends on optomechanical properties and temperature. For reasonable optomechanical properties this ratio is on the order of $-50\,\mathrm{dBc}$ for room temperature experiments. This signal is easily detected through a variety of detection schemes such as direct photo-detection, homo- and heterodyne detection, and single-photon counting.

2.4.2 Optomechanical back-action

The optomechanical scattering rate introduced in the last subsection is an important parameter which not only governs the power in the optomechanical sideband but also directly influences the dissipation in the mechanical mode. The Stokes process injects phonons into the mechanical mode with a well-defined phase reference to the optical pump and therefore works against phonon leakage. Conversely, the anti-Stokes process consumes phonons leading to additional dissipation (Fig. 2.8).

The above dynamics can be elucidated by solving the cavity optomechanical CMEs (Eq. (2.21)). By assuming either $\Delta = \pm\omega_m$ and solving for the mechanical degree of freedom. The results show that the optomechanical coupling gives rise to an altered mechanical susceptibility [17]

$$\chi_m'(\omega) = \frac{1}{i(\omega_m - \omega) + (\gamma_0 \pm \gamma_{om})/2}, \quad \text{for } \omega \sim \omega_m. \tag{2.27}$$

In the above, we have omitted the optical spring-effect and the minus sign is chosen for $\Delta = \omega_m$. This predicts that the optomechanical coupling opens up an additional mechanical dissipation channel which can work in both directions depending on detuning (Fig. 2.7). Since $\gamma_{om} \propto n_c$, this effect is commonly used to gauge the optomechanical coupling of sideband-resolved systems, such as the release-free OMC in Paper A.

The implications of this effect are many. Since the optical environment can be assumed to be at zero temperature (Eq. 2.22) the additional dissipation granted for red detuning does not come with any added thermal noise[8]. This allows for an effective "cooling" of mechanical modes which is routinely used to reach lower phonon occupations than the environmental temperature allows. Examples of systems where this has

[8] It does however come with quantum fluctuation noise.

been successfully applied to reach phonon occupations at or near the quantum ground state include integrated micro-mirrors in FP-style cavities [11], SiN membranes in membrane-in-the-middle cavity configurations [67], microwave-driven capacitor membranes [15] and silicon OMCs [20, 21, 28]. The limits to the achievable cooling depends on external heating and ultimately the quantum back-action noise in the drive laser [17].

In the case of blue detuning, the optical pump drives the mechanical mode through a stream of phonons generated via the Stokes process. Each injected phonon can, in turn, seed another coherent scattering event, thereby building up the amplitude of the mechanical oscillation. This typical case of parametric amplification is governed by the *optomechanical cooperativity*

$$C_{\mathrm{om}} = \frac{\gamma_{\mathrm{om}}}{\gamma_0}. \tag{2.28}$$

This property can be viewed as the relative odds for a phonon to stimulate an optomechanical scattering event over being lost through intrinsic decay. When the cooperativity exceeds unity under blue detuning, the mechanical mode enters a regime of self-induced oscillation, producing what may be regarded as a phononic laser source. This phenomenon is demonstrated in Paper A and is relevant for radio-frequency (RF) signal processing [71, 72, 73].

The optomechanical cooperativity (2.28) has major significance even under red detuning. When the beam-splitter Hamiltonian is active (Fig. 2.8), coherent swapping between phonons and cavity photons is made possible. In this regime, C_{om} governs the fidelity of a swap operation, i.e. the degree to which a swapping operation is successful over phonon loss. This is especially important for microwave-optics transduction and will be returned to in Chapter 5.

2.4.3 Electromagnetically induced transparency

The effects discussed up to this point have involved scattering driven by thermal mechanical occupation. These signals are easily observed in room temperature when phonon occupation is high, giving easy access to optomechanical properties. However, at dilution refrigerator temperatures of $\sim 10\,\mathrm{mK}$, a well thermalized mechanical mode with $\omega_{\mathrm{m}}/(2\pi) \sim 5\,\mathrm{GHz}$ is at $n_{\mathrm{m}} \ll 1$ without external heating. In this regime, thermomechanical signatures are weak, requiring quantum-limited measurement techniques such as homo-/heterodyne detection or single-photon count-

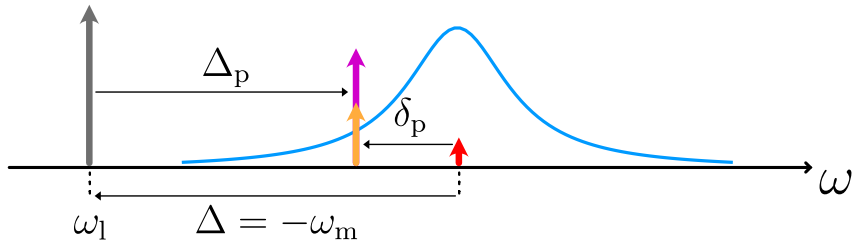


Figure 2.9: Electromagnetically induced transparency. A pump tone (gray) at ω_l is modulated with an EOM probe at Δ_p (magenta). The beating between pump and probe tones generates a coherent mechanical excitation that stimulates an optomechanical sideband at $\omega_\mathrm{l} + \Delta_\mathrm{p}$ (orange). The interference between probe and optomechanical sideband depends on the probe detuning $\delta_\mathrm{p} = \Delta_\mathrm{p} - \omega_\mathrm{m}$ from the thermomechanical sideband (red), causing optomechanical dependence to the probe reflection.

ing to properly resolve. But in cases when the thermal properties of the mechanical device is not of primary concern, the thermal stimulus can instead be substituted with coherent driving.

Electromagnetically induced transparency (EIT)[9] is an effect commonly observed in atomic and molecular systems where an optical probe tone can experience a window of transparency due to self-interference through the coupled system [75]. The optomechanical Hamiltonian also supports this effect, allowing for probing optomechanical properties without relying on thermal mechanical occupancy.

The effect is best observed while detuned to either motional sideband ($\Delta = \pm\omega_\mathrm{m}$) and the optical pump is modulated with an electro-optic modulator (EOM) at frequency $\Delta_\mathrm{p} \sim \omega_\mathrm{m}$ before being sent to the optomechanical system. Due to the optical density of states, the field inside the cavity predominantly consists of the pump tone at ω_l and the EOM-modulated sideband (or probe tone) at $\omega_\mathrm{l} + \Delta_\mathrm{p} \sim \omega_\mathrm{o}$ (Fig. 2.9). The two tones inside the cavity cause the internal light intensity to beat, driving the mechanical mode through optical forces at frequency Δ_p. The coherent mechanical excitation at Δ_p stimulates optomechanical scattering with the strong pump at ω_l, giving rise to an optomechanical sideband at $\omega_\mathrm{l} + \Delta_\mathrm{p}$ which coincides with the EOM-modulated sideband. Since coherence is preserved throughout this process, the tones interfere which can cause the optomechanical system to appear transparent for the probe tone.

[9] also sometimes known as *optomechanically* induced transparency (OMIT) [74].

To find theoretical understanding, we return to the cavity optomechanical CMEs (Eq. (2.21)). The following derivation will treat $\Delta = -\omega_\mathrm{m}$ but is similar for $\Delta = \omega_\mathrm{m}$. We are interested in the system response when driven by a strong pump at $\omega_\mathrm{l} \approx \omega_\mathrm{o} - \omega_\mathrm{m}$ modulated with an intensity modulating EOM at Δ_p. By omitting the contribution from $\hat{a}_\mathrm{in,i}, \hat{b}_\mathrm{in,0}$ we find the solution for the output optical field using input-output theory Eq. (2.20) (see App. B.2, Eq. (B.6))

$$\begin{aligned}\hat{a}_\mathrm{out,e}(\omega) &= \left[1 - \frac{\kappa_\mathrm{e}}{\chi_\mathrm{o}^{-1}(\omega) + \chi_\mathrm{m}(\omega) G_\mathrm{om}^2}\right] \hat{a}_\mathrm{in,e}(\omega) \\ &= r(\omega)\hat{a}_\mathrm{in,e}(\omega).\end{aligned} \tag{2.29}$$

Remember that the equations are formulated in a rotating frame for the optical degree of freedom. Apart from vacuum fluctuations, the input field contains the strong pump at $\omega = 0$ and modulation tones at $\pm\Delta_\mathrm{p}$, where the upper tone at Δ_p is called the probe. When reflecting off the system, these tones will pick up reflection coefficients $r(-\Delta_\mathrm{p}) \approx r(0) \approx 1$ (for $\kappa \ll \omega_\mathrm{m}$) and $r(\Delta_\mathrm{p})$, respectively. Looking closer at the probe tone reflection coefficient we get

$$\begin{aligned}r(\Delta_\mathrm{p}) &= 1 - \frac{\kappa_\mathrm{e}}{-i(\Delta_\mathrm{p} - \omega_\mathrm{m}) + \kappa/2 + G_\mathrm{om}^2/(-i(\Delta_\mathrm{p} - \omega_\mathrm{m}) + \gamma_0/2)} \\ &\approx 1 - 2\eta_\mathrm{o} \frac{-i\delta_\mathrm{p} + \gamma_0/2}{-i\delta_\mathrm{p} + (\gamma_0 + \gamma_\mathrm{om})/2},\end{aligned} \tag{2.30}$$

where we introduced $\delta_\mathrm{p} = \Delta_\mathrm{p} - \omega_\mathrm{m}$ which is assumed to be comparable to γ_0 such that $\delta_\mathrm{p} \ll \kappa/2$. We thus see probe tone's reflection coefficient is dependent on the optomechanical coupling.

The intensity modulated input field can now be expressed with the classical amplitude

$$\alpha_\mathrm{in} = \alpha_0(1 + \beta e^{-i\Delta_\mathrm{p} t} + \beta e^{i\Delta_\mathrm{p} t}), \tag{2.31}$$

where $\beta \ll 1$. After interacting with the optomechanical system, the output field has picked the reflection coefficients and is approximately given by

$$\alpha_\mathrm{out} \approx \alpha_0(1 + \beta r(\Delta_\mathrm{p}) e^{-i\Delta_\mathrm{p} t} + \beta e^{i\Delta_\mathrm{p} t}). \tag{2.32}$$

To measure this signal, we detect the beating between pump and probe on a high-speed photo-detector (HSPD) and demodulate the signal at

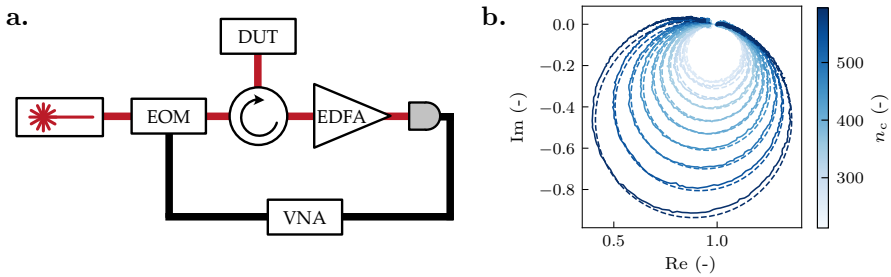


Figure 2.10: a. Setup for measuring EIT. A laser is modulated by an EOM before being sent to the device under test (DUT). To bring the signal above the electronic noise floor of the HSPD, the signal is amplified before detection with an erbium-doped fiber amplifier (EDFA). A VNA coherently detects the photo-detector output at the modulation frequency Δ_p. **b.** Typical EIT data for a blue detuned pump at varying n_c with fits to (2.35).

Δ_p with a vector network analyzer (VNA). The demodulated complex voltage signal V_det at Δ_p will thus follow

$$V_\mathrm{det}(\Delta_\mathrm{p}) \propto 1 + r(\Delta_\mathrm{p}). \tag{2.33}$$

Normalizing this to the signal at $|\delta_\mathrm{p}| \gg \gamma_0 + \gamma_\mathrm{om}$ while still satisfying $|\delta_\mathrm{p}| \ll \kappa/2$ gives the following useful result

$$\begin{aligned} V_\mathrm{det,norm}(\Delta_\mathrm{p}) &= \lim_{\omega\to\infty} \frac{V_\mathrm{det}(\Delta_\mathrm{p})}{V_\mathrm{det}(\omega)} \\ &= 1 + \frac{\eta_\mathrm{o}/2}{1-\eta_\mathrm{o}} \frac{\gamma_\mathrm{om}}{-i\delta_\mathrm{p} + (\gamma_0 \pm \gamma_\mathrm{om})/2}. \end{aligned} \tag{2.34}$$

The above equation describes a complex Lorentzian with FWHM $\gamma_0 \pm \gamma_\mathrm{om}$, where the minus sign is chosen for $\Delta = \omega_\mathrm{m}$.[10]

Eq. (2.34) allows for measurement of the optomechanical scattering rate γ_om through coherent excitation of the mechanics. A common way to perform this measurement is by using a VNA to both generate the probe tone and to measure the detected signal at Δ_p (Fig. 2.10). Lastly we note that phase delays and differing losses for pump and probe tones alters the measured signal slightly. To compensate for this, we introduce auxiliary parameters $A, \theta \in \mathbb{R}$ to define the final fitting function

$$V_\mathrm{det,fit}(\Delta_\mathrm{p}) = 1 + \frac{Ae^{i\theta}}{-i\delta_\mathrm{p} + (\gamma_0 \pm \gamma_\mathrm{om})/2}. \tag{2.35}$$

[10] for blue detuning one also redefines $\delta_\mathrm{p} = \Delta_\mathrm{p} + \omega_\mathrm{m}$.

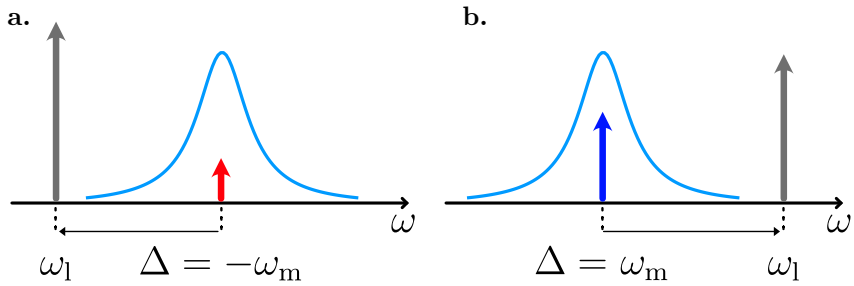


Figure 2.11: Sideband asymmetry. Due to vacuum fluctuations in the mechanical mode, the optomechanical sideband differs in power depending on the pump laser's detuning Δ. For low cooperativities, the output optomechanical sideband flux in the anti-Stokes process (**a**) is lower than in the Stokes process (**b**) with difference given by $\gamma_{\mathrm{om}}\eta_{\mathrm{o}}$.

2.4.4 Sideband asymmetry

In Sec. 2.4.1 we discussed how thermal occupation in the mechanical system leads to Stokes- and anti-Stokes scattering, leaving an imprint on light scattered off the optomechanical system. We noted that due to the stimulated nature of the processes, the power in the scattered sidebands is dependent on the phonon occupation in the mechanical system. This gives an opportunity to optically infer the phonon population by studying the reflected light. However, the power in the sidebands is also affected by other parameters such as input power, system coupling rates, optical losses and detection efficiency. To gauge phonon occupancy, an experiment therefore needs to be properly calibrated. To help in this endeavor, quantum mechanics coincidentally offers a unique way of calibrating such experiments through *sideband asymmetry*.

The concept of sideband asymmetry is strictly quantum mechanical and can be understood through the scattering picture (Fig. 2.5) where the asymmetry is immediately recognizable from the Stokes- and anti-Stokes processes. The fundamental difference is that the Stokes process generates a phonon, whereas the anti-Stokes process requires one as input. So if there are no phonons present on average, the anti-Stokes process will be completely suppressed. The Stokes process on the other hand can happen spontaneously, meaning that the process can be "stimulated" by quantum mechanical vacuum fluctuations. This effect produces an asymmetry between Stokes and anti-stokes scattering rates when $n_{\mathrm{m}} \sim 1$.

To understand the phenomenon quantitatively, we once again turn to the cavity optomechanical CMEs and consider a sideband resolved system pumped with a noiseless laser. We're interested in the output field $\hat{a}_{\mathrm{out,e}}$ and how its interaction with the mechanical mode differs when changing the dominant scattering process (i.e. changing the detuning $\Delta = \pm\omega_{\mathrm{m}}$). From the solutions (Eqs. (B.8),(B.6)), we see that when moving from red to blue detuning, the dominantly coupled mechanical operator changes from $\hat{b}_{\mathrm{in},0}$ to $\hat{b}^{\dagger}_{\mathrm{in},0}$. This manifests in the sideband photon flux of the output mode that is given by the power spectral density defined in Eq. (B.4)

$$\begin{aligned} S_{\hat{a}_{\mathrm{out,e}}}(\omega)\Big|_{\Delta=\mp\omega_{\mathrm{m}}} &= \int \langle \hat{a}^{\dagger}_{\mathrm{out,e}}(\omega')\hat{a}_{\mathrm{out,e}}(\omega)\rangle \mathrm{d}\omega' \\ &\approx \frac{\gamma_{\mathrm{om}}\gamma_0\eta_{\mathrm{o}}}{(\omega\mp\omega_{\mathrm{m}})^2 + (\gamma_0 \pm \gamma_{\mathrm{om}})^2/4}\left(n_0 + \frac{1}{2}(1\mp 1)\right), \end{aligned} \tag{2.36}$$

where in the last step we adiabatically eliminated the optical mode. Eq. (2.36), describes the sideband photon flux as a Lorentzian centered at $\pm\omega_{\mathrm{m}}$ for red and blue detuning respectively (Fig. 2.11). The last factor contains a $(1\mp 1)/2$-term that originates from the bath's quantum mechanical correlators (Eq. (2.22)). Integrating over the sideband yields the total photon flux

$$\begin{aligned} \Gamma|_{\Delta=\mp\omega_{\mathrm{m}}} &= \frac{1}{2\pi}\int \mathrm{d}\omega\; S_{\hat{a}_{\mathrm{out,e}}}(\omega)\Big|_{\Delta=\mp\omega_{\mathrm{m}}} \\ &= \gamma_{\mathrm{om}}\eta_{\mathrm{o}}\frac{\gamma_0}{\gamma_0 \pm \gamma_{\mathrm{om}}}\left(n_0 + \frac{1}{2}(1\mp 1)\right) \\ &\approx \gamma_{\mathrm{om}}\eta_{\mathrm{o}}\left(n_0 + \frac{1}{2}(1\mp 1)\right), \text{ for } C_{\mathrm{om}} \ll 1, \end{aligned} \tag{2.37}$$

where the factor $1/(2\pi)$ comes from the Fourier transform definition (see Eq. (B.5)). We find that for small cooperativities C_{om}, the sideband photon scattering rates differ by exactly one equivalent excitation representing the vacuum fluctuations in the mechanical mode. We use this to calibrate the thermometry experiments described in Chapter 4.

The above derivation gives appreciable understanding for the origin of sideband asymmetry, but it omits two crucial facts that must be mentioned for completeness.

Firstly, the output mode also contains the reflected pump which is not visible in Eq. (2.36). However, the sharp pump tone at ω_{l} is generally filtered away before detection, either through low-pass filtering in

heterodyne detection [76, 21, 77], or by sharp optical filtering when using single-photon detection [70, 49, 78].

Secondly, we assumed a pump laser stripped from classical noise sources such as phase noise or relative intensity noise. It has been shown that classical laser noise at the mechanical frequency can not only drive the mechanics, but can also interfere with the optomechanical sideband[11], causing incorrect estimations of sideband photon flux [79, 80].

The above two points are important experimental considerations that we return to in Sec. 4.2.

[11] With similar physics as what governs EIT.

CHAPTER 3

The release-free optomechanical crystal

At the beginning of this thesis work, release-free silicon optomechanics, and consequently, the release-free optomechanical crystal cavity (OMC) was a largely unexplored concept. Pioneering work by Sarabalis *et al.* in the mid 2010's [81, 82] had shown that both release-free Brillouin active waveguides and particular geometries of OMCs could be supported on silicon-on-insulator (SOI), but efforts had not yet yielded fully desirable results and lacked important features such as sideband resolution. Yet, the promise of thermally stable release-free devices on potentially novel material platforms was an enticing goal and served as the guiding star at the inception of this project.

The work led to the publishing of Paper A which presents the, to our knowledge, first demonstration of a sideband-resolved release-free optomechanical crystal[1]. The release-free OMC has since its conception been the basis of other nanofabricated devices such as microwave-optic transducers [83, 84] and electromechanical crystals [85]. In this chapter we give further context to the inception of the release-free design and expand on the methods and measurement results presented in Paper A.

[1]The attentive reader notices that *clamped* is used to describe the thermal anchoring in Paper A. This was in later papers changed to *release-free*, both to comply with the terminology of Sarabalis [82], but also to resolve the – perhaps understandable – confusion it regrettably caused.

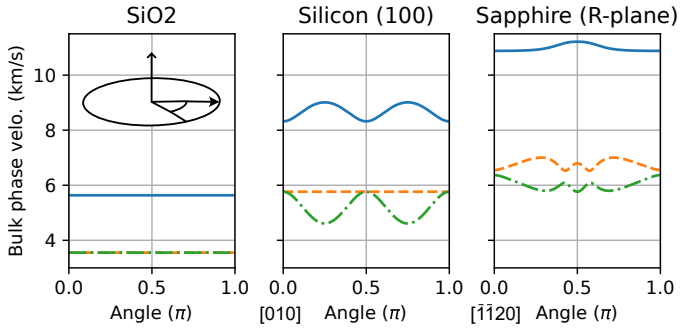


Figure 3.1: Bulk phase velocities for materials studied in this thesis. The velocities are calculated in the given material plane for an angle range of π radians which spans the full range of velocities due to symmetry. Blue curves represent compressional waves whereas orange and green curves give velocities for out-of-plane and in-plane sheer waves, respectively. Stiffness matrix coefficients for sapphire are extracted from Ref. [86].

3.1 Design

3.1.1 Total internal reflection for acoustic waves

The obvious problem one tackles when designing release-free OMCs is the risk of increased phonon loss through the substrate. A pathway for increased heat dissipation could as well act as an extra decay channel for the optomechanically important coherent phonons. However, despite this increased contact between device layer and substrate, the wave nature of the acoustic radiation can still allow for efficient confinement which is achieved through careful engineering and material choices.

To understand this in detail we turn to the optical fiber which here can be considered an optical analogy for the acoustics. In a standard solid-core optical fiber, light is confined to the fiber core even though a continuum of radiation modes is present in the cladding. The principle behind this confinement is well-known and commonly referred to as total-internal-reflection (TIR). The common strategy to achieve TIR is to have a core with a lower phase-velocity (or higher refractive index in the case for optics) than the surrounding cladding. This ensures that a guided mode's wave vector component along the propagation direction is larger than any of the available modes in the cladding continuum, making any

scattering prevented through momentum conservation[2].

Due to their wave-nature, acoustic vibrations in solid materials have similar properties to optical waves, and as such, are also governed by principles such as TIR. Naturally, one therefore looks to design release-free acoustic waveguides in device layers with low phase-velocities compared to their surrounding substrate. The bulk phase velocities of the materials studied in this thesis are presented in Fig. 3.1 from which we see that materials such as sapphire is a promising substrate for release-free silicon optomechanics. However, the quality of the device layer and material bonding is also of prime importance which is not guaranteed for all material stacks.

3.1.2 Unpatterned release-free optomechanical waveguides

Guided by the principles of TIR, we start the design process by studying unpatterned release-free optomechanical waveguides (OMW). A convenient starting point comprises a rectangular waveguide cross section where the waveguide bottom surface is fully attached to a substrate that covers the lower half plane (Fig. 3.2). Note that the coordinate system is now changed w.r.t. Sec. 2.2 to comply with conventions in the field. The device layer is chosen to be a (100) crystalline silicon plane with crystal orientation such that the [110] direction is parallel to the waveguide. For the substrate, we choose a sapphire R-plane which effectively highlights the design principles of release-free optomechanics due to its high speed of sound (Fig. 3.1). The SOI material platform, out of which the devices in the thesis' appended papers are fabricated, is a natural extension that will be treated as a special case later. We thus proceed with a silicon-on-sapphire (SOS) release-free OMW.

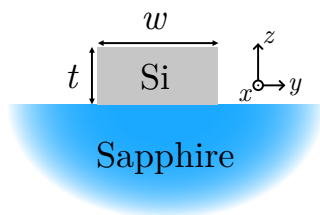


Figure 3.2: Cross section of unpatterned release-free OMW with thickness t and width w.

Dispersion diagrams for both optical and mechanical modes of this system are readily available through finite-element simulations using COMSOL. We study a 500 nm wide waveguide made from a 220 nm

[2]Formally the wave vector can be seen as quasi-momentum, containing contributions from the electromagnetic properties of the material.

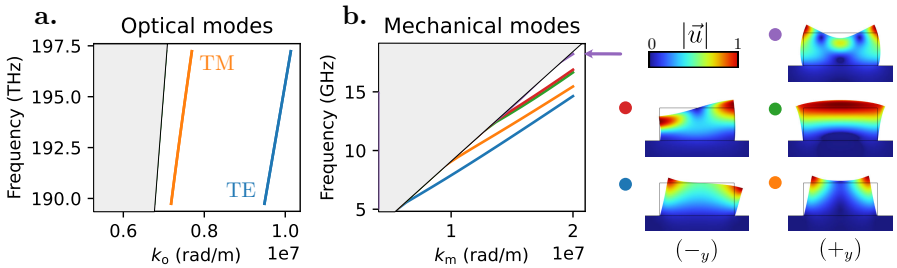


Figure 3.3: Band diagrams for a 220 × 500 nm silicon OMW on an R-plane sapphire substrate. **a.** The optical band diagram consists of transverse electric (TE) and transverse magnetic (TM) modes of which the TE-like mode is most confined to the silicon. **b.** Five mechanical modes confined to the device layer can be found for high mechanical wavenumbers, three with positive symmetry about $y = 0$ $(+_y)$ and two with negative $(+_y)$.

tick device layer and present its dispersion in Fig. 3.3. Being release-free, both optical and mechanical band diagrams feature a continuum of modes that are separated from guided modes by the *light cone* for optics and the *Rayleigh cone* for mechanics. The slope of the Rayleigh cone is set by the lowest phase velocity surface acoustic waves (SAW) and bulk acoustic waves (BAW) in the substrate. For R-plane sapphire, this lower limit is set by Rayleigh-type SAWs with phase velocity around 5800 m/s [83]. For sufficiently high wavenumbers, mechanical modes fully guided in the device layer emerges from the continuum which can be used for Brillouin interactions. This stands in contrast to an identical OMW fabricated on an SiO_2 substrate. The SOI platform does not generally support guided mechanical modes due to the wider Rayleigh cone of the SiO_2 substrate. However, as alluded to earlier, guided mechanics is not impossible in SOI OMWs. This was shown in the early work by Sarabalis [81, 82] and will be further explored in Sec. 3.1.3.

For release-free OMWs, symmetry in the substrate normal direction (z) is inherently broken due to the presence of the substrate. In the waveguide transverse direction (y) however, symmetry is given by the properties of each mode. While intramodal scattering can only reach significant coupling with positive transverse symmetry $(+_y)$, intermodal scattering can utilize $(-_y)$-symmetry to scatter between optical modes of opposing symmetries [87]. In this work, we focus on intramodal scattering and thus favor modes with $(+_y)$ symmetry.

The process of calculating optomechanical coupling for the release-free OMWs begins with choosing ingoing optical and mechanical modes.

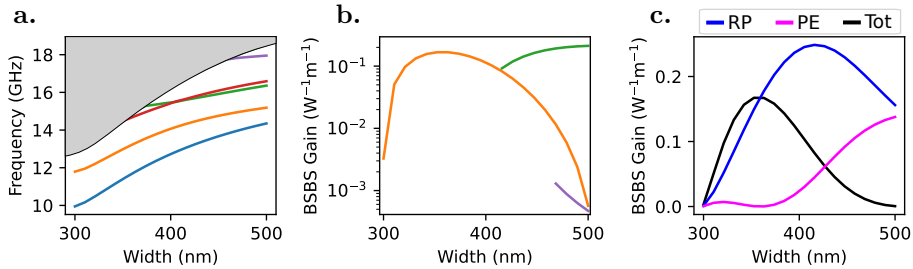


Figure 3.4: BSBS gain ($\mathcal{G}/Q_\mathrm{m}$) in a $t = 220\,\mathrm{nm}$ SOS release-free OMW with variable width. **a.** Mechanical modes and Rayleigh cone. Color coding for the mechanical modes matches Fig. 3.3b. **b.** Total intramodal BSBS gain for the mechanical modes in **a** with identical color coding. Gain is calculated with the TE-like optical mode in Fig. 3.3a. **c.** Intramodal BSBS gain with photoelasticity (PE) and moving boundary (MB) contributions for the lowest frequency ($+_y$) symmetry mode (orange in **a** and **b**).

For intermodal scattering, two optical and one mechanical mode are chosen, whereas for intramodal scattering, only one optical mode is required. Next, we must choose whether to calculate the coupling for backward stimulated Brillouin scattering (BSBS) or forward stimulated Brillouin scattering (FSBS). The mutual direction of ingoing and outgoing optical modes is important for release-free optomechanics since it determines the wavenumber for the mechanics through the phase matching condition

$$k_\mathrm{o} = k'_\mathrm{o} + k_\mathrm{m}. \tag{3.1}$$

Here k_o (k'_o) is the wavenumber of the ingoing (outgoing) optical mode and k_m is the resulting mechanical wavenumber[3]. In FSBS, the interacting optical modes co-propagate, which generally stimulates long-wavelength ($k_\mathrm{m} \approx 0$) mechanical modes. On the contrary, BSBS features counter-propagating optical waves, which stimulate mechanical modes with approximately half the optical wavelength ($k_\mathrm{m} \approx -2k_\mathrm{o}$). The high mechanical wavenumbers stimulated by BSBS are beneficial for release-free optomechanics to evade the Rayleigh cone (Fig. 3.3b). This reduces the effectiveness of intramodal FSBS since its stimulated mechanical modes generally fall within the Rayleigh cone and are thus lost to the continuum. Therefore, we mostly consider BSBS when calculating Brillouin gains.

We use the theory established in Sec. 2.2 and App. B.3 to calculate the optomechanical coupling strength in terms of intramodal BSBS gain

[3]We now use k_m and ω_m to denote mechanical wavenumber and angular frequency.

$\mathcal{G}/Q_{\mathrm{m}}$. We do this for all available mechanical modes while using the TE-like mode at 1550 nm as optical input and output (Fig. 3.4). Of the five modes presented in Fig. 3.3b, only the three with $(+_y)$ symmetry yields non-zero gain on account of the overlap integrals being linear in $\vec{u}$ (Eq. (B.13)). However, even the modes with correct symmetry have around 2 orders of magnitude lower Brillouin gain compared to similar suspended waveguides [88, 89, 59]. One of the reasons for this low total gain is that the overlap integrals for PE and MB is comparable in magnitude but opposing in sign, therefore causing cancellation (Fig. 3.4c).

Another issue is that the available mechanical modes that generate non-zero Brillouin gain with guided mechanics have frequencies greater than 10 GHz. We will later discuss the integration of release-free optomechanics in a hybrid quantum system to be integrated with transmon qubits. For efficient coupling between qubits and mechanical modes, their frequencies must match, making mechanical frequencies in the qubit frequency range around 5 GHz more desirable.

However, both of the above issues has a simple solution when expanding the design space beyond translationally invariant waveguides. In the next subsection we exchange translational invariance for discrete periodicity, which we will see allows for both stronger coupling and lower mechanical frequencies.

3.1.3 Patterned waveguides and the pinch mode

Introducing a discrete periodicity to waveguides through a patterning of holes is a common strategy to engineer the dispersion of both optical and acoustic modes within a waveguide. This is the design philosophy of OMCs and can also be exploited for applications such as optical storage with slow-light waveguides [90, 91]. In release-free OMWs it also serves the important role of introducing the waveguide to additional surfaces. Although surfaces are commonly associated with material imperfections, they are also important for optomechanical coupling through to the MB effect.

Since the MB effect is only present at material interfaces, waveguide surfaces can contribute to a large part of the total optomechanical coupling. This is especially important in silicon which has weaker photoelastic interactions as compared to materials as chalcogenide glasses [92]. To achieve a strong MB interaction, it is required that a significant part of the mechanical mode displacement is perpendicular to boundaries where the electric field is strong (Eq. (2.10)). This leads to a weak MB

interaction for mechanical modes where the majority of the displacement is in the waveguide material bulk. By cutting holes in the waveguide, we introduce surfaces that are perpendicular to longitudinal waveguide motion which otherwise would not be contributing to the MB interaction. The electric field in the waveguide center can also be strong, further increasing the potential of a strong MB contribution.

In addition, patterning the waveguides with holes – and thus increasing its surface-to-volume ratio – also reduces the frequencies of the available mechanical modes through *geometrical softening* [81]. This geometric effect is unique to acoustic waves and stems from the free boundary conditions on surfaces bordering to vacuum. Atoms on the surface of a solid have fewer neighboring atoms than those in the bulk, and will thus experience a weaker restoring force when displaced. This reduces the effective stiffness of the material and lowers available resonance frequencies. This is the same principle that allows for confined SAWs and thus also SAW-based devices [93, 73].

To see the above principles applied in action, we study a periodic release-free OMW by performing finite-element simulations on a unit cell structure with periodic boundary conditions in the waveguide longitudinal direction. For now, we continue with the SOS material platform from the previous section and define the unit cell by extruding the waveguide cross section by a period length a (Fig. 3.5). Finally, we etch a elliptical hole concentric with the unit cell through the waveguide device layer with principal axis lengths h_x, h_y. As in 2D OMW cross section simulations, optical and mechanical eigenmode frequencies and fields are given for each predefined wavenumber $k_\mathrm{o}, k_\mathrm{m}$.

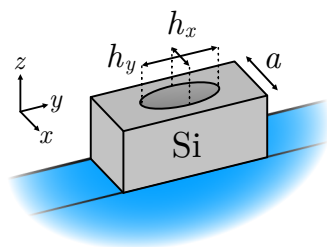


Figure 3.5: Release-free OMW unit cell with period a and elliptical hole parameters h_x and width h_y.

The simulation results for a unit cell with parameters $\{a, t, w, h_x, h_y\}$ $= \{188, 220, 662, 94, 321\}$ nm are presented in Fig. 3.6, where t and w denote the thickness and width of the waveguide, respectively. In the optical band structure, we find a TE-like mode at $k_\mathrm{o} = 0.5\pi/a$. This mode will be the primary choice for optomechanical coupling due to phase matching considerations. Looking to the mechanical band diagram, we

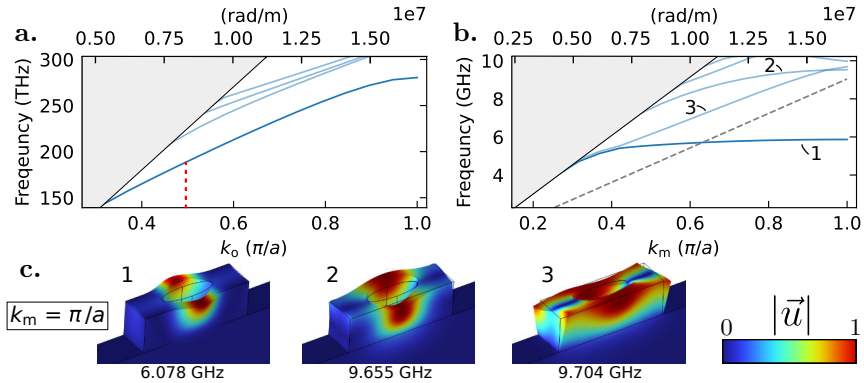


Figure 3.6: Dispersion diagram for a release-free SOS unit cell. Geometrical parameters are found in the main text. **a.** Optical dispersion diagram. Wavenumbers in the longitudinal direction is now given in terms of π/a where a is the unit cell period. **b.** Mechanical dispersion diagram with modes marked 1-3 representing the mode shapes in **c**. The solid continuum is bounded by the Rayleigh cone for the sapphire substrate. The gray dashed line represents the Rayleigh cone for an SiO_2 substrate ($v_{SAW} = 3400\,\mathrm{m/sec}$). **c.** Mechanical mode profiles at $k_m = \pi/a$ for the three lowest frequency modes in the unit cell. Mode 1 is referred to as the "pinch" mode.

see that the dispersion is less trivial compared to the unpatterned structure (Fig. 3.3b) and that frequencies are significantly lower at high k_m due to geometrical softening. At the edge of the Brillouin zone, the lowest frequency mode even falls below the Rayleigh cone for an SiO_2 substrate[4] – an essential prerequisite for the SOI-guided mechanics used in the thesis' appended papers. The lowest frequency mechanical mode has displacement primarily in the waveguide longitudinal direction. This is a version of the "pinch" mode that was first presented along with the initial suspended OMC designs [19] and, as it turns out, is exceptionally well suited for release-free optomechanics.

Comparing the release-free unit cell design in Fig. 3.6 to that of a conventional suspended OMC with breathing mode mechanics [26], the stark difference is in the shape and periodicity of the holes. The release-free design deploys tightly spaced holes with elliptical principal axis lengths satisfying $h_y/h_x \approx 2$. A shorter periodicity a increases the span of available longitudinal wavenumbers by increasing the size of the first Brillouin zone $\mathbb{B}_0 = \{-\pi/a, \pi/a\}$. To have available guided mechanical modes in

[4]For SiO_2, we use the SAW velocity $v_{SAW} = 3400\,\mathrm{m/s}$ to define the Rayleigh cone [94].

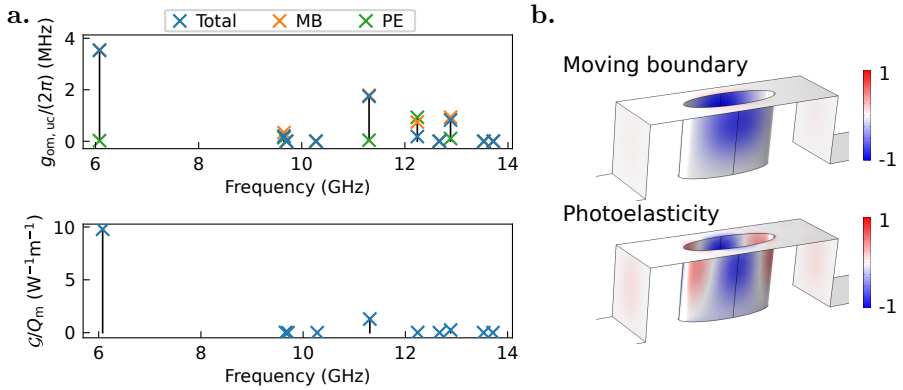


Figure 3.7: a. Intramodal BSBS unit cell coupling $g_{\mathrm{om,uc}}$ and equivalent total Brillouin gain $\mathcal{G}/Q_{\mathrm{m}}$ for 10 mechanical modes in the SOS unit cell ($k_{\mathrm{m}} = \pi/a$ in Fig. 3.6b). $g_{\mathrm{om,uc}}$ is shown with MB and PE contributions. To satisfy BSBS phase matching, we choose the optical mode at $k_{\mathrm{o}} = 0.5\pi/a$. **b.** Normalized real component of the MB and PE integrands (see Eq. (B.16)) on the unit cell surfaces when calculated for the pinch mode at $\omega_{\mathrm{m}}/(2\pi) = 6.078\,\mathrm{GHz}$.

the device layer, the first Brillouin zone must include wavenumbers that support modes outside the Rayleigh cone (Fig. 3.3). We discuss this design consideration in Paper A and conclude that periods of around $a \approx 200\,\mathrm{nm}$ are well suited for release-free optomechanics on both SOS and SOI.

Finally, we look at the optomechanical coupling in the unit cell. For optimal mechanical confinement, we choose the Brillouin zone edge (X-point) as operating point in the mechanical dispersion diagram ($k_{\mathrm{m}} = \pi/a$) which constrains the optical wavenumber to $k_{\mathrm{o}} = 0.5\pi/a$ through BSBS phase-matching (Eq. (3.1)). In these unit cell simulations, we use the standard 3D formulation of the optomechanical overlap integrals to calculate the unit cell coupling $g_{\mathrm{om,uc}}$ while making sure to adapt them for BSBS (see App. B.4). To properly compare the result to the unpatterned case, we also convert the unit cell coupling to Brillouin gain using (2.24) with $L = a$.

When calculating both couplings and gains for all mechanical modes up to 14 GHz, the pinch mode at 6.078 GHz clearly stands out as the strongest coupled (Fig. 3.7). The unit cell coupling rate $g_{\mathrm{om,uc}}/(2\pi) = 3.5\,\mathrm{MHz}$ is equivalent to $\mathcal{G}/Q_{\mathrm{m}} = 9.7\,(\mathrm{Wm})^{-1}$ – almost a factor 100 larger than what was achieved in the unpatterned waveguide (Fig. 3.4). As in the unpatterned waveguide case, the contributions from MB and

PE are generally opposing in the unit cell simulation; however, this does not affect the total coupling severely due to the MB effect being largely dominant.

The large calculated $\mathcal{G}/Q_{\mathrm{m}}$ for the pinch mode is comparable to similar Brillouin-active waveguides in integrated silicon photonics [92]. This is in part due to the slow-light effects achieved in a periodic waveguide [90]. Previous silicon demonstrations with high gain commonly rely on FSBS or co-propagating intermodal scattering which generally stimulate mechanical modes within the Rayleigh cone. Due to the BSBS interaction however, the pinch mode offers strong coupling while simultaneously being completely shielded from the mechanical continuum, enabling high mechanical quality factors without waveguide suspension. These properties make the pinch mode uniquely suited for serving as base for designing full release-free optomechanical crystal cavities.

3.1.4 Release-free optomechanical crystal cavities

An optomechanical crystal cavity (OMC) consists of three essential parts: (1) the defect region consisting of unit cells which support optical and mechanical modes close to the desired frequencies which couples strongly, (2) two surrounding mirror regions which are designed to reflect radiation from the defect region, and (3) the transition region which bridges mirror and defect. While the unit cell from the last subsection will serve as the defect unit cell, we design a second release-free unit cell serving as the mirror unit cell. The transition region is then formed as a set of unit cells with parameters that smoothly transition between those of the mirror and defect regions. The design principles we employ for the release-free OMCs are similar to those used in suspended optomechanical crystal design [95] and will not be explained in detail here, but there are some interesting differences that are worth mentioning.

The purpose of the transition region is to deform the the unit cell band structure between defect and mirror unit cells. Localized defect modes are achieved when the mirror cell has bandgaps at the defect resonance frequencies[5]. For the pinch mode, the chosen operating point ($k_{\mathrm{m}} = \pi/a$) attains the highest mechanical frequency for that mode in the first Brillouin zone, causing even a tiny unit cell deformation that pulls the band towards lower frequencies to immediately open up a bandgap

[5]In fact, it is sufficient for some of the transition region unit cells to posses bandgaps at the desired frequency to reach appreciable quality factors in both simulation and measurement. This is demonstrated in Papers A and B.

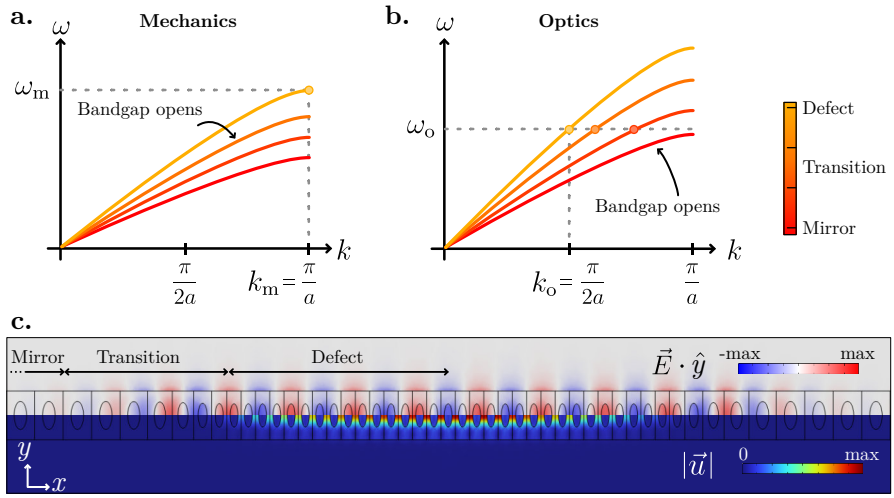


Figure 3.8: a./b. Sketch of optical/acoustic band diagrams in the unit cells under defect-to-mirror deformation. The defect mechanical mode at $k_\mathrm{m} = \pi/a$ is immediately pulled into the bandgap upon unit cell deformation while the optical mode (initially at $k_\mathrm{o} = 0.5\pi/a$) requires a greater deformation to fully open up a bandgap at ω_o. **c.** Optical and acoustic field distributions in a release-free OMC with $N_\mathrm{d} = 31$ and $N_\mathrm{t} = 7$.

(Fig. 3.8a). On the contrary, the optical mode at $k_\mathrm{o} = 0.5\pi/a$ has available states for both lower and higher frequencies around ω_o. A bandgap is not opened up until the deformation is large enough to remove all states with $\omega > \omega_\mathrm{o}$ (Fig. 3.8b). A consequence of the delayed opening of the optical bandgap is that the optical mode penetrates further into the transition compared to the mechanics. For modes with Gaussian spatial for the field spatial envelopes, optimal coupling is generally achieved for optical and mechanical modes satisfying $L_\mathrm{o} = \sqrt{2}L_\mathrm{m}$, where $L_\mathrm{o/m}$ is the full-width-half-maximum (FWHM) spacial extent of the optical/mechanical mode in the OMC longitudinal direction [96]. Due to the delayed optical bandgap, the optical mode generally gives $L_\mathrm{o} \gg L_\mathrm{m}$, resulting in a non-optimal total coupling.

A counteraction to the problem of non-optimal spatial overlap is to increase the size of the defect region in relation to the transition. This causes the non-optimal tapering of the modes in the transition region to have a lower impact on the total overlap. In Paper A, the number of defect unit cells is $N_\mathrm{d} = 31$ compared to the transition unit cells $N_\mathrm{t} = 7$ (Fig. 3.8c). This longer OMC achieves satisfactory mode overlap

but suffers in sheer mode volume which also lowers coupling roughly according to $N_{\mathrm{d}}^{-1/2}$ [96]. For this release-free OMC design, overlap and mode volume counteract almost perfectly while increasing the OMC size, making the achieved coupling in long OMCs comparable to short designs with $N_{\mathrm{d}} = 1$. From a thermal noise perspective, a larger mode volume also increases thermal transport area to the chip bulk which is a desirable property from the perspective of low noise optomechanics (Sec. 4.3.2). However, a longer OMC is more susceptible to fabrication imperfections which is discussed further in Sec. 3.3.3.

In summary, the design process laid out in this section yields release-free OMCs with localized modes for both SOS and SOI material platforms, where the latter is dependent on geometrical softening. For SOI, both short OMCs with $N_{\mathrm{d}} = 1$ and longer designs with $N_{\mathrm{d}} = 31$ yield coupling rates of $g_{\mathrm{om}}/(2\pi) \approx 500\,\mathrm{kHz}$. Coupling rates tends to be slightly higher in SOI compared to SOS (around 20%) which is likely due to the higher index sapphire substrate pulling the optical mode away from regions of high mechanical energy.

Lastly we comment on simulated optical and mechanical losses. In SOI, quality factors with scattering as primary loss mechanism exceeds 10^6 and 10^5 for optics and mechanics, respectively [94]. In SOS, higher optical scattering losses are expected due to the wider light cone of sapphire compared to SiO_2. The opposite is true for mechanics leading to higher radiation-limited mechanical quality factors for SOS compared to SOI.

3.2 Fabrication

With the design of the release-free devices finished, we now turn to fabrication. The OMC is a relatively simple device. Even so, to achieve high quality samples, utmost care must be executed in all steps of the fabrication, from material choice, lithography, etching, and cleaning. This section covers the silicon processing that yielded the measured devices during this thesis work. We give detailed information about our SOI processing; however, due to its early development stage and lack of published results, details on SOS fabrication will not be given in this thesis.

For fabricating release-free OMCs on SOI, we start with 8" SOITEC wafers with a 220 nm device layer ($\sigma > 750\,\Omega \cdot \mathrm{cm}$) and 2 µm thermal buried oxide (BOX). We dice the SOI wafers in 5×10 cm chips with an in-house physical dicing system (Disco DAD3350) for rapid prototyping.

Over the course of this thesis work, many samples were fabricated while optimizing fabrication recipes and device designs. This means that the presented devices in this thesis are not guaranteed to have been fabricated with identical process parameters or tools, as tool availability and performance varies in a shared clean room with many users. As such, this section only covers the broad strokes of the fabrication processes that yielded measurable devices during this thesis work. We present the most important process steps with notes in Tab. 3.1.

3.2.1 Silicon dry-etching

Arguably the most intricate step of release-free OMC fabrication is the etching which transfers the design pattern into the silicon device layer. In this process, all vertical surfaces of the devices are defined which are responsible for both positive properties such as MB optomechanical coupling, but also introduce optical and mechanical scattering losses. In addition, it is believed that dry etching can leave the remaining material surface with a damaged crystalline structure and/or unwanted ion implantation [97] which may have a significant impact on absorption induced thermal mechanical noise. This is further explained in Sec. 4.1.1.

Etching of silicon nanostructures is most commonly performed through inductively coupled plasma (ICP) reactive ion etching (RIE). Through both chemical and physical action, plasma ions remove chip material uncovered by protective resist. Common elements used for silicon processing are F, Cl and Br. Methods based on fluorine are generally referred to as pseudo-Bosch techniques where etch gases such as SF_6 are used in combination with a polymer-depositing gas such as C_4F_8 to control selectivity and etch anisotropy [98]. Fluorine-based etching has seen much success in silicon photonics and has produced photonic crystal devices with internal Q-factors exceeding 10^7 at $\lambda = 1560\,\mathrm{nm}$ [99]. A fluorine-based pseudo-Bosch is also routinely used for silicon OMCs and has produced internal Q-factors of 10^6 for optics and 10^{10} for mechanics [100, 76]. Although not as common for silicon optomechanical crystals, a fluorine-based chemistry can also be used with O_2 as passivation gas at cryogenic temperatures [101].

Table 3.1: Outline of SOI release-free OMC fabrication process.

Process Step	Description
Spin e-beam resist	ARP6200-9 and -13 is both used with comparable success. The thicker ARP6200-13 resist is diluted with anisole at a ratio of 2:1 (resist:anisole).
E-beam lithography	E-beam system: Raith EBPG 5200. Smoother silicon sidewalls are attained through a multi-pass routine which divides the dose in sensitive exposure areas over up to 4 passes.
Development	O-xylene development of ARP6200 resist.
Etching	RIE with Cl- and HBr-based chemistry. More details below.
Resist removal and surface treatment	Piranha solution with 3:1 concentration (H_2SO_4:H_2O_2) followed by 2 % hydrofluoric acid (HF) to remove native oxides. Oxide strip must be quick to avoid sacrificing buried oxide.
(OMC suspension)	For comparison to our release-free devices, we also fabricate OMCs with a final suspension step using either 15% HF or vapor HF with an SPTS uEtch tool.

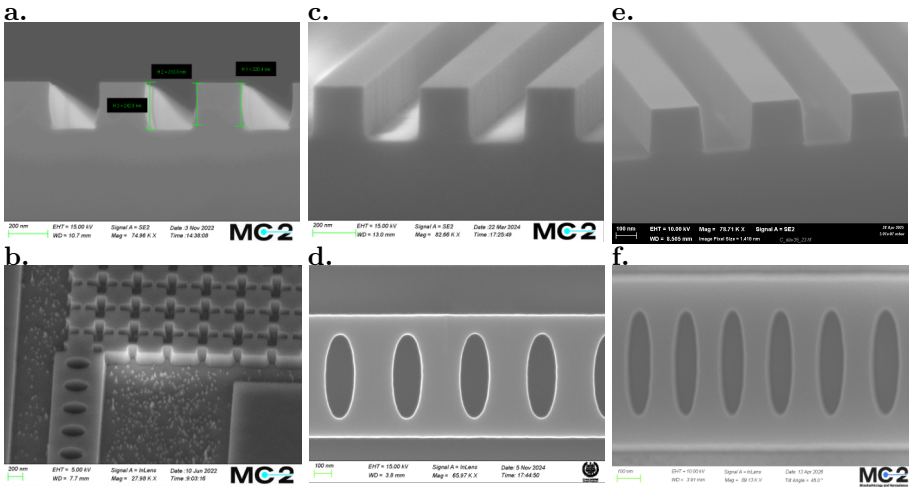


Figure 3.9: Silicon etching with three different recipes and tools. **a-b.** Cl_2+HBr in an STS Multiplex ICP etcher. The cross section reveals a slight footing and a 20 nm undercut of the SiO_2 due to the short 2% HF surface treatment (Tab. 3.1). When the breakthrough etch fails, silicon nano-grass can be observed. **c-d.** Cross section and vertical hole profiles with a pseudo-Bosch etch in an Oxford PlasmaPro 100. This etch produces a near perfect sidewall verticality and well-defined OMC holes. **e-f.** Cl_2+HBr in an Oxford PlasmaPro 100. The sidewall angle is approximately 5° off vertical.

The alternative to fluorine-based etching are techniques using Cl and Br. Compared to F, Cl and Br etches silicon with high selectively with respect to SiO_2 without added polymer deposition. This allows for SiO_2 to be used as passivation layer without cryogenics. Therefore, common techniques use gases such as Cl_2 and/or HBr in combination with O_2 to control selectivity, anisotropy and etch rates [102, 103]. As with pseudo-Bosch etching, Cl- and Br-based chemistry has been successfully used for optomechanical crystal fabrication [28, 104].

The tools available during this thesis work allowed for trials with both F- and Cl+Br-based etching. Recipes for both methods were developed across multiple tools. The quality of the etch is gauged from several different aspects: (1) accuracy of design transfer in the top silicon surface, (2) etched sidewall angle, (3) sidewall and line roughness, (4) optical quality factors.

The devices featured in Papers A and B were fabricated with a Cl_2+HBr etch in an STS Multiplex ICP tool. The development of the recipe involved optimizing the initial oxide breakthrough step and the

Table 3.2: Process parameters for Cl_2+HBr etching of silicon in an Oxford PlasmaPro 100. The breakthrough step physically etches the native oxide which otherwise acts as a stop layer for the main etch. We run the main etch until the silicon device layer is fully etched through by monitoring progress with laser end point detection. When etched through, we keep etching in an over-etch to make sure that small features which can etch slower are also through-etched. Nominal etch rate for the main etch is $\sim 35\,\mathrm{nm\,min^{-1}}$

Parameter	**Unit**	**Breakthrough**	**Main Etch**
ICP RF	W	800	250
Table RF	W	110	60
Cl_2 flow	sccm	0	20
HBr flow	sccm	40	50
O_2 flow	sccm	0	2
Temperature	°C	25	25
Time	sec	10	End point

ratio of O_2 to Cl_2 and HBr flow. Failing to break through the silicon native oxide leaves passivated patches which leads to the formation of silicon nano-grass [105] in the etched regions (Fig. 3.9a). Increasing the breakthrough time and power generally allows for physical removal of the native oxide if the chamber O_2 content is not too high. The final recipe produced grass-free samples with decent sidewall roughness. Despite imperfect sidewall verticality, this etch produced devices with optical quality factors of up to $280 \cdot 10^3$ [94].

Since the fabrication of the device presented in Papers A and B, two other tools have been used to fabricate samples. A pseudo-Bosch recipe was developed in an Oxford Plasma Pro 100 tool which produced almost perfectly vertical sidewalls with very low roughness. Due to malfunctioning of this pseudo-Bosch tool, another Cl_2+HBr etch based on the etch in the STS tool was also developed in a separate PlasmaPro 100 with recipe details inspired by [106]. This etch is the currently stable version in use at the writing of this thesis and was used in the fabrication of the transducer device in Paper C. This etch has been shown to produce optical quality factors in release-free OMCs exceeding $500 \cdot 10^3$.

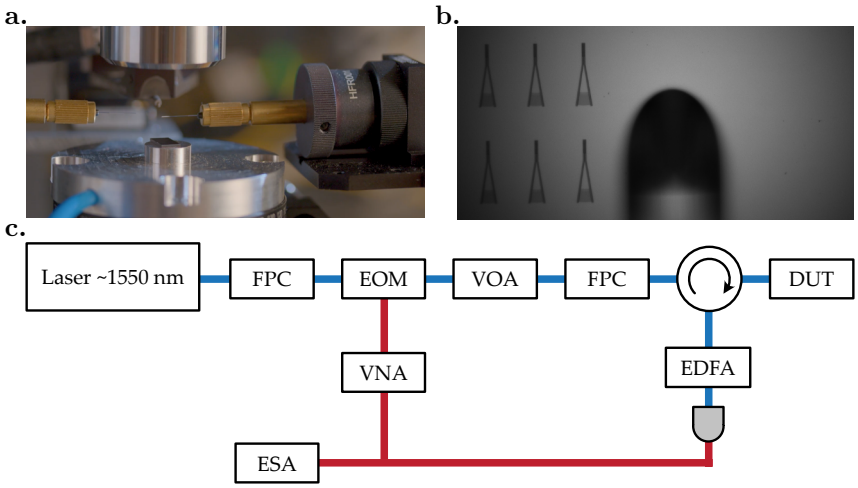


Figure 3.10: Room temperature characterization setup. **a.** Chip mounting pedestal with vertically mounted microscope for fiber alignment. Fibers mounted on motorized stages guide light to and from the chip via on-chip grating couplers. A microwave probe (background) is used to couple in microwave signals for transducer measurements. **b.** Microscope view showing the angle-cut fiber tip and on-chip devices. **c.** Diagram of room temperature optical experimental setup. FPC: Fiber polarization controller, EOM: Amplitude electro-optic modulator, VOA: Variable optical attenuator, DUT: Device under test, EDFA: Erbium-doped fiber amplifier, VNA: Vector-network analyzer, ESA: Electrical spectrum analyzer.

3.3 Room-temperature measurements

The first step toward thermal noise characterization at cryogenic temperatures is to gauge the properties of the device under test (DUT) in room temperature. The room temperature experimental setup is designed for rapid characterization of optomechanical properties of OMCs and micro-ring resonators (Fig. 3.10). In addition, microwave probe access was later made available to allow for the transduction experiments presented in Paper C. The results of room temperature characterization of release-free SOI OMCs is in majority presented in Paper A; however, this section gives additional information that was either cut from the manuscript or obtained after publication.

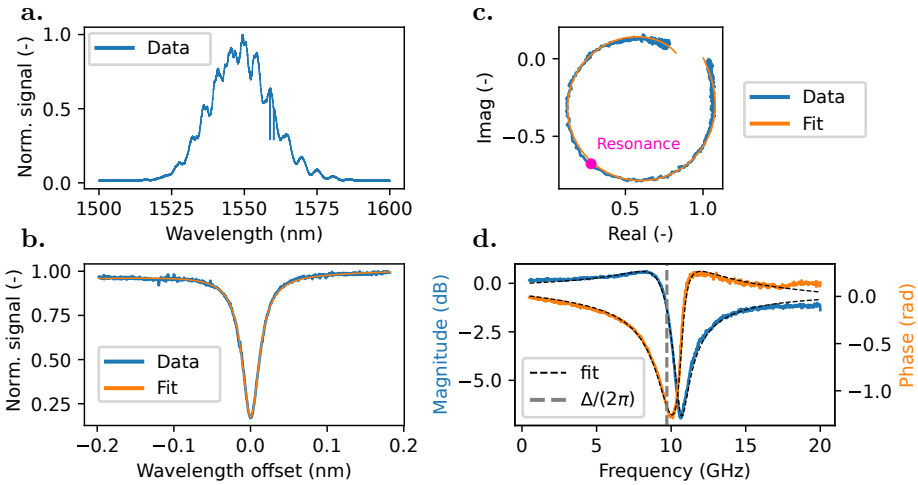


Figure 3.11: Optical OMC characterization. **a.** Normalized OMC reflection spectrum. After fiber-chip coupling via a grating coupler, light at the correct wavelength interacts with the OMC before reflecting off a Bragg-reflector. The reflection is coupled back into the fiber through the same above mentioned grating. **b.** Single-tone spectroscopy of an OMC optical mode with Lorentzian fit. **c./d.** Two-tone optical spectroscopy using a pump and a swept sideband. The beat note is detected on a high-speed photo-detector (HSPD) and measured with a vector network analyzer (VNA) to yield a compex Lorentzian response from which the detuning Δ is extracted.

3.3.1 Optical properties

The main laser of the room temperature setup is a tunable Santec TSL570 external cavity diode laser (ECDL). This laser serves as a rapid characterization laser with fast scan speeds with decent reliability over the GHz level tuning required to gauge optical linewidths.

To couple light from optical fibers to the on-chip devices, we use angle cut fibers together with on-chip grating couplers. The grating coupler design is inspired by the two-step apodized grating couplers presented in Ref. [107]. The gratings provide an approximately Gaussian transmission spectrum (Fig. 3.11a) with center wavelength and insertion loss (IL) both set by grating and fiber properties [108]. At maximum transmission, we measure different grating IL depending on the material platform. For the SOITEC SOI, we reach a minimal IL of 4.4 dB. Other grating couplers fabricated on a 220 nm Shin-Etsu SOI platform with 3 µm BOX reach a minimal grating IL of 3.2 dB, likely due to a more optimized light incidence angle [107]. For SOS chips, the minimally attained grating IL

is around 5 dB. Other fiber-chip coupling methods such as edge-coupling [109] or tapered fibers [110] could be employed but was not prioritized to reduce alignment and fabrication complexity. In addition, grating couplers allow for easy access to devices across the entire chip surface which is important for the full piezo-optomechanical transducer Sec. 5.3.

After finding the OMC resonances in the grating spectrum, we measure their optical properties by sweeping the tunable laser and recording the reflected light on a photo-diode (Fig. 3.11b). This measurement yields the total optical loss κ and a measure of how well internal and external optical losses are matched in form of the resonance extinction (or dip depth). We determine the optical coupling $\eta_\mathrm{o} = \kappa_\mathrm{e}/\kappa$ by investigating the optical extinction as a function of bus waveguide distance [111] or through optical two-tone spectroscopy (Fig. 3.11c/d). We perform two-tone spectroscopy with the Electromagnetically induced transparency (EIT) setup described in Sec. 2.4.3 which measures the complex optical reflection response of the OMC through the beating between a swept sideband and an optical pump [112]. The response is approximately a complex Lorentzian which we fit with a custom resonator fitting package in Python [113].

3.3.2 Mechanical properties

With optical properties of the devices measured, we use the optomechanical interaction to probe the mechanical modes of the OMC devices. Using the principles described in Sec. 2.4.1, we generate optomechanical sidebands on a pump laser by placing it in the vicinity of the OMC optical mode. All devices presented in this thesis are sideband-resolved ($\omega_\mathrm{m} > \kappa$), meaning that a non-zero detuning Δ produces a measurable beating between the sidebands and the pump [17]. We detect the beating on an HSPD (Fig. 3.10c) which produces a power spectrum in the generated radio-frequency (RF)-signal at the mechanical frequency.

By measuring the power spectrum with an electrical spectrum analyzer (ESA) we can fit for the mechanical susceptibility (Eq. (2.27)) to receive the optomechanically altered dissipation rate $\gamma_\mathrm{m} = \gamma_0 \pm \gamma_\mathrm{om}$ (Fig. 3.12a). By sweeping the input power and converting to intracavity photons n_c, the optomechanical coupling g_om can be calculated through a linear fit (Fig. 3.12b). When only accounting for optomechanical backaction, the linear slope is expected to be equal in magnitude on both red and blue side, differing only by a sign. However, due to several reasons, this is commonly not the case and has the risk of corrupting coupling

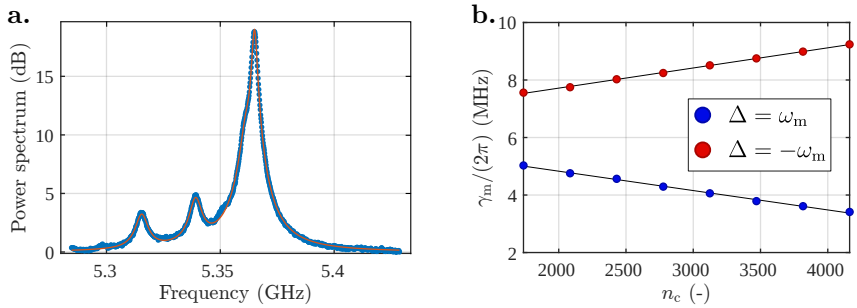


Figure 3.12: a. Normalized room temperature thermomechanical spectrum of the release-free OMC presented in Papers A and B. We fit the signal to a sum of Lorentzians representing the different orders of the pinch mode within the OMC [83]. **b.** Optomechanical backaction for the mechanical mode at $\omega_m/(2\pi) = 5.365\,\text{GHz}$ in **a**. Measured optomechanical coupling is $g_{om}/(2\pi) = 0.5\,\text{MHz}$.

results. To attain accurate results for g_{om}, the optical resonance must first not have significant Fano-like features which does not guarantee that $n_c(\Delta) = n_c(-\Delta)$ for the same input power [114]. Secondly, thermal contributions to the n_c-dependent γ_m is independent of Δ and can thus introduce asymmetry to the backaction curves [115]. In the context of cryogenic silicon OMC studies, these thermal effects are sometimes referred to as a hot-bath coupling γ_p which will be discussed in Sec. 4.1.2.

3.3.3 Disorder in longer devices

We experiment with more OMC device designs to map the space of available properties and limitations. In particular, we are interested in devices with of different lengths which we tune by altering the amount of defect unit cells. A longer OMC is interesting in several aspects. The longer device has: (1) better optomechanical overlap and thus utilizes the defect unit cell's high coupling more optimally (Sec. 3.1.4), (2) more device material that increases the total thermal capacity of the device, (3) greater thermal contact area to the chip bulk, and (4) a larger optical mode volume that reduces the maximum electric field at fixed n_c, potentially reducing the effect of non-linear optical absorption mechanisms (Sec. 4.1.1). All of the above motivate the choice of device design with $N_d = 31$ presented in Papers A and B.

However, a larger defect region does not only bring positive properties to the OMC. A major challenge with longer devices is apparent when

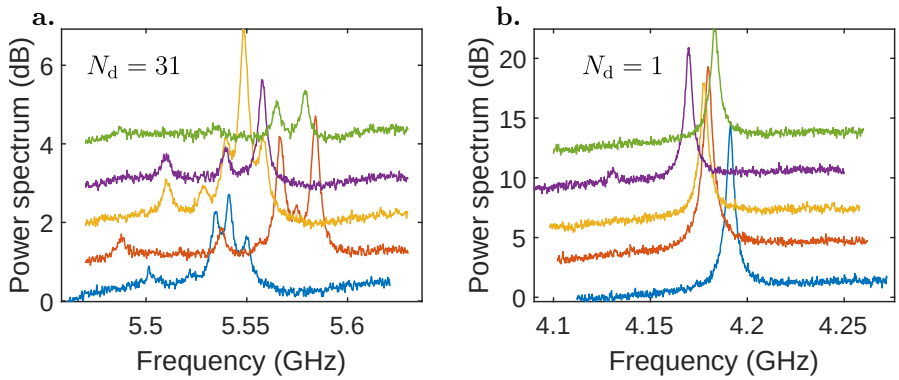


Figure 3.13: Normalized mechanical power spectra for release-free OMCs with different lengths. For each device length, spectra for five devices are presented with a vertical offset for visual clarity. All devices are fabricated on the same chip. **a.** Spectra for long OMCs as presented in Paper A with $N_d = 31$ defect unit cells. **b.** Short OMC spectra where $N_d = 1$.

measuring mechanical power spectra. While a short OMC design with $N_d = 1$ produces devices that with high yield agrees with simulation results, the longer OMC does so with poorer yield. Investigating several devices with $N_d = 1$ and 31 with nominally equal design[6], we see a stark difference in the variation of the mechanical power spectrum for the two device classes (Fig. 3.13). The short design features a single prominent mechanical mode, while the long design produces an unpredictable set of modes around the expected frequency with differing coupling. We believe that this speaks towards the long OMC having a higher susceptibility to fabrication imperfections on account of the larger mechanical mode volume [83].

Despite the low yield, long SOI devices with clean mechanical spectra that agree with simulation is manufacturable with the fabrication techniques presented in Sec. 3.2. However, the results presented in Fig. 3.13 cause designs spanning more than 30 defect unit cells seem less appealing. Even so, the impact of device size is still interesting from a thermometry viewpoint (Sec. 4.3.2), making a solid case for further investigations into larger devices.

[6] up to a small scaling factor.

CHAPTER 4

Laser-induced thermal noise at cryogenic temperatures

The study of laser-induced thermal noise in optomechanical crystals at cryogenic temperatures is both challenging and enticing. Even though many state-of-the-art devices report this type of noise as the limiting factor to performance [50, 25, 116], few have fully committed to understanding its fundamentals. With the release-free optomechanical crystals introduced in the last chapter, we are uniquely positioned to study thermal noise dynamics in silicon nano-structures from a novel perspective that could bring valuable insights to the entire field of low-noise silicon optomechanics.

The majority of the thermometry methods and results are summarized in Paper B, which serves as the centerpiece of this thesis. However, in this chapter, we give further context and details to more fully capture the progress in understanding optically induced thermal noise. The chapter proceeds as follows: we first describe the problem posed by optical-absorption-induced thermal noise and summarize the field's current understanding of the phenomenon. Next, the measurement setup is introduced with further details than those presented in Paper B. Lastly, we present thermometry data taken with additional devices, which add further insight to the Paper B results.

4.1 Laser-induced thermal noise

4.1.1 Optical absorption in silicon

To understand the limitations of low-noise cryogenic silicon optomechanics, it is important to have a foundation in optical absorption. In the context of this work, we will mainly discuss three absorption types: (1) two-photon absorption (TPA), (2) free carrier absorption (FCA), and (3) electronic defect absorption (EDA). The two former types are commonly treated within room-temperature low-loss and high-power silicon photonics [117, 118], whereas EDA is the most commonly stated source for absorption-induced noise in low-power and cryogenic applications [119]. In this section, we briefly discuss the significance of all three types of absorption.

In contrast to three-wave mixing (Sec. 2.4.1), optical absorption refers to a scattering event where the energy of the ingoing photon completely leaves the optical domain. As the telecom photon is a relatively high-energy particle, the available physical degrees of freedom that can reliably accept its energy are limited. All of the previously stated absorption processes thus rely on the electronic degree of freedom, which has available transitions in the single-eV range.

The bandgap energy of silicon ($E_\mathrm{g} = 1.12\,\mathrm{eV}$) exceeds that of the telecom photon ($\sim 0.8\,\mathrm{eV}$), which generally prevents single-photon excitation from the valence band to the conduction band. However, high powers can support TPA, which annihilates two photons to make the transition possible. Being a two-photon process, the TPA rate scales quadratically with power and is thus most prominent at high powers. Apart from absorbing a photon, the result of a TPA-event is an excited electron in the conduction band. These free carriers are subsequently responsible for the next type of absorption: FCA.

Carriers in the conduction band have a continuum of available states for higher energies, making them susceptible to all types of photon absorption. FCA is thus linear in optical power granted that there are available free carriers in the conduction band. However, high resistivity Si wafers are designed for low carrier concentrations and can reach $< 10^{16}\ \mathrm{cm}^{-3}$ at room temperature for resistivities $\sigma > 1\,\Omega\mathrm{cm}$ [118]. In addition, thermally excited carriers are frozen out at low temperatures, making linear FCA irrelevant for the cryogenic discussion. However, TPA-excited carriers can still yield a significant FCA contribution. For a simple Si waveguide, the TPA-excited carrier concentration N_TPA is

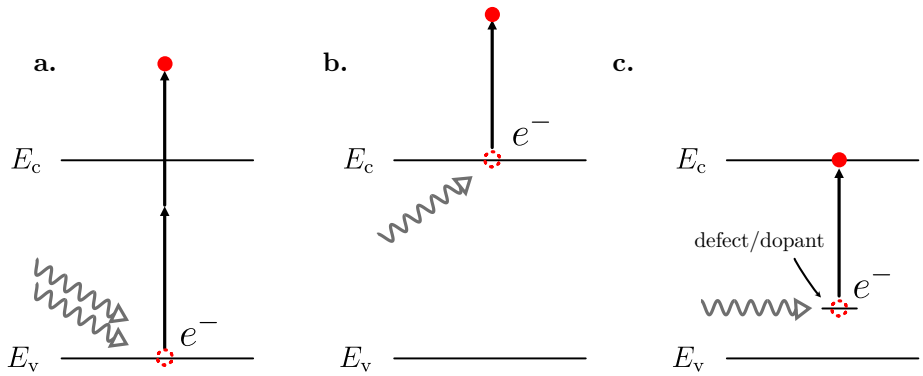


Figure 4.1: Optical absorption in silicon. **a.** A telecom photon at $\hbar\omega_o \approx 0.8\,\text{eV}$ cannot bridge the band gap energy $E_g = E_c - E_v = 1.12\,\text{eV}$; however, at high optical power, two photons can annihilate simultaneously to excite an electron from the valence band to the conduction band in a TPA process. **b.** A free carrier electron already present in the conduction band – put there through thermal excitation or other absorption effects – can absorb single photons. **c.** Dopants or lattice defects can lead to electronically active states in between valence and conduction bands. These localized defect states can bridge the gap for single photons to be absorbed and excite carriers into the conduction band.

given by

$$N_{\text{TPA}} = \frac{\beta I^2 \tau}{2\hbar\omega_o} \tag{4.1}$$

where I is the light intensity, $\beta \approx 0.7\,\text{cm/GW}$ is the two-photon absorption cross-section and τ is the carrier recombination time [117]. At low temperatures, the recombination time can be 100 ps in silicon-on-insulator (SOI) waveguides [120], which would lead to carrier concentrations $N_{\text{TPA}} > 10^{15}\ \text{cm}^{-3}$ in our release-free optomechanical crystal cavity (OMC)s at an input power of 1 mW.

Now, being nonlinear in power, both TPA and TPA-assisted FCA are weak for low optical powers. Therefore, it is the linear absorption mechanisms that dominate in the low-power regime regularly accessed within low-noise quantum optomechanics. This leads us to the final type of optical absorption, which we call EDA in the context of this thesis. EDA is mediated by localized defects that act as intermediary energy levels between the valence and conduction bands (Fig. 4.1c). Even intrinsic, high-resistivity Si has trace amounts of dopants that are frozen out at low temperatures. A dopant such as boron could therefore accept electrons from the valence band in an optical absorption event. However, the

energy mismatch between the telecom photon energy and boron's activation energy (45 meV) likely lowers the probability of this transition. A more probable event is absorption through dangling bond defects present at Si/SiO_2 interfaces [119].

Dangling bond defects, commonly referred to as P_b-type defects, have been extensively studied in the context of semiconductor CMOS-technology [121]. The defects are formed in the transition where the (near) perfect Si crystal structure transitions into unordered thermal/native SiO_2. Dangling bonds can act as traps for both electrons and holes with energy levels between valence and conduction bands, reducing carrier mobility and causing unwanted leakage currents [121]. It has been shown that P_b-type defects can have both donor-like and acceptor-like defect states in the Si bandgap, which closely matches the telecom radiation energy [122]. Although no study has yet analyzed the density of these defects at low temperatures, it is still a strong hypothesis that P_b-type defects are a major cause of linear absorption in the context of quantum silicon optomechanics.

A common way to deal with P_b-type defects is through hydrogen passivation. A hydrogen atom can occupy a dangling bond, thereby extinguishing its electronic activity. Surface passivation of Si through HF-etching has been shown to significantly reduce absorption in Si whispering gallery mode (WGM) resonators [16]. While HF-etching is an effective Si surface treatment, its reach is limited and cannot affect the Si/thermal SiO_2-interface attaching the SOI release-free OMCs to their substrate. On the other hand, forming gas annealing (FGA) is known to diffuse hydrogen into thin-film Si and can thus lead to deeper passivation in release-free OMCs [123].

4.1.2 Hot-bath model

The absorption events discussed in the last subsection transform energy in the electromagnetic field into charge carrier kinetic energy. But how does this process lead to a higher thermal occupation in the OMC mechanical mode at $\sim 5\,\mathrm{GHz}$? Even though a microscopic description for the origin of optical absorption induced noise is not yet fully understood by the international community, theoretical models on its treatment have been presented and compared to measurement results [119, 49, 100]. A general consensus on a proper noise model has not yet been reached among research groups studying cryogenic silicon optomechanics, making measurement results across studies harder to compare. In an effort to

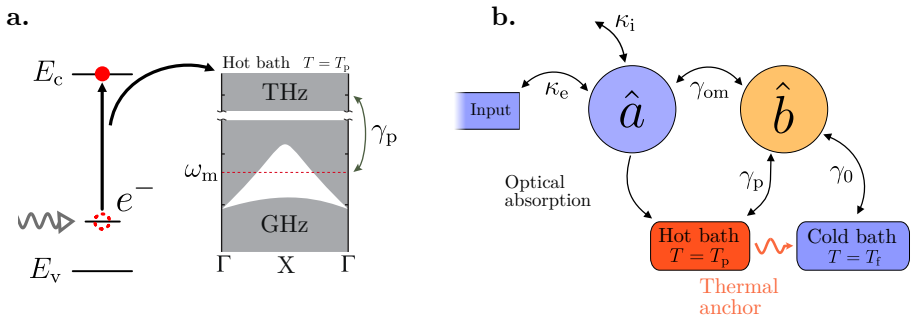


Figure 4.2: Hot-bath model for optical absorption heating. **a.** Energy is transferred from optical to acoustic domains through phonon-mediated electronic defect absorption/relaxation. The energy populates a band of high-frequency (THz) phonons with fast internal scattering. The THz-phonons are thus defined as a hot bath with temperature T_p. Finally three-wave mixing at rate γ_p populates the mechanical mode at ω_m. **b.** Full interaction environment for the mechanical mode $\hat{b}$. The optical mode $\hat{a}$ couples to $\hat{b}$ through γ_{om} and is in turn coupled to the input waveguide and its thermal environment at rates κ_e and κ_i, respectively. Optical absorption populates the hot bath which interacts with $\hat{b}$ with rate γ_p. Finally, $\hat{b}$ couples to the cryostat cold bath through γ_0.

bolster comparability, we thus choose to base the analysis in this thesis on the most generally cited model presented by Meenehan *et al.* in 2014 [119] – even though its general applicability is still under investigation.

The model is based partly on the assumption that EDA (and the reverse relaxation process) is phonon-mediated. This is a reasonable assumption since the local electric field around a silicon dangling bond depends on the presence of electric charge. As an electron trapped at the dangling bond is ionized by an optical photon, equilibrium positions of neighboring atoms are likely perturbed, leading to acoustic excitations upon lattice relaxation. The EDA events thus inject a shower of phonons into the OMC, assumed to be of high frequency due to the energy scale of the absorbed photon. The injected phonons then inter-mix on a time scale that allows them to form a thermal bath with a common temperature T_p [100] (Fig. 4.2). This thermal bath of THz phonons is labeled the "hot bath" and is the noise source populating the mechanical mode with excess acoustic energy in a cryogenic environment. We note that to what extent T_p is well-defined depends on internal scattering and relaxation for the THz phonons and might not be equal for all device geometries. This adds to the qualitative nature of the model, making experiments important for proper verification.

Table 4.1: Table of n_c exponents. Exponents are here defined through $n_m \propto (n_c)^\alpha$ and $\gamma_p \propto (n_c)^\beta$. In most low-loss device $n_m = n_p$. Some exponents are presented in regimes of low/high n_c. BC: Butt-coupled, SC: Side-coupled, RF: Release-free. Blanks are left where data is not provided/no simple power law was identified.

Device type	Reference	Year	α	β
1D	Meenehan *et al.* [119]	2014	0.25	–
1D	MacCabe *et al.* [100]	2020	0.33	0.66
BC 2D	Ren *et al.* [49]	2020	0.33	0.61/0.29
SC 2D-I	Sonar *et al.* [78]	2025	0.31	0.29
SC 2D-II	Sonar *et al.* [78]	2025	0.21	0.29/0.39
RF 1D	Kolvik *et al.* [125]	2025	0.44/0.61	0.98
1D	Kolvik *et al.* [125]	2025	0.29	–
High γ_0 1D	Fig. 4.12b	2026	0.72/0.33	–
1UC SOS	Fig. 4.10	2026	0.81	–
31UC SOS	Fig. 4.10	2026	0.63	–

Due to the vast frequency gap between the hot bath's THz-phonons and the GHz mechanical mode, coupling between them is mediated by three-wave phonon-phonon scattering. The interaction is conjectured to be facilitated by the anharmonicity in the atomic lattice, which also governs Landau–Rumer and Akheizer damping [124]. Through Fermi's Golden Rule, a non-linear interaction rate γ_p can be defined, which describes the mechanical mode's interaction with the hot bath at an effective occupation $n_p = (\exp\{\hbar\omega_m/(k_B T_p)\} - 1)^{-1}$ [119]. Absorption-induced heating is thus phenomenologically described by a local thermal bath with a temperature T_p and thermal population n_p, which interacts with the mechanical mode with rate γ_p.

With the hot bath defined, the analysis can be extended to describe how the hot-bath parameters depend on input optical power. Using a polynomial ansatz for the hot-bath density of states and assuming that the hot bath radiates energy like a black body leads to [100]

$$\begin{cases} \gamma_p \propto n_c^{2(d-1)/(d+1)} \\ n_p \propto n_c^{1/(d+1)} \end{cases} \quad \text{for } T_p \gg \frac{\hbar\omega_m}{k_B}, \qquad \begin{cases} \gamma_p \propto n_c^{(2d-1)/(d+1)} \\ n_p \propto \exp\left[-\hbar\omega_m / \left(k_B n_c^{1/(d+1)}\right)\right] \end{cases} \quad \text{for } T_p \ll \frac{\hbar\omega_m}{k_B}. \tag{4.2}$$

In (4.2), d is a parameter representing the spatial dimensionality of the

hot bath, which would differ based on device geometry. The model thus predicts an n_c power-law dependence for both the effective population n_p and the interaction rate γ_p for high T_p. While the bath dimensionality argument has shown some agreement with early measurement results for 1D suspended OMCs (in which a hot bath dimensionality $d = 2$ was assumed due to the estimated frequencies of the hot bath phonons), the model has not held up consistently across continued studies on different device types. Tab. 4.1 compiles power-law exponents reported in the literature, including results from the release-free device presented in Paper B and Figs. 4.10,4.12. Notably, the effects behind these power-law dependencies do not appear to be tied to physical dimensionality alone, since devices with the same geometry sometimes yield different results. Disorder and surface effects are plausible explanations for these differences [78], but no study has yet examined this systematically. What is clear is that further exploration of the microscopic effects underlying optical absorption and heat conductance is needed to close these knowledge gaps.

It should also be noted that the data in Tab. 4.1 is mostly compiled from work published by Oskar Painter's group at Caltech. It goes without saying that there are other contributors to the field of cryogenic silicon optomechanics; however, as previously stated, the formalism used across works is not always consistent enough to allow for direct comparison. We adopt the hot-bath model in this thesis since it considers both absolute noise levels n_p and thermal broadening γ_p, giving more tools for analyzing measurement results.

4.1.3 Phonon transport at millikelvin temperatures

Ridding nanoscale devices of heat is a major concern across many technologies [126, 127]. Phonons are one of the primary heat carriers and are especially important in materials with low charge-carrier concentration such as insulators and high-resistivity silicon. Using phonon transport through the chip substrate as a channel to funnel away laser-induced thermal noise is the primary technological advantage claimed by the release-free optomechanical crystal. However, the intricacies of nanoscale phonon transport make direct predictions of increased device heat capacity challenging. As device sizes are reduced, the simple Fourier's law suffers in predictability due to material interfaces and the phonon mean-free-path (MFP) exceeding the device scale [127]. Proper descriptions of thermal heat transport in nanoscale devices thus require other mod-

els, and recent progress has been made with descriptions involving, e.g., hydrodynamic phonon transport [128]. However, limited work has yet been extended into the cryogenic environment relevant for the quantum silicon optomechanics experiments in this thesis.

At the 10 mK environment at which this thesis' cryogenic experiments are performed, the thermal properties of materials are vastly different from room temperature. Material thermal conductance and capacity scale drastically with temperature, imparting a strong and non-trivial temperature nonlinearity to thermal noise studies. We will here summarize the important thermal properties of the materials relevant for our release-free OMCs.

Heat transfer through phonons relies on the flow of thermally excited phonons through the atomic lattice of materials. At low temperatures, phonon-mediated heat conduction κ_{th} in a crystalline material can be expressed as [129]

$$\kappa_{\mathrm{th}} = \frac{1}{3}\frac{C_{\mathrm{th}}}{V} v_{\mathrm{g}} \Lambda_{\mathrm{MFP}}. \tag{4.3}$$

The heat conduction is thus governed by (1) the amount and density of excited thermal states, represented by the thermal capacity C_{th} in the volume V, (2) the phonon group velocity v_{g}, and (3) the amount of transport obstructions represented by the phonon MFP Λ_{MFP}. The two major temperature-dependent parts of (4.3) are the heat capacity and the MFP.

For a crystalline material, the heat capacity can be calculated using the Debye model which gives a strong T^3-dependence for low temperatures. The phonon MFP is more technical and involves several contributions from different sources acting as obstructions to phonon transport. At low temperatures, both phonon-phonon (Umklapp) and electron-phonon scattering can safely be neglected, leaving material defects and boundaries as the major contributors to the MFP. All materials have imperfections such as dislocations and point-defects which scatter phonons. These scattering events are dependent on phonon wavelength and frequency and thus impart an inverse temperature dependence to the MFP [129]. However, high-purity materials at low temperatures can show low contributions from defects, leaving $\Lambda_{\mathrm{MFP}} \propto T^0 \Rightarrow \kappa_{\mathrm{th}} \propto T^3$.

For amorphous materials, heat conductance and specific heat are instead commonly described in terms of resonant phonon interactions with two-level systems (TLS) [133]. The model describes the amorphous material's atoms as sitting in metastable potentials which can resonantly interact with phonons passing through the lattice. The TLS energy

Table 4.2: Summary of experimentally measured thermal conductivities κ_{th} given in $\mathrm{W}/(\mathrm{m}\cdot\mathrm{K})$ for materials relevant to this thesis work. Values for 10 mK are extrapolations using the given power-law behavior at 300 mK. LR: Low resistivity, HR: High resistivity.

Material	Reference	$\kappa_{\mathrm{th}}(300\,\mathrm{mK})$	Scaling	$\kappa_{\mathrm{th}}(10\,\mathrm{mK})$
LR Si	[130]	$8 \cdot 10^{-4}$	$T^{2.2}$	$4 \cdot 10^{-7}$
a-SiO_2	[131]	$2 \cdot 10^{-4}$	T^{2}	$2 \cdot 10^{-7}$
Sapphire (chip-scale)	[130]	$2 \cdot 10^{-3}$	T^{3}	$7 \cdot 10^{-8}$
HR Si	[130]	$5 \cdot 10^{-2}$	$T^{2.4}$	$1 \cdot 10^{-5}$
Sapphire (bulk)	[132]	$1 \cdot 10^{-1}$	T^{3}	$3 \cdot 10^{-6}$

separation ΔE is assumed to be statistically distributed with a near flat dependence on ΔE in relevant energy ranges which leads to a $\kappa_{\mathrm{th}} \propto T^2$ for $T < 1\,\mathrm{K}$.

The most important materials to this thesis are Si, SiO_2, and sapphire. In Tab. 4.2, we present experimental thermal conductivity data in the sub-kelvin range for these materials. Recent thermal conductivity results show data with decent consistency with the above models. The literature confirms that the crystalline materials are superior heat transporters compared to amorphous SiO_2 even at low temperatures, despite the more favorable T^2-scaling. It also shows that the sample size may have a big impact on thermal conductivity as chip-scale sapphire is shown to perform worse by almost two orders of magnitude compared to bulk samples. silicon doping also seems to have an impact, as high-resistivity silicon surpasses low-resistivity silicon by more than two orders of magnitude.

Lastly, we address the important notion of material interfaces in our release-free OMCs. Increased thermal conduction away from the optomechanically active region relies on efficient phonon transport across the interface that attaches the OMC to the substrate. A material interface constitutes a discontinuity in the impedance experienced by traveling phonons making the transition from one material to another. Phonon scattering due to this impedance mismatch can thus be modeled as an interfacial thermal resistance (ITR) sometimes called Kapitza resistance [134] and is non-zero even if the material bonding conditions are perfect. The ITR can be even more significant for imperfect material bonding where the interface extends into the material bulk in a highly disordered and defect-ridden region. The interface quality between the device layer and the chip bulk is thus of significant importance, especially in less con-

ventional material stacks such as silicon-on-sapphire (SOS). The impact of ITR in the SOI-platform is evaluated implicitly in the thermometry experiments presented in Paper B.

4.1.4 Thermal phonon dynamics

In the hot-bath model introduced in Sec. 4.1.2, we assume a thermal bath coupled to the mechanical mode which, during continuous wave (CW) optical pumping, is at an elevated thermal occupancy n_p compared to the surrounding environment at ambient temperature T_f (Fig. 4.2b). Using the cavity optomechanical coupled mode equations (CME) (Eqs. (2.21)), we can solve for the expected steady-state phonon occupation for a sideband-resolved oscillator in the $C_\mathrm{om} < 1$ regime:

$$n_\mathrm{m} = \langle \hat{b}^\dagger \hat{b} \rangle = \frac{n_0\gamma_0 + n_\mathrm{p}\gamma_\mathrm{p}}{\gamma_\mathrm{m}}. \tag{4.4}$$

where $\gamma_\mathrm{m} = \gamma_0 + \gamma_\mathrm{p} \pm \gamma_\mathrm{om}$ for red (+) and blue (−) detuning and $\gamma_\mathrm{m} = \gamma_0 + \gamma_\mathrm{p}$ when $\Delta = 0$. For any relevant CW application in the quantum regime, we require that the steady-state occupation is $n_\mathrm{m} \ll 1$. Another metric for this regime is the quantum cooperativity $C_\mathrm{q} = C_\mathrm{om}/n_\mathrm{m}$ which must be > 1 to achieve achieve optomechanical state transfer faster than the mechanical decoherence rate [17]. Although some optomechanical systems have shown $C_\mathrm{q} > 1$ [49, 78], reliable quantum operation requires further reduction of noise which, in this model, is represented by reducing $n_\mathrm{p}\gamma_\mathrm{p}$.

However, an intriguing proposal to overcome the steady-state noise and access more near-term quantum applications was proposed in 2015 by Meenehan *et al.* [135]. Their proposal was to operate the devices in a pulsed regime where very short optical pulses would perform optomechanical action faster than thermal noise could build up in the OMC. It is therefore not sufficient to know the steady-state noise level of the OMC, but also to know the noise's time dynamics.

To derive the time dynamics of the thermal noise under optical pulsing, we again return to the cavity optomechanical CMEs (Eqs. (2.21)). This time, however, we solve them in the time domain while adiabatically eliminating the dynamics of the optical cavity (see App.B.5). For a sharp optical pulse starting at $t = 0$ – which for now is assumed to immediately populate the hot bath – we get the following dynamics for

the time-dependent noise occupancy $n_{\mathrm{m}}(t) = \langle \hat{b}^\dagger(t)\hat{b}(t)\rangle$:

$$\begin{aligned} n_{\mathrm{m}}(t) &= n_{\mathrm{i}} + (n_{\mathrm{f}} - n_{\mathrm{i}})(1 - e^{-\gamma_{\mathrm{m}} t}), \quad \forall t > 0, \\ n_{\mathrm{i}} &= \langle \hat{b}^\dagger(0)\hat{b}(0)\rangle, \quad n_{\mathrm{f}} = \frac{\gamma_0 n_0 + \gamma_{\mathrm{p}} n_{\mathrm{p}}}{\gamma_{\mathrm{m}}}, \end{aligned} \tag{4.5}$$

with γ_{om} as in (4.4). Again, this assumes that the optomechanical backaction is not strong enough to cause significant backaction noise.

During pulsed operation in experiments probing the quantum properties of the system, thermal noise dilutes and decoheres the prepared quantum state. For instance, in work such as Ref. [24], single photons are generated from an optomechanical system by interleaving blue and red detuned optical pulses. The spontaneous parametric down-converted (SPDC) photon in the photon-phonon pair generated by the blue write-pulse is used to herald a single phonon state in the mechanical mode. However, infidelity enters the experiment when the photon-click used for heralding does not originate from the SPDC event. Upconverted thermal phonons are one of the possible sources of this infidelity. While assuming a sharp optical pulse ($\gamma_{\mathrm{om}}(t) \propto n_{\mathrm{c}}(t) = \mathrm{const}$), the probability p_{th} that a thermal phonon is upconverted during a pulse of length T_{p} can be expressed as:

$$p_{\mathrm{th}} = \gamma_{\mathrm{om}} \int_0^{T_{\mathrm{p}}} n_{\mathrm{m}}(t)\mathrm{d}t \coloneqq p_{\mathrm{s}} n_{\mathrm{avg}} \tag{4.6}$$

where $p_{\mathrm{s}} = \gamma_{\mathrm{om}} T_{\mathrm{p}}$ is the Stokes scattering probability and $n_{\mathrm{avg}} = T_{\mathrm{p}}^{-1} \int_0^{T_{\mathrm{p}}} n_{\mathrm{m}}(t)\mathrm{d}t$ is the average phonon occupation during the pulse. For quantum operations with fidelity unbounded by thermal noise, we thus require $p_{\mathrm{s}} \gg p_{\mathrm{th}} \Leftrightarrow n_{\mathrm{avg}} \ll 1$. Now, for short pulses, (4.5) gives

$$n_{\mathrm{avg}} \approx n_{\mathrm{i}} + n_{\mathrm{f}} \frac{T_{\mathrm{p}} \gamma_{\mathrm{m}}}{2}, \quad \text{for } T_{\mathrm{p}} \gamma_{\mathrm{m}} \ll 1, \tag{4.7}$$

which serves as a lower bound to n_{avg} *if* $n_{\mathrm{m}}(t)$ follows (4.5).

Phonon dynamics given by Eq. (4.5) is valid under the assumption that heating caused through optical absorption is applied immediately upon optical excitation. This assumes that the processes that induce noise are much faster than the dynamics of the mechanical mode, which is supported within the THz phonon hot bath model presented in Sec. 4.1.2. Throughout the experiments performed in this thesis, limited evidence has pointed against this assumption. More specifically, the dynamics stated in (4.5) has consistently been used to accurately represent the

time dependence of n_m upon optical pulsing. However, previous work has also reported deviations from this standard dynamics. In Ref. [135], this behavior was quantified with a fractional parameter δ_b and an additional rate γ_s with which the dynamics of n_m were described:

$$\dot{n}_\mathrm{m}(t) = -\gamma_\mathrm{m} n_\mathrm{m}(t) + \gamma_0 n_0 + \gamma_\mathrm{p} n_\mathrm{p}(1 - \delta_\mathrm{b} e^{-\gamma_\mathrm{s} t}). \tag{4.8}$$

More detailed phenomenological models were also presented in [100]. Like several other properties of optical-induced thermal noise, the origin of this behavior is not yet fully understood.

4.1.5 The thermo-optic effect

Thermal noise in the OMC impacts several physical properties of the OMC; one of these affected properties is the optical resonance frequency ω_o through the thermo-optic effect. The thermo-optic effect is an optical dispersive nonlinearity present in most materials including silicon which alters the material's refractive index as a function of temperature $n_\mathrm{Si} = n_\mathrm{Si}(T)$. It is common to linearize this dependence around a reference temperature T_ref to get

$$n_\mathrm{Si}(T) = n_\mathrm{Si}(T_\mathrm{ref}) + \beta(T_\mathrm{ref})(T - T_\mathrm{ref}), \tag{4.9}$$

where $\beta(T_\mathrm{ref}) = (\partial n_\mathrm{Si}/\partial T)(T_\mathrm{ref})$ is the thermo-optic coefficient. This is a commonly exploited property of materials and can be used both for temperature sensing [136] and fine-tuning of phase conditions [137]. In this work, we use this property to study optical-absorption-induced heating. However, the heavy temperature dependence of β for low temperatures [138] along with the presence of additional dispersive nonlinearities in silicon [118] makes this feature more of a proxy rather than a quantitative measurement tool of laser-induced heating.

4.2 Measurement setup

Performing cryogenic thermometry of nanoscale optomechanical devices requires specialized measurement capabilities. Measuring the weak thermomechanical sidebands at cryogenic temperatures warrants high sensitivity with low added noise. Details of the full cryogenic experimental setup are provided in Paper B Appendix B. However, some aspects were left out for brevity and will thus be the subject of this section.

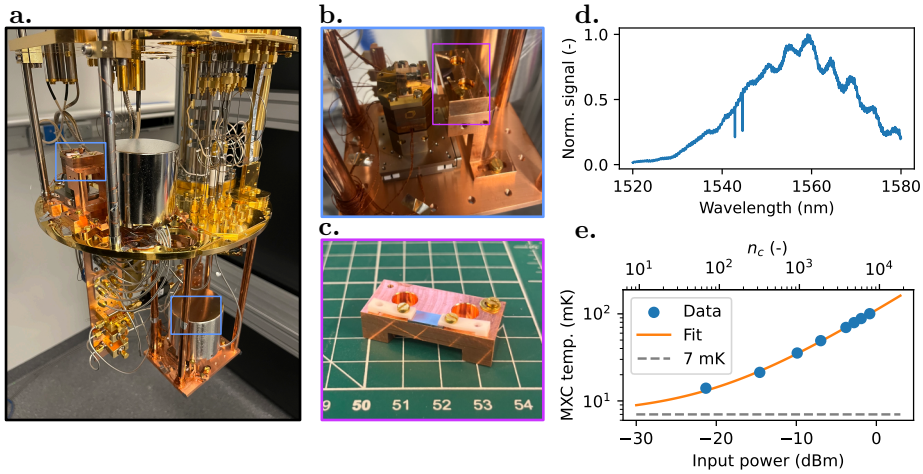


Figure 4.3: Cryogenic optomechanics setup. **a.** Mixing chamber of a Bluefors LD400 cryostat featuring two optomechanics compatible setups (blue). **b.** Each optomechanics setup contains a set of cryogenic positioners used to align an angle-cut fiber to grating couplers on the chip (magenta). **c.** Chip on copper mounting block, secured with PTFE clamps. **d.** Typical normalized grating response. **e.** Mixing chamber (MXC) temperature as function of input optical power. We also show achieved n_c for fiber-chip coupling $\eta_{fc} = -6\,\mathrm{dB}$, $\kappa/(2\pi) = 1.5\,\mathrm{GHz}$, $\kappa_e/(2\pi) = 750\,\mathrm{MHz}$, $\Delta/(2\pi) = 5\,\mathrm{GHz}$.

4.2.1 Dilution refrigerator setup

To reach the temperatures required for these studies, we use a Bluefors LD400 dilution refrigerator. The cryostat is specially equipped with optical fiber feed-throughs which allow fiber access to the mixing chamber (MXC) where the coldest temperatures are reached. For our experiments requiring optical alignment, we use one of two setups equipped with cryogenically compatible positioning stages (attocube) mounted to the MXC (Fig. 4.3a). At room temperature, we use the positioners along with a USB microscope to align angle-cut fibers to the on-chip grating couplers. Thermal contraction during cooldown causes misalignment which we counteract with periodic realignment every 30 min by measuring light reflected off the devices. When the cryostat reaches 4 K, we finalize alignment to the device to be tested at millikelvin temperatures before condensation causes temperatures to drop further.

Optimal fiber-chip coupling at the wavelength of the device under test (DUT) for a given grating coupler is achieved by optimizing the grating maximum transmission wavelength λ_{max} according to the phase-

matching condition [107]

$$\lambda_{\mathrm{max}} = \Lambda(n_{\mathrm{eff}} - \sin(\theta_{\mathrm{in}})), \tag{4.10}$$

where Λ and n_{eff} are the grating period and effective index, and θ_{in} is the light incidence angle. We choose Λ and n_{eff} to align λ_{max} to the resonance wavelength of the DUT, with θ_{in} fixed by the properties and tilt of the input fiber. However, a slight variation to the final fiber conditions after installation leads to uncertainty in λ_{max} and thus also in the achievable fiber-chip coupling efficiencies (Fig. 4.3d). Common fiber-chip coupling efficiencies achieved cryogenically range from -6 to $-10\,\mathrm{dB}$. The uncertainty would be reduced by installing a cryogenically compatible goniometer for the fiber mount.

After condensation, we reach temperatures at the MXC of around 10 mK in the span of 2 hours, dropping further to $\sim$ 7 mK over the course of a few days. Due to the µW-level cooling power at the MXC, the thermal conditions at the MXC are easily perturbed when applying optical power. We track the steady-state temperature of the MXC as a function of applied optical power (Fig. 4.3e) and find a phenomenological model

$$T_0(P) = A[P/(1\,\mathrm{mW})]^{\alpha} + 7\ \mathrm{mK} \quad \text{for } T_0 \in \{10, 100\}\ \mathrm{mK}, \tag{4.11}$$

where P is input power in W, $A = 104\,\mathrm{mK}$ and $\alpha = 0.5767$. Throughout thermometry experiments performed in this thesis, input optical power never exceeds 0 dBm, thereby keeping steady-state $T_0 \lesssim 110\,\mathrm{mK}$ which is equivalent to $n_0 \lesssim 0.12$ at 5 GHz. We note that this temperature is measured directly on the MXC plate close to the cryostat cooling element and does not accurately represent the temperature of the chip. This is of importance when interpreting thermometry results which we will return to in Sec. 4.3.4.

4.2.2 Phase noise and pump filtering

A crucial part of the optical experimental setup is the phase noise and pump filtering which enable detection of weak optomechanical sidebands with signals unperturbed by phase noise and pump light. As discussed briefly in Sec. 2.4.4, pumping an optomechanical system with a noisy laser can cause significant perturbation to a thermometry measurement. To make sure that the measurement is not plagued by excess heating or noise squashing/anti-squashing, proper pre-filtering is required.

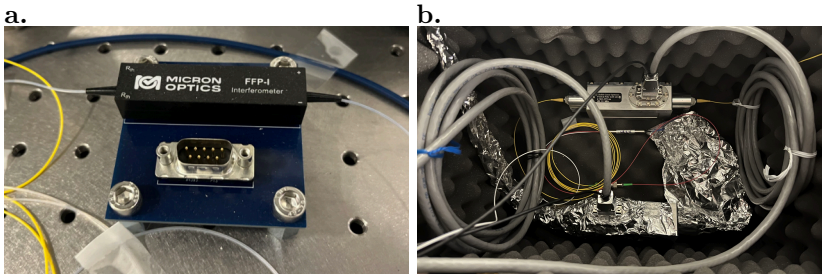


Figure 4.4: a. Fiber coupled Fabry–Pérot filter with temperature controlled frequency tunability. Used for reducing laser phase noise at the mechanical offset frequency. **b.** Two fiber-coupled piezo-tunable Fabry–Pérot filters inside an acoustically and thermally insulated enclosure. When tuned to an optomechanical sideband the filters effectively removes the pump before detection. Aluminum foils covers fibers between the last filter and the single-photon detector input to shield it from stray light.

We perform pre-filtering by locking our free-running laser (Toptica CTL1550) to a fiber-coupled Fabry–Pérot filter (Luna FFP-I) with full-width-half-maximum (FWHM) bandwidth of 36 MHz and FSR ≈ 20 GHz (Fig. 4.4a). The Fabry–Pérot power transfer function is given by [139]

$$T(\omega) = \frac{(1-r)^2}{1 + r^2 - 2r\cos(\omega t_{\mathrm{rt}})}, \tag{4.12}$$

where $r \approx 1 - \pi\mathrm{FWHM}/\mathrm{FSR}$[1] is the mirror reflectivity, and t_{rt} is the cavity round-trip time. For the given parameters, (4.12) projects a noise suppression around 48 dB at an offset frequency of 5 GHz. To have total control of the pump laser frequency, the filter is tunable over more than one free spectral range (FSR) using a thermo-electric cooler element that is regulated by a temperature controller. This allows for accurate placement of the laser at a desired detuning Δ and keeps it fixed with minimal drift which is crucial for the second filter type in the setup: pump filtering.

The purpose of pump filtering is to remove the pump tone so that the optomechanical sideband is the only signal passed to detection. This is crucial in a superconducting nanowire single-photon detector (SNSPD) measurement since the detector is generally not frequency resolving and cannot distinguish signal from pump photons. As mentioned in Sec. 2.4.1, the power in an optomechanical sideband is around −50 dBc when as-

[1] Valid for high finesse cavities where the finesse $\mathcal{F} = \mathrm{FSR}/\mathrm{FWHM}$.

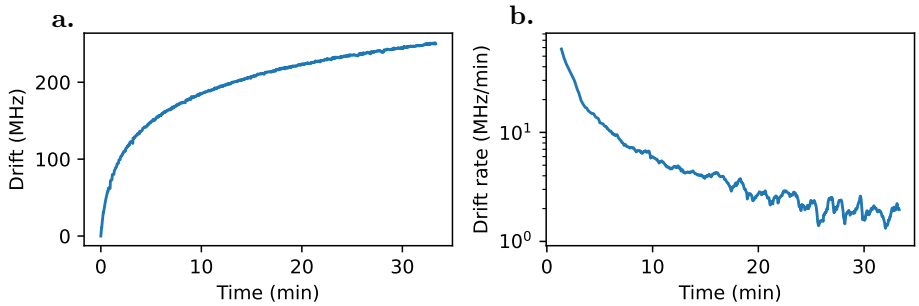


Figure 4.5: **a.** Typical pump filter drift due to piezo creep immediately following initial alignment. **b.** Drift rate due to piezo creep. Settles in the a range $< 1\,\mathrm{MHz/min}$ over the course of a few hours.

suming reasonable optomechanical performance in a room temperature setting where $n_\mathrm{m} \sim 1200$. In cryogenic environments, however, we hope to measure $n_\mathrm{m} \lesssim 1$, meaning that expected sideband powers are in the $-80\,\mathrm{dBc}$ range or lower. To make sure that the SNSPD signal is not drowned by noise, we thus need to achieve $> 80\,\mathrm{dB}$ suppression of the pump tone before detection.

We achieve pump filtering with two additional tunable Fabry–Pérot filters that we apply in series to the light before detection. These filters have FWHM bandwidth of 13 MHz and FSR $\approx 19\,\mathrm{GHz}$ which through (4.12) gives a total pump suppression around 113 dB at 5 GHz (Fig. 4.4b). Due to the exceptionally weak signals and frequency-insensitive nature of the SNSPD detection, active locking of the pump filters to the optomechanical sideband is unavailable. We thus use passive placement of the filters around the optomechanical sideband while resorting to periodic, automatic realignment during longer measurements. To align the filters before or during a measurement, we generate a strong sideband at the mechanical frequency using an electro-optic modulator (EOM) and use that as a reference for filter alignment using piezo tunability. After initial filter placement, piezo creep is a major factor of filter drift (Fig. 4.5). However, when piezo creep tapers off after around 30 minutes, the total drift rate settles around 1 MHz/min. For long experiments on the time scale of days, average drift rates can settle at significantly lower values, allowing for measurement periods of minutes before automatic realignment.

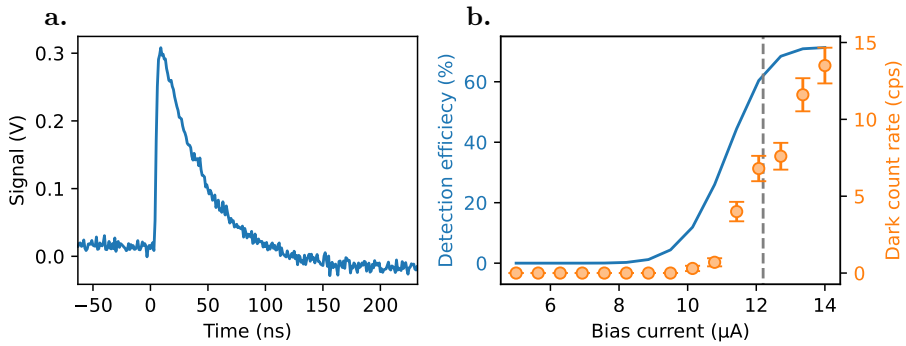


Figure 4.6: SNSPD characterization. **a.** Voltage signal upon a photon detection event. **b.** Detection efficiency and dark count noise as a function of detector bias current. Gray dashed line indicates standard operating current 12.2 μA. Note that detection efficiency also includes potential losses in connector and cryostat feed-through fibers.

4.2.3 Single-photon detection and excess noise

To measure the weak optomechanical sidebands, we use SNSPDs mounted to the 900 mK stage of the dilution refrigerator cryostat. The working principle behind the SNSPD is that photon absorption events in a superconducting wire locally break superconductivity and temporarily increase the resistance in the wire [140]. The resulting spike in voltage across the wire is fed to an amplifier before being detected in a photon-counting module which reads each spike as a photon detection event (Fig. 4.6a). We use WSi nanowire detectors (PhotonSpot) which are spliced to fibers attached to the cryostat optical feed-throughs. At optimal bias current, we achieve detection efficiencies $\sim 70\,\%$[2] and dark count rate ~ 6 cps (Fig. 4.6b) for a terminated detector input. This corresponds to an equivalent noise power of -151 dBm.

Apart from dark count noise, there are several other noise factors that must be suppressed for high sensitivity measurements. We suppress ambient stray light from transmitting into the fibers leading to the SNSPDs by running experiments with minimum ambient light and by wrapping all fibers connecting the last pump filter to the SNSPDs with aluminum foil. In addition, we reduce broadband laser noise before detection by using a 1530-1570 nm bandpass filter (OF-Link) with 30 dB isolation.

Finally, we characterize the main sources of laser noise: phase/intensity

[2]Including temperature-dependent loss in cryostat feed-through and fiber.

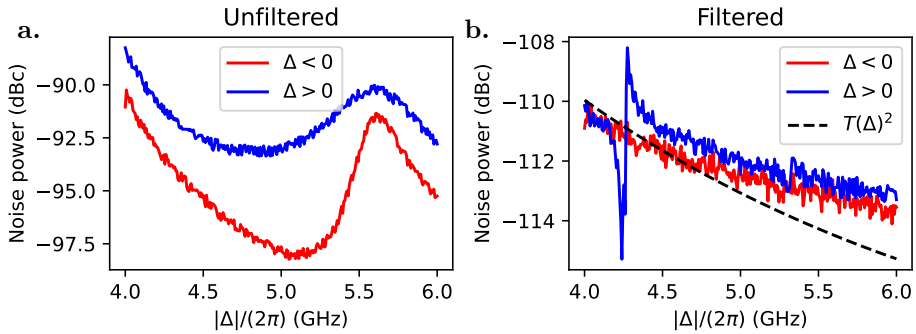


Figure 4.7: Laser noise as measured with single-photon detection (SPD) through the pump filter stack with effective FWHM $\approx 8.86\,\mathrm{MHz}$. Noise is measured at offset Δ from the main laser output at $\lambda = 1552\,\mathrm{nm}$. **a.** Free-running laser noise. **b.** Noise while the laser is locked to an Fabry–Pérot (FP)-filter with 50 MHz BW and 18 GHz FSR. The spectral features of the unfiltered noise are replaced by the transmission function of the pump filter stack which points towards pump bleed-through as the limiting noise factor. A resonance feature representing an auxiliary filter mode can be seen for $\Delta/(2\pi) \approx 4.25\,\mathrm{GHz}$. Dashed line represents $T(\Delta)$ given in (4.12).

noise at the offset frequency and pump filter bleed-through. The measurements are performed by sending the main laser directly to the pump filter stack which is placed at a variable offset frequency Δ. The signal power measured on the SNSPD is referred to the input light to calculate the pump-referred relative noise power in the 8.86 MHz effective bandwidth of the pump filter stack (Fig. 4.7). We perform the experiment at the standard 50 mW laser output power, both red and blue detuned with offset $|\Delta| \in \{4, 6\}$ GHz for both a free-running laser and while locked to the phase-noise-suppressing filter (Sec. 4.2.2). In the free-running experiment, we measure noise powers in the range of $\{-90, -100\}$ dBc with a clear peak at 5.6 GHz. This represents noise power spectral densities (PSD) $\bar{S}_{\phi\phi}(\Delta) \in \{-160, -170\}$ dBc/Hz which seems to be within an order of magnitude of what was measured in 2013 for certain New Focus lasers (Ref. [79])[3]. Interestingly, the noise does not seem completely symmetrical for red and blue sides which could allude to correlations in phase and amplitude noise caused by relaxation oscillations.

While locked to the pump filters, the noise drops significantly – but not by the 48 dB projected by (4.12). The measurement is now instead limited by pump light seeping through the pump filter stack which we call

[3]To compare to frequency noise PSD $\bar{S}_{\omega\omega}(\omega)$, we use $\bar{S}_{\omega\omega}(\omega) = \omega^2 \bar{S}_{\phi\phi}(\omega)$.

pump bleed-through. We measure bleed-through in the range expected through (4.12) meaning that we achieve pump suppression in the range of 110 dB.

4.2.4 Acousto-optic pulsing

To study the time dynamics of the OMC thermal noise, we use a set of two 110 MHz acousto-optic modulators (AOM)s with a total extinction ratio > 110 dB. The AOM radio-frequency (RF) drivers are controlled with analog pulses sent from the pulse sequencer module (QM OPX) that also reads the SNSPD output and records photon clicks.

To characterize the optical pulsing, we send the AOM output through heavy attenuation before detection with the SNSPD. A typical pulse shape is presented in Fig. 4.8. We fit this to a phenomenological model:

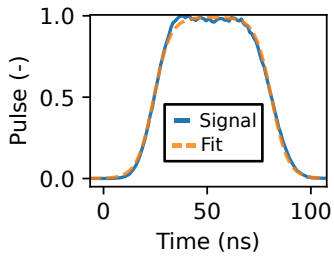


Figure 4.8: Normalized waveform of a 57 ns pulse generated through acousto-optic modulation with fit to (4.13).

$$P(t) = P_{\max}\sigma(t - t_{\text{start}})\sigma(-(t - t_{\text{stop}})), \tag{4.13}$$

for start and stop times t_{start} and t_{stop}, where $\sigma(t) = (1 - e^{t/t_{\text{r}}})^{-1}$ is a sigmoid function with rise time parameter $t_{\text{r}} \approx 4$ ns. We calibrate the pulsing by comparing programmed pulse lengths to the fitted measurements and find a 10-90% rise time of 16 ns. The calibrated pulse waveform (4.13) is used to fit $n_{\text{m}}(t)$ in Paper B.

4.3 Supplementary thermometry results

In Paper B, we make a comprehensive comparison between a release-free SOI OMC with 31 defect unit cells and a conventional suspended breathing mode OMC with high mechanical Q. More devices have been cryogenically studied during the course of this thesis which have not yet been published. In this section, we present results obtained with these additional devices which further our understanding of the behavior of optically induced thermal noise in silicon OMCs.

Table 4.3: Optomechanical properties of studied SOS devices.

Device:	SOSA 31 UC	SOSB 1 UC A
$\omega_o/(2\pi)$ (THz)	194.9524	194.0824
$\omega_m/(2\pi)$ (GHz)	4.7595	4.6044
$\kappa/(2\pi)$ (GHz)	2.27	1.99
$\kappa_e/2\pi$ (MHz)	810	790
$\gamma_0/(2\pi)$ (kHz)	620	100
$g_{om}/(2\pi)$ (kHz)	203	318

4.3.1 Silicon-on-sapphire optical nonlinearities

We first report on results with OMCs fabricated on the SOS platform. From Sec. 4.1.3, we expect a sapphire substrate to more efficiently conduct heat than the SiO_2 buried oxide (BOX) layer which is in direct contact with the devices in SOI. For this study, we fabricate two different SOS devices where the major difference is the number of unit cells in the defect region. Device SOSA is fabricated with a design very similar to the 31-unit-cell SOI device presented in Papers A and B, whereas device SOSB has only a single defect unit cell.

One of the advantages of SOS fabrication is that the sapphire is not etched by HF. This allows stripping of the silicon native oxide prior to cooling down. Oxide stripping and hydrogen passivation of surfaces have been proven to reduce optical absorption in silicon nano-structures [16, 123] and might have a significant impact on optical-absorption-induced thermal noise in silicon. We therefore treat the chips in 2 % HF solution for 30 s before preparing a cooldown. We generally achieve a loading time of 20–30 min between the acid treatment and applying vacuum to the cryostat sample chamber. When the cryostat is cold, we measure the optomechanical properties according to methods presented in Chapter 2 and Paper B appendices (Tab. 4.3). As for SOI, the longer SOS devices suffer from inhomogeneous broadening in the mechanical spectrum, causing closer spacing between mechanical modes (~ 5 MHz) and lower average optomechanical coupling than the 1-UC devices.

We conduct a study of optical nonlinearities in device SOSA with 31 unit cells which we directly compare to the results presented in Fig. 2 of Paper B (Fig. 4.9). From room temperature measurements, we see that the SOS device is even more optically stable than the release-free SOI device. Optical red-shifting is only achieved for $n_c > 10^5$, which is more than one order of magnitude compared to the release-free SOI device.

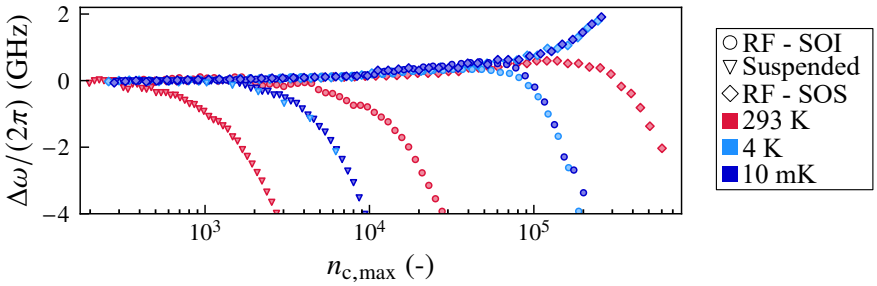


Figure 4.9: Nonlinear response of device SOSA (Tab. 4.3) compared to the data presented in Paper B Fig. 2. Data is gathered by sweeping a tunable laser over the OMC resonance and recording the frequency shift $\Delta\omega$ as a function of the maximally attained photon number $n_{c,max}$ at resonance. RF = Release-free.

This is evidence for the SiO_2 2 µm BOX layer acting as the bottleneck in thermal transport away from the silicon device region in SOI. Cooling down the device to cryogenic temperatures completely removes the red-shifting behavior in the explored n_c-region. The blue-shift that was also partially visible for the SOI device is now unobstructed by thermo-optic red-shift. As mentioned in Paper B, this is likely caused by free-carrier dispersion where the carriers are supplied through two-photon absorption [118].

The results in Fig. 4.9 seem to suggest an even greater thermal transport capability for the SOS material stack for both room temperature and cryogenic environments. However, the processes that govern the heat generating the thermo-optic effect are not guaranteed to overlap with those causing noise at 5 GHz. For that, we move on to thermometry.

4.3.2 Silicon-on-sapphire continuous-wave noise

In this continuous-wave experiment, we study the noise behavior of both SOSA and SOSB and compare it to the release-free SOI device. The calibration is performed with sideband asymmetry as described in Paper B Appendix E.

The data presented in Fig. 4.10 shows several interesting features. Despite the superior thermal transport of the sapphire substrate that is evident in the optical nonlinearity study, there is not a clear increase in noise robustness for both SOS devices compared to the SOI device. The

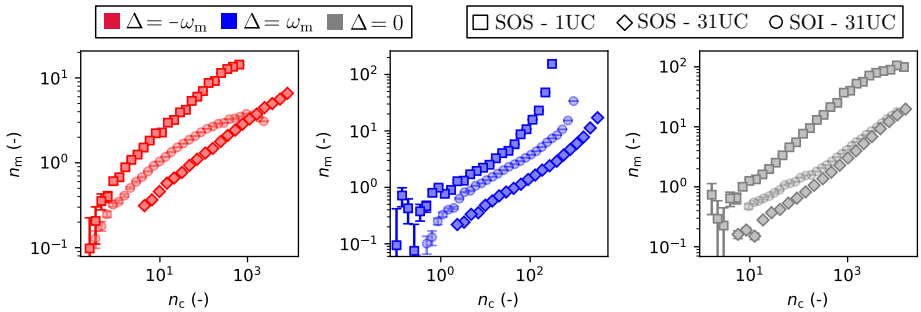


Figure 4.10: Continuous wave thermometry of SOS devices. Two devices with different number of unit cells (UC) are compared to the 31 UC SOI device presented in Paper B (faded circles). The shorter OMC exhibits more noise while the long SOS OMC shows exceptionally low n_m for $\Delta = \pm\omega_\mathrm{m}$ and small n_c. However, the lower optomechanical performance still allows the SOI device to be cooled to lower n_m in the high n_c regime.

1-UC device exhibits significantly more noise than the 31-UC SOI device for all detunings; at $n_\mathrm{c} \sim 10^3$, the difference almost reaches an order of magnitude for $\Delta = 0$. However, the 31-UC SOS device shows better performance, especially for $\Delta = \pm\omega_\mathrm{m}$ where $n_\mathrm{m} \approx 0.4$ for $n_\mathrm{c} = 10$. The advantage is also not as pronounced for $\Delta = 0$ where noise levels match the SOI device closely for $n_\mathrm{c} > 10^3$. Due to the weaker optomechanical coupling in the long SOS device, the SOI device also reaches lower cooled-noise levels for $\Delta = -\omega_\mathrm{m}$ and $n_\mathrm{c} > 10^3$.

Looking solely at absolute noise levels, we conclude that a HF-treated long SOS OMC design can surpass that of SOI, although not by a margin that justifies the lower optomechanical performance that can currently be reached in the SOS platform. Longer OMCs seem to consistently show lower noise levels, as has been observed for both SOS and SOI devices in separate studies. Longer OMCs have larger contact areas with the substrate and larger optical mode volumes, which lead to lower energy densities and field strengths at fixed n_c, potentially lowering nonlinear absorption effects. Compared to the thermo-optic effect studied in the previous section, the continuous-wave noise does not seem to benefit as much from the higher thermally conductive substrate. The underlying cause for this is not yet fully understood, but it could originate from disordered regions in the OMC material, such as the silicon surfaces or the silicon-sapphire interface, whose structure has yet to be studied in detail for this platform.

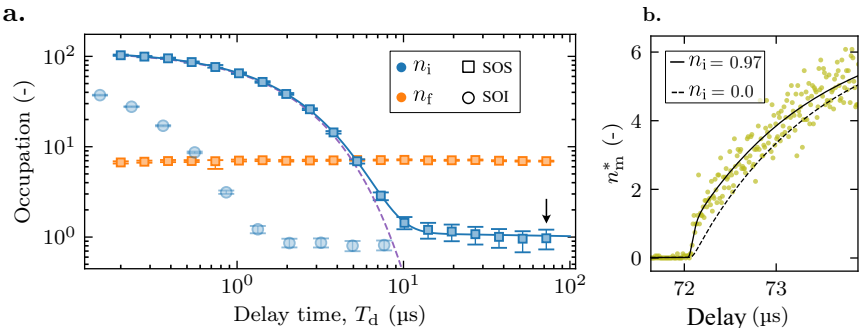


Figure 4.11: Coherent ringdown of device SOSB. **a.** Initial and final occupations during 10 µs readout pulses at time T_d following a modulated drive pulse. We fit the n_i data (solid blue) to an exponential decay (purple dashed) together with a slowly decaying contribution $\propto (T_d/(1\,\mu s))^{\alpha}$, with α being a fitting constant. Faded circles represent SOI data from Paper B Fig. 5f. **b.** Closer inspection of data to which we fit for the n_i-value marked with an arrow in **a**. We compare the best-fit curve yielding $n_i = 0.97$ to the same model with $n_i = 0$ to gauge the model's evidence for n_i-estimation.

4.3.3 Silicon-on-sapphire ringdown

In Fig. 5 of Paper B, we show that despite the release-free SOI OMCs' orders-of-magnitude-lower CW noise level at fixed n_c compared to the suspended alternative, together with their appreciable γ_{om}/n_c, the achieved pulsed noise fails to surpass previous demonstrations with suspended 1D and 2D OMCs [50, 28, 25]. This is partly due to a slowly decaying contribution to the noise following optical excitation. This causes the initial phonon occupancy n_i at the pulse start to be higher than expected, which acts as a lower bound for the average pulse noise (see Eq. (4.7)). Paper B Fig. 5f shows that the noise following coherent excitation initially decays as expected with time constant γ_0, which transitions into a slow decay for delay times T_d. We investigate the same effect for the SOS platform, using device SOSB with 1 defect UC due to its superior γ_{om}/n_c.

The experiment is set up equally to the one presented in Paper B Fig. 5b,d,f, in which a red-detuned drive pulse modulated at the mechanical frequency rings up the mechanics to a bright coherent state. The decay of the coherent state is then read out by another red-detuned pulse at delay time T_d. The laser power for both drive and readout pulses is set to $n_c = 80$. The calibrated and filtered phonon dynamics waveform $n_m^*(t)$ is fitted to extract n_i and n_f as described in Paper B.

The results are presented in Fig. 4.11a and show striking similarity

to Paper B Fig. 5f. For $T_\mathrm{d} \lesssim 5\,\mu\mathrm{s}$, the behavior is governed by an exponential decay with time constant $\gamma_0/(2\pi) \approx 100\,\mathrm{kHz}$, which agrees with Electromagnetically induced transparency (EIT) measurements. However, as for the SOI device, we see that the decay tapers off for higher T_d. Strikingly, despite a factor of 5 difference in γ_0, the slow-down of both SOI and SOS data is initiated at a phonon level ~ 1. This similarity raises questions about the measurement noise floor. The lowest measurable n_i is governed by n_NEP and the evidence in the data for the phonon dynamics model we fit. For this experiment, n_NEP is limited by dark count noise and is estimated to be < 0.01 for $\Gamma_\mathrm{cal} = 8.6\,\mathrm{cps}$, $\Gamma_\mathrm{DCR} \approx 6\,\mathrm{cps}$, and $n_\mathrm{c} = 80$ (Paper B Appendix H). We also closely inspect the data for large T_d, which indicates that the Bayesian fitting model has evidence for n_i in the estimated range (Fig. 4.11b).

The fact that the slowly decaying contribution to the thermal noise starts to dominate at a phonon occupation of $n_\mathrm{m} \approx 1$ is intriguing. Although we showed in Paper B Appendix I that n_i at $T_\mathrm{d} = 10\,\mu\mathrm{s}$ is dependent on the experiment duty cycle, the fact that it emerges at $n_\mathrm{m} \approx 1$ still remains. A limit of the present experiment is that we cannot properly distinguish between occupancy contributions from the coherent state and the thermal noise when these are comparable in magnitude. A full state tomography would tell us more about the full evolution of the state, from the initial bright coherent state with $n_\mathrm{m} \sim 100$ to the final thermal state at $n_\mathrm{m} \sim 1$.

The data supports the hypothesis that both SOI and SOS devices are limited by the same underlying mechanism. The strong connection to occupancies ~ 1 alludes to an interplay between the OMC mechanical mode and fermionic systems such as TLS, which has previously been suggested to affect mechanical decay [141]. However, the dynamics does not seem to differ drastically between SOS and SOI despite the SOS sample's crystalline sapphire substrate and its HF surface treatment before cooldown to limit the presence of TLS-ridden native oxides. Although the SOS sample is expected to have a lower TLS density, we currently have no way of experimentally confirming this hypothesis. Therefore, further investigations of the composition of the SOS material stack are required before further evaluating the capabilities of the SOS platform.

4.3.4 Suspended pinch-mode OMC

The suspended device presented in Paper B was fabricated from a design expected to yield high optomechanical coupling and mechanical

Table 4.4: Optomechanical properties of the suspended pinch-mode OMC.

Property	Value
$\omega_o/(2\pi)$ (THz)	193.3907
$\omega_m/(2\pi)$ (GHz)	3.0832
$\kappa/(2\pi)$ (GHz)	1.25
$\kappa_e/2\pi$ (MHz)	370
$\gamma_0/(2\pi)$ (kHz)	64
$g_{om}/(2\pi)$ (kHz)	668

Q. In addition to the OMC mirror region, this design also used 2D phononic shielding as presented in Ref. [100]. The long mechanical $T_1 = \gamma_0^{-1} \approx 300\,\mu s$ along with its high steady-state noise levels makes it unsuitable for high repetition rate pulsed experiments. For such fast pulsed experiments, deliberately designing the devices for reduced mechanical Q is a common way to increase repetition rates at fixed noise [48, 50].

To study noise performance of a low Q_m suspended OMC, we here take a different approach. We start from one of our 1 UC release-free OMCs designed to have pinch-mode mechanical resonance at $\sim 4.2\,GHz$ (Sec. 3.3.3); we then release the OMCs using hydrofluoric acid (HF) vapor. As in Ref. [19], this creates a suspended OMC that supports a pinch-like mechanical mode (Fig. 4.12a) with optomechanical coupling based on similar principles as presented for release-free pinch-mode optomechanics in Sec. 3.1.3. For this design, we also exclude the 2D phononic shielding, which is beneficial for lower mechanical Q and for stronger thermal anchoring to the chip bulk. After fabrication, we cool down the chip and choose a device with appreciable optomechanical properties for thermometry measurements (Tab. 4.4). In this test, the chip was not surface treated with HF before cooldown, giving it similar measuring conditions to both devices studied in Paper B.

Through single-pulse ringdown measurements similar to those performed and presented in Paper B Fig. 3d, we determine the mechanical decay rate at no applied optical power to be $\gamma_0/(2\pi) = 64\,kHz$. This is almost 200 times lower than the breathing-mode OMC from Paper B and makes the suspended pinch-mode OMC comparable to breathing-mode OMCs with lightly engineered phonon leakage [48].

As in previous studies, we start thermometry measurements by studying noise under CW pumping (Fig. 4.12b). This time, we compare to the

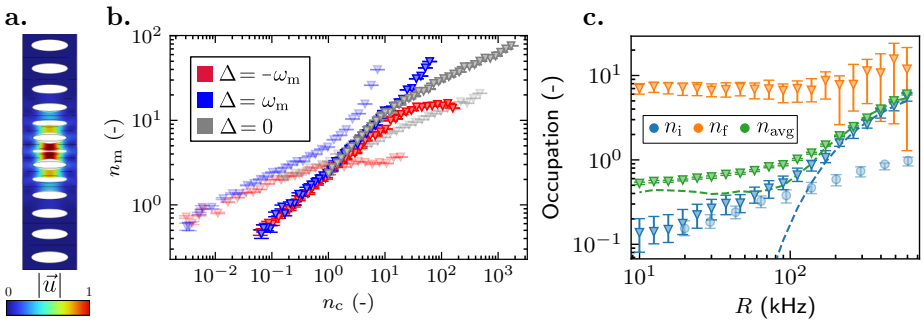


Figure 4.12: Suspended pinch-mode thermometry. **a.** Mechanical displacement field of a pinch-like mechanical mode in a suspended silicon nanobeam. **b.** Continuous-wave thermometry of a suspended pinch-mode OMC for red, blue and resonant detunings. Faded data points represent the breathing-mode suspended OMC presented in Paper B. **c.** Red-detuned pulsed noise analysis of the suspended pinch-mode OMC where $T_p = 100\,\text{ns}$ and $n_c = 72$ to reach $p_{as} = 5\,\%$. We include the projected behavior of n_i given $\gamma_0/(2\pi) = 64\,\text{kHz}$ (blue dashed) and n_{avg} (green dashed) using (4.6), the projection for n_i, and the measured n_f. Faded data points represent n_i data from Paper B Fig. 5e.

suspended breathing-mode OMC from Paper B and find several noteworthy features. We first note the noise trend as a function of n_c. For the breathing-mode OMC, the behavior is captured by a single power-law function with exponent 0.29. For the pinch-mode OMC, this is not the case, and the trend is better described by two power-law functions. For high n_c, the exponent of 0.33 matches that of the breathing-mode OMC to a reasonable extent, while for low n_c, the exponent is significantly higher at 0.72. Due to the noise's strong n_c-dependence for low n_c, the pinch-mode OMC exhibits lower noise levels at low powers compared to the breathing-mode OMC; however, the advantage is lost at higher powers due to the same effect. In addition, the higher γ_0 increases the power needed to reach $C_{om} = 1$, which leads to higher cooled-noise levels for high n_c at $\Delta = -\omega_m$.

A possible explanation for the split power-law dependence is a shift in the dominant internal dephasing rate. For the breathing-mode OMC where $\gamma_0/(2\pi) = 528\,\text{Hz}$, the dominant contribution to the internal mechanical linewidth under optical pumping is γ_p, which can be in the range of 10 kHz for $n_c = 10$ [119], as supported by our data. With $\gamma_0/(2\pi) = 64\,\text{kHz}$, an n_c-threshold likely exists where $n_0\gamma_0 \sim n_p\gamma_p$. Within this hypothesis, the noise should be limited by $n_m \approx n_0$ for low n_c. Even though the noise is lower in this regime, it still corresponds to

a significantly higher effective temperature than the fridge temperature for the applied optical power (Sec. 4.2). Similarly to what was concluded for the release-free SOI OMC in Paper B, this suggests that the "cold" bath coupled to the OMC through γ_0 can be significantly warmer than the fridge temperature.

Finally, we study short pulse noise for the suspended pinch-mode OMC. The study is set up to be comparable to the experiment presented in Paper B Fig. 5e. Red-detuned pulses with length $T_\mathrm{p} = 100\,\mathrm{ns}$ and optical power $n_\mathrm{c} = 72$ are used to reach $p_\mathrm{as} = \gamma_\mathrm{om} T_\mathrm{p} = 5\,\%$. As in previous pulsed experiments, we use the methods described in Paper B Appendix F to fit for n_i, n_f, and n_avg (Fig. 4.12c). For high repetition rates $R \sim \gamma_0$, the initial occupation follows exponential decay expected from γ_0. In this regime, the average noise is strongly limited by n_i, which causes large uncertainty in the estimated n_f. The quickly decaying behavior of n_i is, however, not retained for $R \lesssim 100\,\mathrm{kHz}$, which causes n_avg to stay largely n_i-limited for $R \gtrsim 20\,\mathrm{kHz}$. For lower R, n_avg approaches the limit set by n_f through $T_\mathrm{p}\gamma_\mathrm{m}/2 \approx 0.06$ (see Eq. (4.7)), for $\gamma_\mathrm{m} = \gamma_0 + \gamma_\mathrm{p} + \gamma_\mathrm{om} = 2\pi \cdot 190\,\mathrm{kHz}$, which we measure separately at this detuning and power.

The transition from quick to slow decay exhibited by n_i for the pinch-mode OMC is strikingly similar to what we measure for release-free devices (Sec. 4.3.3). In addition, the decay of n_i for lower R seems to line up with the SOI data from Paper B Fig. 5e (Fig. 4.12c). This behavior is drastically different from other reports on pulsed noise in suspended silicon OMCs. Low-Q_m suspended breathing-mode OMCs have shown pulsed noise $n_\mathrm{avg} \sim 0.1$ with $T_\mathrm{p} = 40\,\mathrm{ns}$, $p_\mathrm{as} = 5\,\%$ at $50\,\mathrm{kHz}$ [50], whereas a 2D OMC has shown $n_\mathrm{avg} \sim 0.01$ for similar conditions with $T_\mathrm{p} = 80\,\mathrm{ns}$ [28]. For the present suspended pinch-mode device, this limit would not be attainable due to the slowly decaying n_i.

Recalling the discussion in Sec. 4.3.3, we note that the absence of HF surface treatment of the suspended pinch-mode OMC prior to cooldown provides a possible explanation for the slow decay of n_i. Removal of the native oxide prior to cooldown was part of the fabrication procedure used in the 2D OMC study [28] and was subsequently identified as a potential means of reducing noise in the full 2D transducer based on the same OMC, which exhibited an order-of-magnitude increase in noise [116]. If the slowly decaying noise originates from interactions with TLS in unstructured regions of the OMC material, suspension combined with native-oxide removal may be the most effective means of suppressing this

noise source. Even the SOS platform still contains the silicon–sapphire interface, which may itself host TLS. An alternative explanation for the similar noise dynamics observed across different samples and architectures is that heat transport is limited by the thermal link between the chip and the cryostat. However, this hypothesis does not readily account for the observed dependence of the noise decay on phonon number.

We conclude that, given the common noise dynamics observed in both release-free and suspended devices, there remains much to be understood about optically induced thermal noise in silicon. Additional experiments that would be conducted in future studies to further elucidate the situation includes: study a low-Q_{m} suspended device with proper HF surface treatment, study the effect of local chip heating by optically addressing several devices on the same chip simultaneously, and performing FGA in addition to HF surface tretment of SOS samples for further limiting P_b-style defects in the silicon.

CHAPTER 5

Release-free piezo-optomechanical transducer

The goal of understanding and reducing optically induced thermal noise in silicon optomechanical crystals discussed in the previous chapter represents the major scientific contribution of this thesis; however, within a broader context, it is but one part of a longer journey. A possible application for the release-free optomechanical crystal cavity (OMC) are within microwave-to-optical (MO) quantum transducers. Quantum computing with superconducting qubits is a promising avenue to realizing fault-tolerance but faces challenges with scalability [41]. An MO quantum transducer partly based on OMC technology has the potential to reduce scalability issues through remote entanglement [42]. Work throughout this thesis has thus been directed toward integrating release-free OMCs within a quantum MO transducer, which is the subject of this chapter.

In Paper C, we present fabrication and room-temperature measurements of a release-free piezo-optomechanical transducer fabricated on the silicon-on-insulator (SOI) platform. The task of conceptualizing, designing, and fabricating this type of device is a great challenge that requires significant effort from a group of talented researchers. As not being part of this thesis work, design and fabrication will not be covered in detail here. More details on this can be found in Refs. [83, 85]. Instead, this chapter focuses on giving further theoretical context to the release-free transducer and to provide more details on the room-temperature measurements of this first-generation release-free transducer.

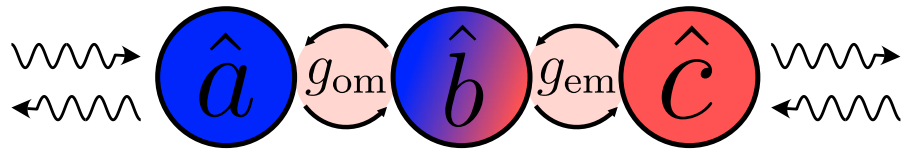


Figure 5.1: Schematic of the electro-optomechanical transduction process. An optical mode $\hat{a}$ couples to the microwave mode $\hat{c}$ through the intermediary mechanical mode $\hat{b}$. Five orders of magnitude separates the optical mode with angular frequency $\omega_{\mathrm{o}} \approx 2\pi \cdot 200\,\mathrm{THz}$ and the mechanical/microwave modes with $\omega_{\mathrm{m}} \approx \omega_{\mu} \approx 2\pi \cdot 5\,\mathrm{GHz}$. Transduction across the large frequency gap is governed by optomechanical coupling rate g_{om}, whereas a resonant electromechanical coupling g_{em} links mechanical and microwave domains.

5.1 Background

5.1.1 Phonons as transduction intermediaries

A quantum MO transducer is commonly modeled as a set of coupled resonator modes. For a transducer using a phononic degree-of-freedom as an intermediary, the modes are labeled $\hat{a}$, $\hat{b}$ and $\hat{c}$ for optics, mechanics and microwaves, respectively (Fig. 5.1). Transduction is enabled when the modes are coupled through zero-point coupling rates g_{om} for optomechanics and g_{em} for the microwave-mechanics coupling termed *electromechanics*. The physical representation of the three modes differ vastly between transducer implementations. Among the most promising approaches within this family of transducers one finds: optomechanical nanostructures with electromechanics enabled through piezoelectric materials [43, 142, 45, 143, 46, 116], or through capacitive coupling [144]; piezo-functionalized bulk-acoustic wave resonators in macroscopic optical cavities [145]; and capacitively coupled silicon-nitride membranes in macroscopic optical cavities [67]. The optomechanical crystals developed and characterized during this thesis are designed for integration into a piezo-optomechanical-style transducer, which utilizes the strong piezoelectricity of lithium niobate (LN) to achieve a mechanical mode with simultaneous electro- and optomechanical coupling.

5.1.2 Piezoelectricity

In previous chapters, we discussed the optomechanical interaction achieved in the release-free optomechanical crystal. For a transducer using a phononic mode as an intermediary, this makes up one of two essential interactions – the other being electromechanics. Being a piezo-optomechanical transducer the release-free transducer is designed to rely on piezoelectricity.

Piezoelectricity is a material property found in materials lacking inversion symmetry. When a piezoelectric material is put under mechanical strain, a voltage builds across the object. This effect can also be applied conversely, that is to say a mechanical strain can be induced by applying voltage across the object. As opposed to optomechanics which is quadratic, piezoelectricity is linear, i.e., strain and electric field have a linear dependence. In such a material, the constitutive relations for acoustic and electromagnetic fields (see Sec. 2.1) are coupled through the definition [58]

$$D_i = \varepsilon_{ij}^S E_j + e_{ijk} S_{jk}, \tag{5.1}$$

$$\sigma_{ij} = c_{ijlm}^E S_{lm} - e_{lij} E_l. \tag{5.2}$$

Here we see that strain polarizes the material, causing an extra contribution to the electric displacement field in (5.1). Conversely, an applied electric field causes an extra induced stress in the material in the second term of (5.2). The material property that governs this interaction is described by the piezoelectric tensor e_{ijk}. In addition, due to the fields affecting the material properties through stress and polarization, it is important to note that ε_{ijk} and c_{ijkl} must be measured at constant applied electric field and strain, hence the superscripts E and S.

5.2 Transducer theory

5.2.1 Piezo-optomechanical Hamiltonian

The piezoelectric coupling between acoustic and electromagnetic fields can be formalized much in the same way as the optomechanical interaction treated in Chapter 2. The additional terms in the constitutive relations naturally lead to corrections to the fields' stored energy expressed by their Hamiltonians. From there, field dynamics can be derived as was explored in Sec. 2.2.3. However, as design and fabrication of the

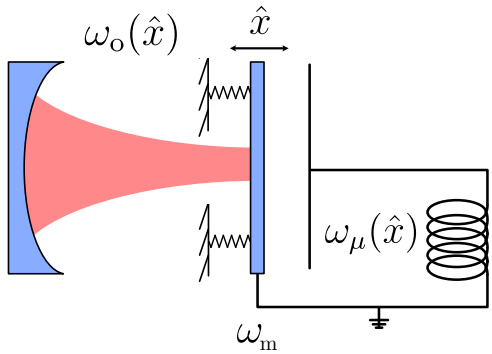


Figure 5.2: Schematic of an electro-optomechanical system. A mechanical mode has angular frequency ω_{m} and displacement $\hat{x}$. While moving, the mechanical mode changes the length of both a Fabry–Pérot cavity and the capacitor of an LC-resonator, thus modulating both of their resonance frequencies ω_{o} and ω_{μ}.

full piezo-optomechanical transducer are not a major part of this thesis, we will move immediately to the modal description which allows us to analyze the behavior of the transducer experimentally.

We thus consider a general system where a mechanical mode, through its movement, is modulating the resonance frequency of a Fabry–Pérot optical cavity (Fig. 5.2). In parallel to this, we also introduce a microwave LC resonator with a capacitor which is also affected by the movement of the mechanical mode. The electromechanics of this picture generally supports both linear and nonlinear interactions, but when applying a large bias voltage over the capacitor, the Hamiltonian for this system (expressed in the rotating frame for the optics) can be linearized as

$$\hat{H}_{\mathrm{tot}}/\hbar = -\Delta\hat{a}^{\dagger}\hat{a} + \omega_{\mathrm{m}}\hat{b}^{\dagger}\hat{b} + g_{\mathrm{om}}\hat{a}^{\dagger}\hat{a}(\hat{b}+\hat{b}^{\dagger}) + g_{\mathrm{em}}(\hat{b}+\hat{b}^{\dagger})(\hat{c}+\hat{c}^{\dagger}), \quad (5.3)$$

and is equivalent to the direct coupling of piezoelectricity [39]. Just as the linearized optomechanical Hamiltonian facilitates conversion between optical photons and acoustic phonons, we have that (5.3) opens up a transition between optical and microwave photons.

5.2.2 Transducer scattering parameters

From the Hamiltonian (5.3), we can once again derive a set of coupled mode equations (CME) that describe the dynamics of the system. This system of equations then describes the efficiency, bandwidth and added

noise of a transducer in operation. However, having introduced the microwave mode $\hat{c}$, which also comes with input and output channels, the complexity of the solutions is substantially increased. But under the right assumptions and approximations, analytical solutions can be obtained which can bring valuable insights to the workings of a transducer.

We study the dynamics of (5.3) under the rotating wave approximation (RWA) with linearized beam-splitter-Hamiltonian optomechanics obtained through pumping the optical system with a red-detuned laser ($\Delta = -\omega_\mathrm{m}$). Under these assumptions, the CMEs are linear and form a closed set of equations for the combined field variable $\hat{\boldsymbol{a}} = [\hat{a}, \hat{b}, \hat{c}]^T$ – meaning that the equations for annihilation and creation operators are not independent under Hermitian conjugation. To the combined field variable, we introduce the input operator $\hat{\boldsymbol{a}}_\mathrm{in} = [\hat{a}_\mathrm{in,e}, \hat{a}_\mathrm{in,i}, \hat{b}_\mathrm{in,0}, \hat{c}_\mathrm{in,e}, \hat{c}_\mathrm{in,i}]^T$, where $\hat{c}_\mathrm{in,e/i}$ are microwave input operators from external/internal sources[1]. Finally, we assume output channels for all modes through a combined output operator $\hat{\boldsymbol{a}}_\mathrm{out} = [\hat{a}_\mathrm{out,e}, \hat{a}_\mathrm{out,i}, \hat{b}_\mathrm{out,0}, \hat{c}_\mathrm{out,e}, \hat{c}_\mathrm{out,i}]^T$.

With the same procedure which brought us to (2.21), we derive the piezo-optomechanical CMEs presented below in matrix form along with the input-output relation [146, 147]:

$$\frac{\mathrm{d}}{\mathrm{d}t}\hat{\boldsymbol{a}}(t) = A\hat{\boldsymbol{a}}(t) + B\hat{\boldsymbol{a}}_\mathrm{in}(t),\ \hat{\boldsymbol{a}}_\mathrm{out}(t) = I_5\hat{\boldsymbol{a}}_\mathrm{in}(t) - B^T\hat{\boldsymbol{a}}(t). \tag{5.4}$$

In the above, we have that

$$\begin{aligned} A &= \begin{pmatrix} i\Delta - \kappa_\mathrm{o}/2 & -iG_\mathrm{om} & 0 \\ -iG_\mathrm{om} & -i\omega_\mathrm{m} - \gamma_0/2 & -ig_\mathrm{em} \\ 0 & -ig_\mathrm{em} & -i\omega_\mu - \kappa_\mu/2 \end{pmatrix}, \\ B &= \begin{pmatrix} \sqrt{\kappa_\mathrm{oe}} & \sqrt{\kappa_\mathrm{oi}} & 0 & 0 & 0 \\ 0 & 0 & \sqrt{\gamma_0} & 0 & 0 \\ 0 & 0 & 0 & \sqrt{\kappa_{\mu\mathrm{e}}} & \sqrt{\kappa_{\mu\mathrm{i}}} \end{pmatrix}, \end{aligned} \tag{5.5}$$

and I_N is an $(N \times N)$ identity matrix. Solving for the output modes in the frequency domain yields

$$\hat{\boldsymbol{a}}_\mathrm{out}(\omega) = S(\omega)\hat{\boldsymbol{a}}_\mathrm{in}(\omega), \tag{5.6}$$

where $S(\omega) = I_5 + B^T(i\omega I_3 + A)^{-1}B$ is the amplitude scattering matrix. The scattering matrix contains all transfer functions relating the

[1]Note that unlike the optical input/output operators $\hat{a}_\mathrm{in,e/i}$, the microwave operators $\hat{c}_\mathrm{in,e/i}$ couple to thermal baths with non-zero occupation.

input of one mode – being either noise or signal – to the output of another (Fig. 5.3a). The MO transduction efficiency $\eta_{o\mu}(\omega)$ can thus be calculated as

$$\eta_{o\mu}(\omega) = |S_{14}(\omega)|^2 = |S_{41}(\omega)|^2 = \eta_{\mu o}(\omega), \tag{5.7}$$

which can be understood as the probability for a photon of frequency ω to avoid loss channels and pass through the transducer[2]. Calculating $S(\omega)$ yields the following expression for the MO efficiency:

$$\begin{aligned}
\eta_{o\mu}(\omega) &= \frac{G_{om}^2 g_{em}^2 \kappa_{\mu e} \kappa_{oe}}{|G_{om}^2 \chi_\mu^{-1} + g_{em}^2 \chi_o^{-1} + \chi_\mu^{-1}\chi_o^{-1}\chi_m^{-1}|^2}, \\
\chi_o &= \chi_o(\omega) = (-i(\omega + \Delta) + \kappa_o/2)^{-1}, \\
\chi_m &= \chi_m(\omega) = (-i(\omega - \omega_m) + \gamma_0/2)^{-1}, \\
\chi_\mu &= \chi_\mu(\omega) = (-i(\omega - \omega_\mu) + \kappa_\mu/2)^{-1},
\end{aligned} \tag{5.8}$$

where κ_o (κ_μ) and κ_{oe} ($\kappa_{\mu e}$) are total and external optical (microwave) losses, and ω_μ is the microwave resonance frequency.

In the case of red detuning and $\omega_\mu = \omega_m$, the spectral dependence of $\eta_{o\mu}$ is sharply centered around $\omega = \omega_m$ with some associated bandwidth. In Fig. 5.3b, we plot the transducer efficiency along with the other 4 scattering parameters as functions of ω with device parameters given in Tab. 5.1. We see that for the given electromechanical parameters, the mechanical and microwave modes hybridize, causing a splitting equal to $2g_{em}$. At higher n_c, the optomechanical scattering rate γ_{om} exceeds g_{em}, causing the splitting to revert.

The requirements of quantum transduction on the efficiency are dependent on the specific mode of operation chosen for the transducer. Direct quantum transduction in which quantum states are directly transferred between microwave and optical domains requires efficiency approaching unity. However, entanglement-based protocols based on spontaneous parametric down-conversion (SPDC) achieved while operating the transducer in the two-mode-squeezing state of blue detuning ($\Delta = \omega_m$), are significantly less restrictive and can achieve microwave-optical entanglement for $\eta_{oe} \ll 1$ [146]. A common metric to quantify the generation rate of remote entanglement through such a protocol is the efficiency-bandwidth product [144]

$$B = \int \eta_{oe}(\omega) \mathrm{d}\omega. \tag{5.9}$$

[2]In the optical domain, ω corresponds to a photon of frequency $\omega_l + \omega$ due to the rotating frame applied to $\hat{a}$.

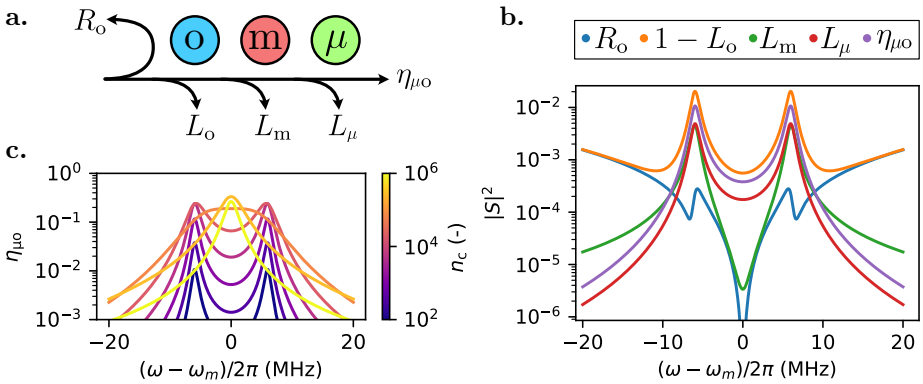


Figure 5.3: Scattering parameters for optical-to-microwave transduction. **a.** Schematic of scattering parameters with optical reflection coefficient $R_o = |S_{11}|^2$; loss coefficients $L_o = |S_{21}|^2$, $L_m = |S_{31}|^2$, $L_\mu = |S_{51}|^2$; and optical-to-microwave efficiency $\eta_{\mu o} = |S_{41}|^2$. **b.** Frequency dependence of the scattering parameters as a function of ω for a transducer with parameters given in Tab. 5.1 and $n_c = 100$. **c.** Transduction efficiency with the same device parameters as **b** for varying n_c.

Table 5.1: Piezo-optomechanical parameters used for simulating $S(\omega)$. Parameters extracted from [83, 46].

Parameter	Value (2π)
ω_m	4.77 GHz
ω_μ	4.77 GHz
Δ	−4.77 GHz
γ_0	500 kHz
κ_o	1 GHz
κ_{oe}	0.5 GHz
κ_μ	1.75 MHz
$\kappa_{\mu e}$	1.2 MHz
g_{om}	0.24 MHz
g_{em}	6 MHz

We calculate this property for a projected release-free quantum transducer with parameters from Refs. [83, 46] in Appendix K of Paper B while investigating the effect of stronger cold-bath coupling γ_0 to the performance of the transducer.

5.3 Design

The core of the transducer design is the mechanical mode which links optical and microwave domains (Fig. 5.1). The mode must therefore have two drive interfaces: one for optical signals and one for microwaves. The optomechanical interface was explored in detail in Chapter 3, where we designed OMCs which comprise an optically drivable acoustic vibration confined to a silicon nanobeam in firm contact with the chip surface (Fig. 5.4a). In parallel to this, we also design electromechanical crystals (EMC), with the purpose of providing the microwave interface. The EMCs are fabricated with similar design principles as the OMC to support a confined pinch-mode mechanical vibration in a release-free patterned nanobeam (Fig. 5.4b). The crucial difference between EMC and OMC is in the material choice, where the EMC nanobeam is fabricated from a thin-film LN on either silicon or sapphire substrates. By evaporating metal electrodes in a periodic pattern across the EMC and choosing the correct LN crystallographic orientation, the pinch-mode is effectively driven by applying a microwave field to the electrodes. These release-free EMCs have been shown to exhibit strong electromechanical coupling $g_{\mathrm{em}}/(2\pi) \approx 30\,\mathrm{MHz}$ to a high-impedance microwave resonator [85].

With the two basic building blocks in place, we turn to integrating them into one common device [83]. To limit optical losses, the optical mode must be kept away from the metal electrodes of the EMC. A solution to this is to spatially separate the device to have distinct opto- and electromechanical regions. The silicon optomechanical region supports a tightly confined optical field and generates optomechanical coupling, while the electromechanical region supports microwave driving through piezoelectric LN. By letting the mechanical mode extend into both regions, we achieve opto- and electromechanical coupling through sacrificing mechanical mode confinement. The LN is applied to part of the device through micro-transfer printing which has successfully been utilized in previous piezo-optomechanical transducer systems [45, 143]. Finally, the release-free nature of the device forces the transition region

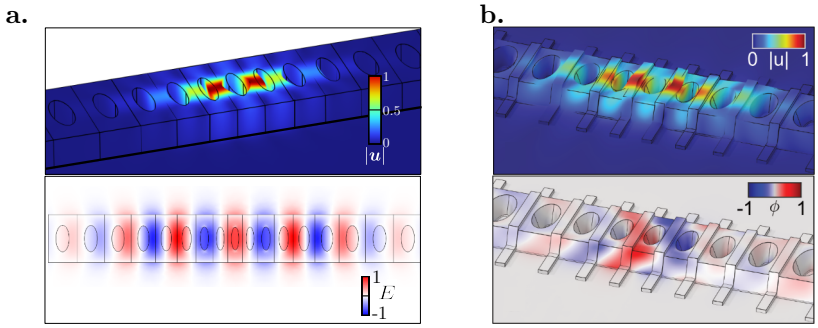


Figure 5.4: Basic components of a release-free piezo-optomechanical transducer. **a.** Release-free SOI optomechanical crystal with pinch-mode mechanics. Features the mechanical mode's displacement field (top) and the optical mode's transverse electric field (bottom). **b.** Lithium niobate electromechanical crystal on silicon or sapphire substrates with transverse aluminum electrodes and pinch-mode mechanics [85]. Figures depict acoustic displacement field (top) and electrostatic potential ϕ (bottom). All fields are normalized.

– the part connecting opto- and electromechanical regions – to be specifically crafted to limit mechanical scattering into the substrate [83].

The transducer design of Paper C is presented in Fig. 5.5b which features a silicon nanobeam with opto- and electromechanical regions as discussed above. This first-generation device has resonant modes for optical and mechanical fields, leaving the complexity of full integration with a microwave mode to future work. However, the mechanical mode can still be electrically driven through the electromechanical region which is connected to a $50\,\Omega$ microwave feedline. Due to the electromechanical coupling, the feedline acts as an external decay channel for the mechanical mode which is quantified with the electromechanical decay rate γ_μ.

5.4 Room-temperature transduction

The experiments presented in Paper C are performed at room temperature with similar methods as described in Sec. 3.3. In this section, we go into a bit more detail about the methods that were left out from the manuscript.

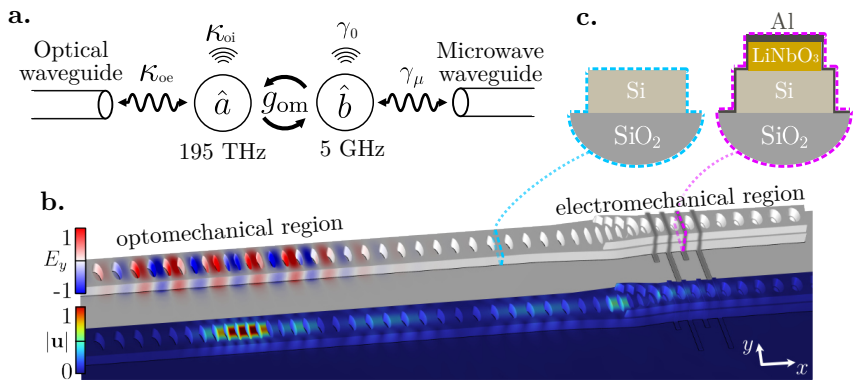


Figure 5.5: a. Transducer mode diagram. Optical mode $\hat{a}$ and mechanical mode $\hat{b}$ couple through optomechanical coupling g_{om}. In addition, the optical mode couples to an optical waveguide and its environment with rates κ_{oe} and κ_{oi}, respectively. Finally, the mechanical mode decays into its environment with rate γ_0 and into the microwave waveguide with electromechanical decay rate γ_μ. **b.** Normalized transverse electric field and acoustic displacement field of the transducer optical and mechanical modes, respectively. **c.** Cross section of the material stack for opto- and electromechanical regions.

5.4.1 Continuous-wave microwave-to-optical transduction

To measure the electromechanical decay rate γ_μ, we use a continuous-wave microwave tone to drive the piezoelectric side of the transducer. Through the MO transduction, this generates a signal in the optical domain which we detect with the high-speed photo-detector (HSPD) that was also used to measure the thermomechanical sideband described in Sec. 3.3.2.

To describe this mathematically, we return to the solutions of the cavity optomechanical CMEs (App. B.2). We can study these solutions since we have not in this design introduced a microwave mode, meaning that the microwave channel can be treated as an external decay channel with input operator $\hat{b}_{\mathrm{in},\mu}$ which couples to $\hat{b}$ with $\sqrt{\gamma_\mu}$. If we treat the input as a classical, steady-state drive with frequency ω_μ, we have that:

$$\langle \hat{b}_{\mathrm{in},\mu}(\omega')\hat{b}_{\mathrm{in},\mu}(\omega)\rangle = 2\pi\Phi_{\mathrm{in},\mu}\delta(\omega-\omega_\mu)\delta(\omega+\omega'), \tag{5.10}$$

where $\Phi_{\mathrm{in},\mu}$ is the input microwave photon flux. Now, we can repeat the calculation leading to the thermomechanical power spectral densities (PSD) of the output optical mode (see Sec. 2.4.4) – with the microwave drive as an addition. While assuming room temperature, i.e., $n_0 \approx$

$1400 \gg 1$, we get

$$S_{\hat{a}_{\mathrm{out,e}}}(\omega)\Big|_{\Delta=\mp\omega_{\mathrm{m}}} = \int \langle \hat{a}^{\dagger}_{\mathrm{out,e}}(\omega')\hat{a}_{\mathrm{out,e}}(\omega)\rangle \mathrm{d}\omega' \approx \frac{\gamma_{\mathrm{om}}\eta_{\mathrm{o}}}{(\omega \mp \omega_{\mathrm{m}})^2 + \gamma_{\mathrm{m}}^2/4}\left[n_0\gamma_0 + 2\pi\Phi_{\mathrm{in},\mu}\delta(\omega-\omega_\mu)\right]. \tag{5.11}$$

In (5.11), we use $\gamma_{\mathrm{m}} = \gamma_0 + \gamma_\mu \pm \gamma_{\mathrm{om}}$ and we adiabatically eliminate the optical mode to approximate $\chi_{\mathrm{o}}^{-1}(\omega) \approx \kappa/2$. The two terms in (5.11) represent a thermal Lorentzian peak at ω_{m} with full-width-half-maximum (FWHM) γ_{m} and a coherent peak at ω_μ. These contributions can both be observed in the power spectrum of the HSPD output (see Paper C Fig. 2a). Using (5.11), we can calculate the total photon flux in these two contributions when $\omega_\mu = \omega_{\mathrm{m}}$

$$\begin{aligned}\Gamma|_{\Delta=\mp\omega_{\mathrm{m}}} &= \frac{1}{2\pi}\int \mathrm{d}\omega\; S_{\hat{a}_{\mathrm{out,e}}}(\omega)\Big|_{\Delta=\mp\omega_{\mathrm{m}}} \\ &= \frac{\gamma_{\mathrm{om}}\eta_{\mathrm{o}}n_0\gamma_0}{\gamma_{\mathrm{m}}} + \frac{4\gamma_{\mathrm{om}}\eta_{\mathrm{o}}\Phi_{\mathrm{in},\mu}\gamma_\mu}{\gamma_{\mathrm{m}}^2} \\ &:= \Gamma_{\mathrm{th}} + \Phi_{\mathrm{in},\mu}\eta_{\mathrm{o}\mu} := \Gamma_{\mathrm{th}} + \Gamma_{\mathrm{coh}}\end{aligned} \tag{5.12}$$

Here, we defined the thermal and coherent photon fluxes Γ_{th}, Γ_{coh} along with the MO conversion efficiency $\eta_{\mathrm{o}\mu} = 4\gamma_{\mathrm{om}}\gamma_\mu\eta_{\mathrm{o}}/\gamma_{\mathrm{m}}^2$ for $\omega = \omega_{\mathrm{m}}$. The ratio of the photon fluxes can readily be obtained through the ratio of the integrated thermal and coherent signals on the HSPD power spectrum. Using this, we can isolate the electromechanical decay rate γ_μ through

$$\gamma_\mu = \frac{\gamma_{\mathrm{m}}\gamma_0 n_0}{4\Phi_{\mathrm{in},\mu}}\frac{\Gamma_{\mathrm{coh}}}{\Gamma_{\mathrm{th}}}. \tag{5.13}$$

For weak opto- and electromechanical coupling, we have that $\gamma_0 \approx \gamma_{\mathrm{m}}$ meaning that γ_μ can be calculated with data given exclusively by the HSPD power spectrum. Together with optomechanical parameters given through methods discussed in Chapter 2, the full transducer efficiency can be calculated.

5.4.2 Classical signal transmission

Lastly, we give some more details on the classical signal transmission experiment where input pulses generated in the microwave domain are upconverted to optical frequencies using the transducer.

The transducer is continuously pumped by an input laser tuned to either the red or the blue sideband ($\Delta = \pm\omega_{\mathrm{m}}$). Since the transducer is

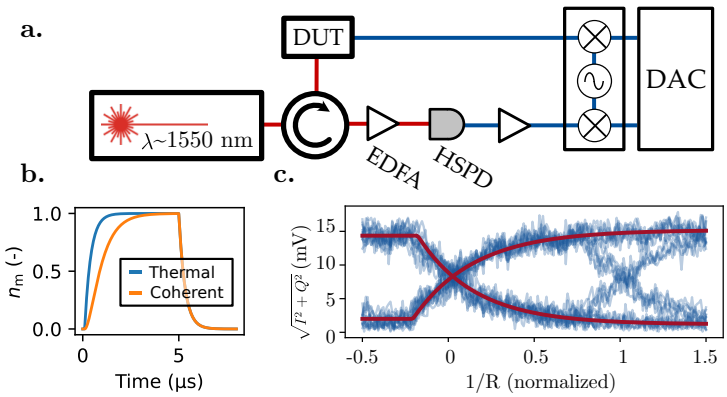


Figure 5.6: **a.** Schematic of the bit-string experiment presented in Paper C. A CW laser tuned to either red or blue sideband is amplified and detected on an HSPD. A digital-to-analog converter generates a modulated baseband signal at 50 MHz which is upconverted to the transducer resonance frequency through an LO-mixer. The transduced optical signal is detected on the HSPD and downconverted into the baseband by the LO-mixer. **b.** Pulsed phonon dynamics with coherent and thermal driving with equal γ_m. **c.** Transduced signal modulation fitted to the rise and decay of a mechanical mode with a coherent drive (Eq. (5.15)).

a narrowband device with operating frequency $\omega_m/(2\pi) \approx 4.3\,\mathrm{GHz}$, the transmission's carrier wave must also be in the GHz frequency range. To synthesize the microwave input signal, we thus use a combination of a digital-to-analog converter (QM OPX) which generates a gated baseband signal at $f_{IF} = 50\,\mathrm{MHz}$ which is upconverted to the transducer operating frequency by an LO-mixer (QM Octave). The mixing is optimized to output a single signal centered at the transducer mechanical frequency together with any modulation imparted on the input IF signal (Fig. 5.6a).

The square microwave pulses used as input to the electromechanical port of the transducer can be treated similarly to the input in Sec. 5.4.1; however, stationary signals cannot be assumed for fast pulses, so we must instead consider the transducer in the time domain. We start from the relation used for calculating the phonon dynamics under thermal driving (Eq. (B.18)). Instead of a thermal drive, we now assume a pulsed classical microwave drive $\hat{b}_{\mathrm{in},\mu}(t) = \sqrt{\Phi_{\mathrm{in},\mu}}\exp(-i\omega_\mu t)$ coupling through $\sqrt{\gamma_\mu}$ during the pulse time $t \in \{0, T_p\}$. If we assume that the classical drive is strong enough to dominate over other input channels, we can

solve (B.18) directly to obtain

$$\hat{b}(t) = e^{-\chi_{\mathrm{m}}^{-1}(0)t}\left[\chi_{\mathrm{m}}(\omega_\mu)\sqrt{\gamma_\mu \Phi_{\mathrm{in},\mu}}\left(e^{\chi_{\mathrm{m}}^{-1}(\omega_\mu)t} - 1\right) + \hat{b}(0)\right], \tag{5.14}$$

valid for $t \in \{0, T_{\mathrm{p}}\}$ where $\chi_{\mathrm{m}}^{-1}(\omega_\mu) = -i(\omega_\mu - \omega_{\mathrm{m}}) + \gamma_{\mathrm{m}}/2$. Now, if the time between pulses is $\gg \gamma_{\mathrm{m}}^{-1}$, we can assume $\hat{b}(0)$ to be a thermal state with no correlation to the microwave drive. Therefore, by setting $\omega_\mu = \omega_{\mathrm{m}}$, we get

$$n_{\mathrm{m}}(t) = \langle \hat{b}^\dagger(t)\hat{b}(t)\rangle = n_{\mathrm{i}} e^{-\gamma_{\mathrm{m}} t} + n_{\mathrm{f}}\left(1 - e^{-\gamma_{\mathrm{m}} t/2}\right)^2, \tag{5.15}$$

where $n_{\mathrm{i}} = \langle \hat{b}^\dagger(0)\hat{b}(0)\rangle$ and $n_{\mathrm{f}} = 4\gamma_\mu \Phi_{\mathrm{in},\mu}/\gamma_{\mathrm{m}}^2$. (5.15) notably differs from the expression for thermal driving (Eq. (4.5)) which we compare in Fig. 5.6b.

As in Sec. 5.4.1, we have that the driven transducer imparts a signal on the reflected optical field which can be measured with the HSPD. When omitting the thermomechanical sideband, we can approximate the detected optical field amplitude as a sum of the reflected pump and the transduced sideband. In a rotating frame, we can express this as

$$\alpha_{\mathrm{det}} = \alpha_{\mathrm{pump}} + \alpha_{\mathrm{trans}}(t) e^{\pm i\omega_{\mathrm{m}} t}, \tag{5.16}$$

for some classical and constant pump amplitude α_{pump} and modulated transduced field amplitude $\alpha_{\mathrm{trans}}(t)$. The measured HSPD beat note at ω_{m} is thus proportional to $2\mathrm{Re}\{\alpha_{\mathrm{pump}}\alpha_{\mathrm{trans}}(t)\exp(\pm i\omega_{\mathrm{m}} t)\}$. Now, the magnitude of the transduced amplitude is the square root of the photon flux in the sideband leading to

$$|\alpha_{\mathrm{trans}}(t)| \propto \sqrt{\gamma_{\mathrm{om}}\eta_{\mathrm{o}} n_{\mathrm{m}}(t)} \tag{5.17}$$

When demodulating the signal back to the baseband, we thus expect a signal amplitude proportional to $\sqrt{n_{\mathrm{m}}(t)}$. When fitting the demodulated pulses in the time domain, we indeed find good agreement with (5.15) for a γ_{m} which is consistent with the experiments in Sec. 5.4.1 (Fig. 5.6c).

CHAPTER 6

Conclusion & Future outlook

During the course of this thesis work, we developed a novel class of release-free OMCs, took the first steps in properly understanding their tolerance to laser-induced thermal noise, and integrated them into a release-free piezo-optomechanical microwave-to-optical transducer architecture.

The design process laid out in Paper A and Chapter 3 of this thesis led to the fabrication of both SOI and SOS release-free OMCs. These first-generation devices showed promising optomechanical properties with coupling rates in the range of $g_{\mathrm{om}}/(2\pi) \approx 500\,\mathrm{kHz}$ and internal optical quality factors that optimally exceeded $500 \cdot 10^3$. At the time of publication of Paper A, their performance made the release-free OMC the first sideband-resolved nanoscale silicon optomechanical system with a device architecture not reliant on device-layer suspension. The optomechanical waveguide simulations laid out in Sec. 3.1.3 present a design process for using pinch-style mechanical modes to achieve efficient optomechanical coupling in a general release-free waveguide system. In this thesis, these waveguides were primarily implemented in linear optomechanical crystal cavities, but the design also supports other geometries such as ring resonators which could be further explored in future work [87].

With the achieved device properties, we studied optomechanical phenomena such as thermomechanical scattering, EIT and optomechanical backaction. In room-temperature studies, we readily achieve C_{om} ap-

proaching 1 with a blue-detuned pump laser causing self-sustained oscillations in the mechanical mode. The strong thermal anchoring of the release-free design makes the devices significantly more robust to thermo-optic nonlinear shifting. For photon occupancies yielding $C_{\mathrm{om}} \approx 1$ at room temperature, the nonlinear thermal shift can be below one optical FWHM for SOI – and potentially even lower for SOS – making release-free OMCs interesting for applications relying on stable phonon lasing (Fig. 4.9). One such application could be all-optical up- and down-conversion of baseband signals for communication protocols such as 3GPP 5G [71, 72].

The thermal properties of both suspended and release-free OMC devices fabricated on different platforms were characterized in Paper B and Chapter 4 of this thesis. The devices were studied at 10 mK using a quantum-limited measurement system based on single-photon counting. Apart from superior thermo-optic robustness for both room- and cryogenic temperatures, the release-free devices showed exceptional resilience to continuous-wave laser-induced thermal noise. For backaction-free resonant pumping, release-free devices tolerate greater than 30 dB higher input powers at a thermal phonon occupancy of 1 compared to a high Q_{m} suspended device. However, stronger noise-scaling with applied power and a lower zero-point optomechanical cooperativity limits this advantage for high-power off-resonant pumping.

Despite the exceptional noise performance of the release-free devices at low input powers, a continuous-wave quantum cooperativity far exceeding 1 is still out of reach. In pulsed operation, the release-free devices benefit from their fast relaxation (γ_0) and low steady-state noise; however, a high γ_0 is also problematic as it affects device heating rates. Despite this, we measure an SOI release-free OMC and find average pulse noise $n_{\mathrm{avg}} < 0.5$ for 100 ns pulses with 5 % optomechanical scattering probability at 100 kHz repetition rate. Time-resolved waveform analysis of the measured pulses reveals that the average noise is limited by a slowly decaying contribution to the thermal noise which does not follow decay dynamics set by the mechanical linewidth. Further investigation of thermal noise dynamics in release-free SOS and fast-decaying suspended devices shows similar decay dynamics for thermal phonon occupancies $n_{\mathrm{m}} \lesssim 1$. The origin of this noise contribution is not yet resolved but might be tied to slowly decaying TLS present in amorphous material regions in native oxides, around material interfaces, and at etched surfaces [16, 123, 97].

Identifying and removing the slowly decaying noise source is one of the primary objectives for future investigations of noise properties of the release-free devices. This will have significance to both future release-free and suspended devices as both suffered this limit in the studies presented in this thesis. A major part of this work is to properly understand the material composition of the devices. Material studies using transmission electron microscopy (TEM) could reveal the effect of plasma etch damage and the material composition around silicon-sapphire material interfaces. These regions with a potentially high level of material disorder could host long-lived TLS affecting the mechanical decay [141, 148]. A complete removal of the slow noise decay would allow the release-free device presented in Paper B to operate at $n_{\mathrm{avg}} \approx 0.2$ at $R = 500\,\mathrm{kHz}$. This is on par with state-of-the-art 2D OMCs [28] making release-free OMCs highly applicable in near-term quantum optomechanical protocols [24, 50, 25].

Among devices benefiting from a possible reduction in noise are piezo-optomechanical quantum transducers of which a first-generation release-free specimen was presented in Paper C. The measured electromechanical decay rate $\gamma_\mu/(2\pi) \approx 58\,\mathrm{Hz}$ was significantly lower than expected from simulation but would still be viable for near-term quantum protocols. With the measured electromechanical interaction rate, we estimate that Rabi-swapping to a $525\,\Omega$ impedance qubit would be enabled for intrinsic mechanical decay $< 3\,\mathrm{MHz}$ – a level that was readily displayed in cryogenic environments for the release-free OMCs presented in this thesis. However, whether mechanical losses in this range can be expected for the more complex transducer system remains to be investigated.

With the goal of displaying distant quantum entanglement in the microwave domain using the low-noise and low-loss propagation of optical fibers, the next step for the release-free piezo-optomechanical transducer is clear. Full integration of the transducer coupled to qubits [43, 44] or high-impedance resonators [45, 143, 46, 47, 85] appears within reach, although not without significant experimental challenges. The silicon-on-sapphire transducer design presented in Ref. [83] would allow for integration of low-loss microwave circuitry in close proximity to the transducer device due to sapphire's low microwave loss tangent [149]. Together with gap-engineered qubits more resilient to light [150], the release-free transducer is well positioned for pulsed quantum experiments with high repetition rate. However, fidelity would be impaired by the slowly decaying noise sources identified in this thesis. Dealing with this excess noise

will significantly improve the prospects of quantum microwave-to-optical transduction within the release-free architecture.

Taken together, this thesis represents the release-free silicon optomechanical crystal's first steps toward technological application. The increased thermal anchoring and firmer structural support expand silicon optomechanics' versatility toward applications with demand for low noise, high optical powers, thermal and physical robustness, or where waveguide suspension is simply not viable. Through the added piezoelectric coupling, the release-free architecture gains an electro-optic interface with applications in both classical and quantum technology. With a potential for increased noise robustness, we look toward a future with imaginable progress in field-defining experiments such as entangling microwave and optical photons [47], remote microwave entanglement [42], qubit readout and control [44] and optical resource state generation [151].

CHAPTER 7

Summary of papers

Paper A

Johan Kolvik, Paul Burger, Joey Frey, Raphaël Van Laer, "Clamped and sideband-resolved optomechanical crystals", *Optica* **10**, 913-916, June, 2023.

In this paper we introduced the concept of the *release-free* optomechanical crystal. We discussed the device's working principles and presented simulations of both unit cells and full optomechanical crystals. In addition, we fabricated and performed room temperature measurements on a specimen of the release-free devices on the silicon-on-insulator material platform. The device showed promising optomechanical properties with internal optical quality factor of $240 \cdot 10^3$, mechanical quality factor of 850, and optomechanical coupling $g_{\mathrm{om}}/(2\pi) = 500\,\mathrm{kHz}$. To our knowledge, this was the first sideband-resolved release-free silicon optomechanical system at the time of publication.

My contribution: I contributed to the description of the working principle of the device. I ran waveguide and unit cell simulations, fabricated the devices, and performed measurements. I wrote the paper with help from co-authors.

Paper B

Johan Kolvik, Paul Burger, David Hambraeus, Trond H. Haug, Joey Frey, Mads. B. Kristensen, Raphaël Van Laer, "Optomechanical crystal in light-resilient quantum ground state", 10.48550/arXiv.2510.15724, October, 2025.
Manuscript submitted.

In this study, we conducted cryogenic optomechanical studies on the device from Paper A and compared them to a suspended nanobeam optomechanical crystal. We found that the release-free optomechanical crystal was exceptionally stable to the thermo-optic effect compared to the suspended device, both at room temperature and at cryogenic temperatures. In addition, we measured laser-induced thermal noise occupation with a continuous wave pump and found that the release-free device tolerated more than 30 dB higher intracavity optical energy compared to the suspended device when operated below 1 noise phonon. In pulsed operation, we measured average noise occupancy < 0.5 phonons for a 100 ns pulse train with 0.5 % scattering probability run at 100 kHz. We concluded that this noise was limited by a slowly decaying component of the thermal noise.

My contribution: I fabricated the devices. I built the optical measurement setup including filtered single-photon detection. I performed the experiments, analyzed the results, and wrote the paper.

Paper C

Paul Burger, Joey Frey, **Johan Kolvik**, Raphaël Van Laer, "Release-free electro-optomechanical crystal modulator", *Optics Letters* **51**, 3886-3889, July, 2026.

Building on the design for the release-free optomechanical crystal, we here presented a design of a full release-free piezo-optomechanical transducer. The device was fabricated on the silicon-on-insulator platform with micro-transfer-printed lithium niobate for piezoelectric interaction. The device could therefore be actuated with both optics and microwaves that coupled to the device through a $50\,\Omega$ microwave feedline. We performed room temperature measurements and measured microwave-to-optical transduction in both continuous wave and pulsed experiments. With optomechanical coupling rate $g_{\mathrm{om}}/(2\pi) = 130\,\mathrm{kHz}$ and electromechanical decay rate $\gamma_\mu/(2\pi) = 58\,\mathrm{Hz}$, the device did not reach the performance expected from simulation. The overall transduction was thus limited by the electromechanical coupling which was in turn limited by impedance mismatch to the $50\,\Omega$ feedline. In future measurements, proper integration with a high impedance resonator or a qubit would allow for Rabi swapping for achievable mechanical losses.

My contribution: I contributed to the description of the device's working principles. I contributed to the continuous wave measurements and supervised pulsed measurements. I provided theory for the pulsed measurements.

APPENDIX A

Supplementary Brillouin scattering theory

In Sec. 2.2, we present a condensed version of the derivation of the Brillouin scattering coupled mode equations (CME) (Eqs. (2.11)-(2.13)). In this appendix, we provide additional details on arguments and assumptions that were left out in the main text.

A.1 Amplitude envelope operators

The final CMEs (Eqs. (2.11)-(2.13)) are expressed in terms of amplitude envelope operators for the ingoing modes. These describe the fields' evolution in both time and space, allowing to track amplitude changes as the fields travel in a Brillouin-active waveguide. However, the ingoing Hamiltonians are formulated using wavenumber decomposition Eq. (2.7) and thus require a change of variables. We achieve the appropriate change of variables using a Fourier transform over the spatial coordinate

$$\begin{aligned} \hat{a}_{nk}(t) &= \frac{1}{\sqrt{2\pi}} \int \mathrm{d}z \hat{a}_n(z,t) \exp(-i(k-k_n)), \\ \hat{b}_{mq}(t) &= \frac{1}{\sqrt{2\pi}} \int \mathrm{d}z \hat{b}_m(z,t) \exp(-i(q-q_m)). \end{aligned} \tag{A.1}$$

Using this transform, we have defined $\hat{a}_n(z,t)$ ($\hat{b}_m(z,t)$) as the annihilation operator for photons (phonons) in mode n (m) at position z along the waveguide. An additional feature to this transform is that we can

see the new operators as classical wave amplitudes. Note that we here also introduced the additional variables k_n and q_m which we take as the center for each mode's wavenumber distribution. The assumed extent of this distribution will be important for the last steps of the derivation. The new field operators naturally also obey commutator relations

$$\begin{aligned}[\hat{a}_n(z,t), \hat{a}^\dagger_{n'}(z,t)] &= \delta_{nn'}\delta(z-z'),\\ [\hat{b}_m(z,t), \hat{b}^\dagger_{m'}(z,t)] &= \delta_{mm'}\delta(z-z'),\end{aligned} \tag{A.2}$$

A.2 Full scattering dynamics

We continue the derivation toward the final CMEs by inserting the real-space decomposition (Eqs. (2.7), (A.1)) into the Hamiltonians (Eqs. (2.9), (2.10)) and finally derive the dynamics with Eq. (2.5). Before proceeding however, some things must be noted:

1. The optomechanical Hamiltonians are nonlinear in the optical field $\vec{E}$ and naturally lead to products $\hat{a}_n\hat{a}_{n'}, \hat{a}^\dagger_n\hat{a}^\dagger_{n'}$. These terms are assumed not capable of efficiently driving the mechanics and are removed in the so-called rotating wave approximation (RWA).

2. A stricter form of the RWA is also applied when removing terms such as $\hat{a}^\dagger_n\hat{a}_{n'}\hat{b}^\dagger_m$ where $\hat{a}^\dagger_n\hat{a}_{n'}$ and $\hat{b}^\dagger_m$ are assumed to co-rotate at the mechanical frequency.

3. The modal distribution in momentum space for $\hat{a}_{nk}$ and $\hat{b}_{mq}$ is assumed to be sharply centered around k_n and q_m such that the transverse mode profiles $\vec{E}_{nk}$, $\vec{u}_{mq}$ can be assumed constant for all relevant k, q. This allows for $\int \mathrm{d}k \hat{a}_{nk}\vec{E}_{nk} = \vec{E}_{nk_n}\int \mathrm{d}k \hat{a}_{nk}$ and similar operations.

4. The dispersions ω_{nk} and Ω_{mq} are assumed to be small over the scale of the mechanical frequency such that when Taylor expanded as functions of wavenumber around k_n and q_m, only zeroth and first order terms are kept.

With the above assumptions, the ingoing Hamiltonians assume the forms

$$\begin{aligned}
\hat{H}_{\mathrm{EM}}(t) &= \sum_n \int \mathrm{d}z \hat{a}_n^\dagger(z,t)\hbar(\omega_{nk_n} - iv_n\partial_z)\hat{a}_n(z,t) \\
\hat{H}_{\mathrm{M}}(t) &= \sum_m \int \mathrm{d}z \hat{b}_m^\dagger(z,t)\hbar(\Omega_{mq_m} - iv_m\partial_z)\hat{b}_m(z,t) \\
\hat{H}_{\mathrm{OM}}(t) &= \sum_{nn'm} \hbar g_{nn'm} \int \mathrm{d}z \hat{a}_n^\dagger(z,t)\hat{a}_{n'}(z,t)\hat{b}_m(z,t) \\
&\qquad \times \exp[i(k_{n'} + q_m - k_n)z] + \mathrm{h.c.},
\end{aligned} \tag{A.3}$$

where $v_n = \partial_k \omega_{nk}|_{k=k_n}$ ($v_m = \partial_q \Omega_{mq}|_{q=q_m}$) is the photonic (phononic) group velocity of mode n (m) at the center wavenumber k_n (q_m). The factor $g_{nn'm} = g^{(\mathrm{MB})}_{nn'm} + g^{(\mathrm{PE})}_{nn'm}$ is the optomechanical overlap integral and describes the strength of the three-wave interaction between modes $nn'm$. The interested reader can find the full expressions of the overlap integrals in Ref.[5] or App. B. In addition, we have that the interaction contains an explicit momentum conservation in the factor $\exp[i(k_{n'} + q_m - k_n)z]$ which is crucial for this work.

With the full Hamiltonians expressed in the correct field operators, we are now ready to apply Eq. (2.5) to derive the dynamics. The result is two coupled equations describing the dynamics of the envelopes

$$\begin{aligned}
\partial_t \hat{a}_n + v_n\partial_z\hat{a}_n &= -i\omega_{nk_n}\hat{a}_n - i\sum_{n'm} g_{nn'm} \\
&\qquad \times \left[\hat{a}_{n'}\hat{b}_m e^{i(k_{n'}+q_m-k_n)z} + \hat{a}_{n'}\hat{b}_m^\dagger e^{i(k_{n'}-q_m-k_n)z}\right], \\
\partial_t \hat{b}_m + v_m\partial_z\hat{b}_m &= -i\Omega_{mq_m}\hat{b}_m - i\sum_{nn'} g_{nn'm}\hat{a}_{n'}^\dagger\hat{a}_n e^{i(k_{n'}-q_m-k_n)z}.
\end{aligned} \tag{A.4}$$

The above equations describe the total interaction between any combination of two optical (n, n') mode and one acoustic mode (m). However, as mention in the main text, this is commonly reduced to consider only one such three-wave interaction where the optical modes are distinguished into pump (p) and Stokes (s) fields. By assuming a phase-matched interaction ($k_p = k_s + q_m$) and renormalizing the field operators into flux units through

$$\begin{aligned}
\hat{a}_n &\to \sqrt{v_n}\hat{a}_n, \\
\hat{b}_m &\to \sqrt{v_m}\hat{b}_m,
\end{aligned} \tag{A.5}$$

we can rewrite Eqs. (A.4) into those presented as Eqs. (2.11)-(2.13):

$$v_{\mathrm{p}}^{-1}\partial_t\hat{a}_{\mathrm{p}} + \partial_z\hat{a}_{\mathrm{p}} = -ik_{\mathrm{p}}\hat{a}_{\mathrm{p}} - i\tilde{g}_0\hat{a}_{\mathrm{s}}\hat{b}_{\mathrm{m}}, \tag{A.6}$$

$$v_{\mathrm{s}}^{-1}\partial_t\hat{a}_{\mathrm{s}} \pm \partial_z\hat{a}_{\mathrm{s}} = -ik_{\mathrm{s}}\hat{a}_{\mathrm{s}} - i\tilde{g}_0\hat{a}_{\mathrm{p}}\hat{b}_{\mathrm{m}}^{\dagger}, \tag{A.7}$$

$$v_{\mathrm{m}}^{-1}\partial_t\hat{b}_{\mathrm{m}} \pm \partial_z\hat{b}_{\mathrm{m}} = -iq_{\mathrm{m}}\hat{b}_{\mathrm{m}} - i\tilde{g}_0\hat{a}_{\mathrm{p}}\hat{a}_{\mathrm{s}}^{\dagger}, \tag{A.8}$$

where the renormalized vacuum coupling rate $\tilde{g}_0$ now appears in all equations due to g_{ijk} being symmetric in its first two indices. Lastly, we note that the above CMEs do not include losses. To properly account for those, a coupling to Markovian thermal baths is required in the interaction-free Hamiltonians (Eq. (2.9)) this is treated properly in the section on cavity optomechanics (Sec. 2.3).

Lastly, we comment on the Brillouin gain $\mathcal{G}$ which is a common metric for the effectiveness of the Brillouin interaction in waveguide systems. In the limit of an undepleted pump, $\mathcal{G}$ describes the power amplification experienced by the Stokes wave per waveguide distance traveled and pump power ($[\mathcal{G}] = (\mathrm{Wm})^{-1}$). When mechanical losses are introduced in terms of the power loss per meter α_{m}, the Brillouin gain can be calculated as

$$\mathcal{G} = \frac{4|\tilde{g}_0|^2}{\hbar\omega_{\mathrm{p}}\alpha_{\mathrm{m}}}, \tag{A.9}$$

where ω_{p} is the angular frequency of the pump light.

APPENDIX B

Supplementary derivations

B.1 Mathematical conventions

Here we state the mathematical conventions we use for all derivations in this thesis.

The first important convention we use is the symmetric Fourier transform for quantum mechanical operators:

$$\begin{aligned}\hat{a}(\omega) =& \frac{1}{\sqrt{2\pi}} \int \hat{a}(t) e^{i\omega t} \mathrm{d}t, \\ \hat{a}^\dagger(\omega) =& \frac{1}{\sqrt{2\pi}} \int \hat{a}^\dagger(t) e^{i\omega t} \mathrm{d}t,\end{aligned} \tag{B.1}$$

which gives $\hat{a}^\dagger(\omega) = [\hat{a}(-\omega)]^\dagger$. Using this convention, we can use the time domain thermal bath correlation functions (2.22) to define the bath correlation functions in the frequency domain

$$\begin{aligned}\langle \hat{a}_{\mathrm{in,e/i}}(\omega') \hat{a}^\dagger_{\mathrm{in,e/i}}(\omega) \rangle &= \delta(\omega + \omega'), \\ \langle \hat{a}^\dagger_{\mathrm{in,e/i}}(\omega') \hat{a}_{\mathrm{in,e/i}}(\omega) \rangle &= 0, \\ \langle \hat{b}_{\mathrm{in},0}(\omega') \hat{b}^\dagger_{\mathrm{in},0}(\omega) \rangle &= (n_0 + 1)\delta(\omega + \omega'), \\ \langle \hat{b}^\dagger_{\mathrm{in},0}(\omega') \hat{b}_{\mathrm{in},0}(\omega) \rangle &= n_0 \delta(\omega + \omega').\end{aligned} \tag{B.2}$$

We move on to define the spectral density of an operator $\hat{a}(\omega)$ through

the Wiener–Khinchin theorem

$$S_{\hat{a}}(\omega) = \int \langle \hat{a}^\dagger(t)\hat{a}(t+\tau)\rangle e^{i\omega\tau} \mathrm{d}\tau. \tag{B.3}$$

For stationary process' $\hat{a}(t)$, we can then use Eq. (B.1) to define the spectral density as a function of the Fourier transformed operators

$$S_{\hat{a}}(\omega) = \int \langle \hat{a}^\dagger(\omega')\hat{a}(\omega)\rangle \mathrm{d}\omega'. \tag{B.4}$$

Finally, we get the equal-time number operator for a stationary process through the same Eq. (B.1) convention as:

$$\langle \hat{a}^\dagger(t)\hat{a}(t)\rangle = \frac{1}{2\pi}\int S_{\hat{a}}(\omega)\mathrm{d}\omega. \tag{B.5}$$

B.2 Solutions to the cavity optomechanical CMEs

The cavity optomechanical CMEs (Eqs. (2.21)) are derived in Sec 2.3 and can be solved for the ingoing quantum mechanical mode operators. For a sideband-resolved system, we can use the RWA when $|\Delta| \sim \omega_\mathrm{m}$. This divides the solution into two branches with simplified dynamics. We note that in limiting cases such as sideband cooling to the quantum ground state, the RWA removes effects such as the backaction limit. Therefore one must proceed with caution when invoking the RWA. However, the RWA is valid for all applications in this thesis if not otherwise stated.

In the following solutions, we also introduce the mechanical coupling to the hot bath described in Sec. 4.1.2. For red detuning, i.e. $\Delta \sim -\omega_\mathrm{m}$, the solution to the CMEs is obtained as:

$$\hat{a}(\omega) = \frac{-iG_\mathrm{om}\sum_{k=0,\mathrm{p}}\sqrt{\gamma_k}\hat{b}_{\mathrm{in},k}(\omega) + \chi_\mathrm{m}^{-1}(\omega)\sum_{l=\mathrm{e,i}}\sqrt{\kappa_l}\hat{a}_{\mathrm{in},l}(\omega)}{\chi_\mathrm{o}^{-1}(\omega)\chi_\mathrm{m}^{-1}(\omega) + G_\mathrm{om}^2}, \tag{B.6}$$

$$\hat{b}(\omega) = \frac{-iG_\mathrm{om}\sum_{l=\mathrm{e,i}}\sqrt{\kappa_l}\hat{a}_{\mathrm{in},l}(\omega) + \chi_\mathrm{o}^{-1}(\omega)\sum_{k=0,\mathrm{p}}\sqrt{\gamma_k}\hat{b}_{\mathrm{in},k}(\omega)}{\chi_\mathrm{o}^{-1}(\omega)\chi_\mathrm{m}^{-1}(\omega) + G_\mathrm{om}^2}. \tag{B.7}$$

When the laser is tuned to the blue motional sideband, i.e. $\Delta \sim \omega_\mathrm{m}$, the

solution instead comes out as

$$\hat{a}(\omega) = \frac{-iG_{\mathrm{om}} \sum_{k=0,\mathrm{p}} \sqrt{\gamma_k}\hat{b}^{\dagger}_{\mathrm{in},k}(\omega) + \chi^{*-1}_{\mathrm{m}}(-\omega) \sum_{l=\mathrm{e,i}} \sqrt{\kappa_l}\hat{a}_{\mathrm{in},l}(\omega)}{\chi^{-1}_{\mathrm{o}}(\omega)\chi^{*-1}_{\mathrm{m}}(-\omega) - G^2_{\mathrm{om}}}, \tag{B.8}$$

$$\hat{b}(\omega) = \frac{-iG_{\mathrm{om}} \sum_{l=\mathrm{e,i}} \sqrt{\kappa_l}\hat{a}^{\dagger}_{\mathrm{in},l}(\omega) + \chi^{*-1}_{\mathrm{o}}(-\omega) \sum_{k=0,\mathrm{p}} \sqrt{\gamma_k}\hat{b}_{\mathrm{in},k}(\omega)}{\chi^{*-1}_{\mathrm{o}}(-\omega)\chi^{-1}_{\mathrm{m}}(\omega) - G^2_{\mathrm{om}}}. \tag{B.9}$$

In the above we have that $\chi_{\mathrm{o}}(\omega) = [-i(\omega + \Delta) + \kappa/2]^{-1}$ and $\chi_{\mathrm{m}}(\omega) = [-i(\omega - \omega_{\mathrm{m}}) + (\gamma_0 + \gamma_{\mathrm{p}})/2]^{-1}$ are the optical and mechanical susceptibilities and $G_{\mathrm{om}} = \sqrt{n_{\mathrm{c}}}g_{\mathrm{om}}$ is the effective optomechanical coupling under optical driving. These equations reduce to the standard equations of motion for two independent driven harmonic oscillators when $G_{\mathrm{om}} \to 0$.

B.3 Brillouin gain in 2D simulations

As mentioned in App. A, the Brillouin gain is a common metric to benchmark Brillouin active waveguides. In this section, we present how we calculate Brillouin gain in waveguide simulations gain using the finite-element tool COMSOL.

The results of a 2D OMW cross-section simulation is given by the electromagnetic fields $\vec{E}, \vec{D}, \vec{H}$ associated with the pump (p) and Stokes (s) waves, along with the mechanical displacement field $\vec{u}$. The pump and Stokes optical fields can be of the same or differing spatial modes giving intramodal or intermodal scattering, respectively. In addition, the propagation direction of the pump and Stokes waves must be considered which dictates whether forward stimulated Brillouin scattering (FSBS) or backward stimulated Brillouin scattering (BSBS) gain will be computed. To yield the field for a counter-propagating Stokes wave, one simply takes the conjugate $\vec{E}_{\mathrm{s}} \to \vec{E}^{*}_{\mathrm{s}}$. Lastly, correct Brillouin gain is only calculated when the wavevector of the mechanical mode obeys momentum conservation (Eq. (3.1)) which differs depending on the propagation direction of the Stokes wave. This must be considered when running the mechanical simulation.

Given the resulting fields and modal frequencies (ω_{m} for mechanics and $\omega_{\mathrm{p}} \approx \omega_{\mathrm{s}} := \omega_{\mathrm{o}}$ for optics) we calculate the coupling based on the theory of Brillouin scattering (Sec. 2.2). For this typ of 2D OMW simulation, the Brillouin gain $\mathcal{G}$ normalized by the mechanical quality factor

Q_m is given by [152]

$$\frac{\mathcal{G}}{Q_\mathrm{m}} = \frac{\omega_\mathrm{o}}{2\omega_\mathrm{m}^2 m_\mathrm{eff} P_\mathrm{p} P_\mathrm{s}} \left| I_\mathrm{MB}^{(2\mathrm{D})} + I_\mathrm{PE}^{(2\mathrm{D})} \right|^2, \tag{B.10}$$

where $[\mathcal{G}] = (\mathrm{Wm})^{-1}$. In this equation, we have introduced the effective mass

$$m_\mathrm{eff} = \int \mathrm{d}^2\vec{r}\varrho \left|\vec{u}(\vec{r})\right|^2, \tag{B.11}$$

which is given in the unit kg/m when $\vec{u}$ is normalized $\vec{u} \to \vec{u}/(\max|\vec{u}|)$. In addition, the optical power in mode n is calculated through

$$P_n = \frac{1}{2}\int \left(\vec{E}_n \times \vec{H}_n\right) \cdot \mathrm{d}\vec{A}, \tag{B.12}$$

where $\mathrm{d}\vec{A}$ is the vector-valued area element which is parallel with the propagation of the pump. Lastly, the optomechanical overlap integrals are two-dimensional versions of the interaction Hamiltonians (Eq. (2.10))

$$\begin{aligned} I_\mathrm{PE}^{(2\mathrm{D})} =& -\frac{\varepsilon_0 n^4}{2}\int \mathrm{d}^2\vec{r} E_{\mathrm{s}i}^*(\vec{r},t) E_{\mathrm{p}j}(\vec{r},t) p_{ijkl} S_{kl}(\vec{r},t), \\ I_\mathrm{MB}^{(2\mathrm{D})} =& \frac{1}{2}\int_C \mathrm{d}\vec{r}[\hat{n}\cdot\vec{u}(\vec{r},t)] \times \Big[(\varepsilon_a - \varepsilon_b)\vec{E}_{\mathrm{p}\parallel}^*(\vec{r},t)\cdot\vec{E}_{\mathrm{s}\parallel}(\vec{r},t) \\ & -(\varepsilon_a^{-1} - \varepsilon_b^{-1})\vec{D}_{\mathrm{p}\perp}^*(\vec{r},t)\cdot\vec{D}_{\mathrm{s}\perp}(\vec{r},t)\Big], \end{aligned} \tag{B.13}$$

where the photoelasticity integral is taken over the waveguide cross-sectional area while radiation pressure is calculated on the 1-dimensional waveguide boundary C.

B.4 Unit cell optomechanical coupling

To calculate unit cell optomechanical coupling in an OMW unit cell simulation, we take a combined approach from Sec. B.3 and Ref. [112]. We start from the perturbation theory definition of the optomechanical coupling and divide the coupling into moving boundary (MB) and photoelasticity (PE) contributions,

$$g_\mathrm{om,uc} = -\frac{\omega_\mathrm{o}}{2} x_\mathrm{zpf} \frac{I_\mathrm{MB}^{(\mathrm{uc})} + I_\mathrm{PE}^{(\mathrm{uc})}}{\mathcal{E}}, \tag{B.14}$$

where we in three dimensions define

$$x_\mathrm{zpf} = \sqrt{\frac{\hbar}{2 m_\mathrm{eff}\omega_\mathrm{m}}}, \quad m_\mathrm{eff} = \int \mathrm{d}^3\vec{r}\varrho|\vec{u}|^2, \quad \mathcal{E} = \int \mathrm{d}^3\vec{r}\vec{E}\cdot\vec{D}. \tag{B.15}$$

We note that as in Sec. B.3, we here use a normalized version of the displacement $\vec{u} \to \vec{u}/(\max|\vec{u}|)$. In this case, unit cell overlap integrals $I_{\mathrm{MB}}^{(\mathrm{uc})}$ and $I_{\mathrm{PE}}^{(\mathrm{uc})}$ are given as

$$\begin{aligned} I_{\mathrm{PE}}^{(\mathrm{uc})} &= -\frac{\varepsilon_0 n^4}{2}\int \mathrm{d}^3\vec{r} E_{si}^*(\vec{r},t) E_{\mathrm{p}j}(\vec{r},t) p_{ijkl} S_{kl}(\vec{r},t), \\ I_{\mathrm{MB}}^{(\mathrm{uc})} &= \frac{1}{2}\int_C \mathrm{d}^2\vec{r}\,[\hat{n}\cdot\vec{u}(\vec{r},t)] \times \Big[(\varepsilon_a-\varepsilon_b)\vec{E}_{\mathrm{p}\parallel}^*(\vec{r},t)\cdot\vec{E}_{\mathrm{s}\parallel}(\vec{r},t) \\ &\qquad -(\varepsilon_a^{-1}-\varepsilon_b^{-1})\vec{D}_{\mathrm{p}\perp}^*(\vec{r},t)\cdot\vec{D}_{\mathrm{s}\perp}(\vec{r},t)\Big]. \end{aligned} \tag{B.16}$$

These overlaps closely resemble the optomechanical interaction Hamiltonians (Eq. (2.10)). However, we point out two important details: (1) the units of the overlap integrals are J/m due to the normalized displacement $\vec{u}$, and (2) where the Hamiltonians consider the total electric field, the unit cell overlap only treats discrete modes. The last point allows for different types of Brillouin interactions to be considered by choosing different combinations of $\vec{E}_{\mathrm{p}}$ and $\vec{E}_{\mathrm{s}}$. Just as in Sec. B.3, we can thus calculate coupling for forward/backward and intra-/intermodal scattering.

B.5 Phonon dynamics with thermal drive

In Sec. 4.1.4, we present the thermal phonon dynamics that we use to fit the time evolution of thermal phonon occupation under optical pumping in Paper B. In this appendix, we briefly motivate Eq. (4.5) from the cavity optomechanical CMEs.

We first assume a red detuning for the optical pulse and start from the mechanical solution to the linearized CMEs (Eq. (B.7)). We now note that $\hat{b}(\omega)$ should be sharply located around ω_{m} with a bandwidth set by the total mechanical decay γ_{m}. Since $\gamma_{\mathrm{m}} \ll \kappa$ for all experiments in this thesis, we can adiabatically eliminate the optical cavity by taking $\chi_{\mathrm{o}}(\omega)|_{\omega\approx\omega_{\mathrm{m}}} \approx 2/\kappa$. The resulting expression for $\hat{b}(\omega)$ thus becomes:

$$\hat{b}(\omega) \approx \frac{-i\frac{2G_{\mathrm{om}}}{\kappa}\sum_{l=\mathrm{e,i}}\sqrt{\kappa_l}\hat{a}_{\mathrm{in},l}(\omega) + \sum_{k=0,\mathrm{p}}\sqrt{\gamma_k}\hat{b}_{\mathrm{in},k}(\omega)}{-i(\omega-\omega_{\mathrm{m}}) + (\gamma_0+\gamma_{\mathrm{p}}+\gamma_{\mathrm{om}})/2}. \tag{B.17}$$

When taken back to the time domain, this describes the dynamics:

$$\dot{\hat{b}} = -\left(i\omega_{\mathrm{m}} + \frac{\gamma_{\mathrm{m}}}{2}\right)\hat{b} + \sum_{k=0,\mathrm{p}}\sqrt{\gamma_k}\hat{b}_{\mathrm{in},k} - i\frac{2G_{\mathrm{om}}}{\kappa}\sum_{l=\mathrm{e,i}}\sqrt{\kappa_l}\hat{a}_{\mathrm{in},l}, \tag{B.18}$$

where $\gamma_\mathrm{m} = \gamma_0 + \gamma_\mathrm{p} + \gamma_\mathrm{om}$ while pumping red. Solving this equation in the time domain for a sharp optical pulse starting at $t = 0$ yields

$$\hat{b}(t) = e^{-(i\omega_\mathrm{m}+\gamma_\mathrm{m}/2)t}\left[\hat{b}(0) + \int_0^t d\tau e^{(i\omega_\mathrm{m}+\gamma_\mathrm{m}/2)\tau} \times \left(\sum_{k=0,\mathrm{p}} \sqrt{\gamma_k}\hat{b}_{\mathrm{in},k} - i\frac{2G_\mathrm{om}}{\kappa}\sum_{l=\mathrm{e,i}} \sqrt{\kappa_l}\hat{a}_{\mathrm{in},l}\right)\right]. \tag{B.19}$$

From here, it is possible to calculate the average mechanical occupation $n_\mathrm{m}(t) = \langle\hat{b}^\dagger(t)\hat{b}(t)\rangle$. By assuming that the baths are mutually uncorrelated and taking bath correlation functions (2.22), we get:

$$n_\mathrm{m}(t) = \frac{\gamma_0 n_0 + \gamma_\mathrm{p} n_\mathrm{p}}{\gamma_\mathrm{m}}(1 - e^{-\gamma_\mathrm{m}t}) + \langle\hat{b}^\dagger(0)\hat{b}(0)\rangle e^{-\gamma_\mathrm{m}t}, \tag{B.20}$$

where n_p is the occupation of the hot bath. Note that the effect of the optical input operators has been eliminated here due their assumed vacuum states. By defining $n_\mathrm{f} = (\gamma_0 n_0 + \gamma_\mathrm{p} n_\mathrm{p})/\gamma_\mathrm{m}$ and $n_\mathrm{i} = \langle\hat{b}^\dagger(0)\hat{b}(0)\rangle$ we arrive at the final expression:

$$n_\mathrm{m}(t) = n_\mathrm{f} + (n_\mathrm{i} - n_\mathrm{f})(1 - e^{-\gamma_\mathrm{m}t}). \tag{B.21}$$

We end by noting that in the case for blue detuning, the input optical operators will not vanish in (B.20) due to vacuum fluctuations. In this case, we instead get a final occupation

$$n_\mathrm{f} = \frac{\gamma_0 n_0 + \gamma_\mathrm{p} n_\mathrm{p} + \gamma_\mathrm{om}}{\gamma_\mathrm{m}} \tag{B.22}$$

which is significant in cases where $\gamma_\mathrm{om} \gtrsim \gamma_0 n_0 + \gamma_\mathrm{p} n_\mathrm{p}$. However, this is most likely not true for any experiment in this thesis.

Bibliography

[1] Menabrea, L. F. Sketch of the Analytical Engine Invented by Charles Babbage. *Scientific Memoirs* **3**, 666–731 (1843).

[2] Wang, C. *et al.* Micromachined Accelerometers with Sub-µg/sqrt(Hz) Noise Floor: A Review. *Sensors* **20**, 4054 (2020).

[3] Lee, X., Wang, C., Luo, Z. & Li, S. Optical design of a new folding scanning system in MEMS-based lidar. *Optics & Laser Technology* **125**, 106013 (2020).

[4] Nguyen, C. T.-C. MEMS-based RF channel selection for true software-defined cognitive radio and low-power sensor communications. *IEEE Communications Magazine* **51**, 110–119 (2013).

[5] Eggleton, B. J., Steel, M. J. & Poulton, C. G. *Brillouin Scattering Part 1*, vol. 109 of *Semiconductors and semimetals* (Elsevier, 2022).

[6] Ippen, E. & Stolen, R. Stimulated Brillouin scattering in optical fibers. *Applied Physics Letters* **21**, 539–541 (1972).

[7] Fischer, L. *et al.* Brillouin–Mandelstam scattering-based cooling of traveling acoustic waves from cryogenic temperatures. *Optics Letters* **51**, 121–124 (2026).

[8] Seiderer, S. *et al.* Giant Brillouin gain in frozen CS2 capillaries. Preprint at http://arxiv.org/abs/2603.25472 (2026).

[9] Kippenberg, T. J. & Vahala, K. J. Cavity Opto-Mechanics. *Optics Express* **15**, 17172–17205 (2007).

[10] Kleckner, D. & Bouwmeester, D. Sub-kelvin optical cooling of a micromechanical resonator. *Nature* **444**, 75–78 (2006).

[11] Gröblacher, S. *et al.* Demonstration of an ultracold micro-optomechanical oscillator in a cryogenic cavity. *Nature Physics* **5**, 485–488 (2009).

[12] Armani, D. K., Kippenberg, T. J., Spillane, S. M. & Vahala, K. J. Ultra-high-Q toroid microcavity on a chip. *Nature* **421**, 925–928 (2003).

[13] Schliesser, A., Del'Haye, P., Nooshi, N., Vahala, K. J. & Kippenberg, T. J. Radiation Pressure Cooling of a Micromechanical Oscillator Using Dynamical Backaction. *Physical Review Letters* **97**, 243905 (2006).

[14] Gorodetksy, M. L., Schliesser, A., Anetsberger, G., Deleglise, S. & Kippenberg, T. J. Determination of the vacuum optomechanical coupling rate using frequency noise calibration. *Optics Express* **18**, 23236–23246 (2010).

[15] Teufel, J. D. *et al.* Sideband cooling of micromechanical motion to the quantum ground state. *Nature* **475**, 359–363 (2011).

[16] Borselli, M., Johnson, T. J. & Painter, O. Measuring the role of surface chemistry in silicon microphotonics. *Applied Physics Letters* **88**, 131114 (2006).

[17] Aspelmeyer, M., Kippenberg, T. J. & Marquardt, F. Cavity optomechanics. *Reviews of Modern Physics* **86**, 1391–1452 (2014).

[18] Painter, O., Vučkovič, J. & Scherer, A. Defect modes of a two-dimensional photonic crystal in an optically thin dielectric slab. *Journal of the Optical Society of America B* **16**, 275 (1999).

[19] Eichenfield, M., Chan, J., Camacho, R. M., Vahala, K. J. & Painter, O. Optomechanical crystals. *Nature* **462**, 78–82 (2009).

[20] Chan, J. *et al.* Laser cooling of a nanomechanical oscillator into its quantum ground state. *Nature* **478**, 89–92 (2011).

[21] Qiu, L., Shomroni, I., Seidler, P. & Kippenberg, T. J. Laser cooling of a nanomechanical oscillator to Its zero-point energy. *Physical Review Letters* **124**, 173601 (2020).

[22] Riedinger, R. *et al.* Remote quantum entanglement between two micromechanical oscillators. *Nature* **556**, 473–477 (2018).

[23] del Pino, J., Slim, J. J. & Verhagen, E. Non-Hermitian chiral phononics through optomechanically induced squeezing. *Nature* **606**, 82–87 (2022).

[24] Riedinger, R. *et al.* Non-classical correlations between single photons and phonons from a mechanical oscillator. *Nature* **530**, 313–316 (2016).

[25] Chen, L. *et al.* Low-noise optomechanical single phonon-photon conversion for quantum networks. *Nature Communications* **17**, 1187 (2026).

[26] Chan, J., Safavi-Naeini, A. H., Hill, J. T., Meenehan, S. & Painter, O. Optimized optomechanical crystal cavity with acoustic radiation shield. *Applied Physics Letters* **101**, 081115 (2012).

[27] Leijssen, R., La Gala, G. R., Freisem, L., Muhonen, J. T. & Verhagen, E. Nonlinear cavity optomechanics with nanomechanical thermal fluctuations. *Nature Communications* **8**, ncomms16024 (2017).

[28] Mayor, F. M. *et al.* High photon-phonon pair generation rate in a two-dimensional optomechanical crystal. *Nature Communications* **16**, 2576 (2025).

[29] Miller, D. A. Attojoule Optoelectronics for Low-Energy Information Processing and Communications. *Journal of Lightwave Technology* **35**, 346–396 (2017).

[30] Zou, C.-L. *et al.* Microwave-optical quantum frequency conversion. *Optica* **8**, 1050–1064 (2021).

[31] Wang, C. *et al.* High-efficiency microwave-optical quantum transduction based on a cavity electro-optic superconducting system with long coherence time. *npj Quantum Information* **8**, 149 (2022).

[32] Sahu, R. *et al.* Quantum-enabled operation of a microwave-optical interface. *Nature Communications* **13**, 1276 (2022).

[33] Adak, P. C. *et al.* Microwave-to-optical transduction using magnon-exciton coupling in a layered antiferromagnet. Preprint at http://arxiv.org/abs/2604.03441 (2026).

[34] Tu, H.-T. *et al.* High-efficiency coherent microwave-to-optics conversion via off-resonant scattering. *Nature Photonics* **16**, 291–296 (2022).

[35] Borówka, S., Pylypenko, U., Mazelanik, M. & Parniak, M. Continuous wideband microwave-to-optical converter based on room-temperature Rydberg atoms. *Nature Photonics* **18**, 32–38 (2024).

[36] Rochman, J., Xie, T., Bartholomew, J. G., Schwab, K. C. & Faraon, A. Microwave-to-optical transduction with erbium ions coupled to planar photonic and superconducting resonators. *Nature Communications* **14**, 1153 (2023).

[37] Li, F. *et al.* Pump Free Microwave-Optical Quantum Transduction. Preprint at http://arxiv.org/abs/2512.05096 (2025).

[38] Goto, K., Kurokawa, H., Kosaka, H. & Koshino, K. Microwave-to-Optical Quantum Transduction via Defect-Mediated Scattering in Diamond. Preprint at http://arxiv.org/abs/2605.15988 (2026).

[39] Safavi-Naeini, A. H., Van Thourhout, D., Van Laer, R. & Baets, R. Controlling phonons and photons at the wavelength scale: integrated photonics meets integrated phononics. *Optica* **6**, 213–232 (2019).

[40] Saadatmand, S. *et al.* Superconducting qubits in the millions: The potential and limitations of modularity. *Physical Review Applied* **25**, 064038 (2026).

[41] Krinner, S. *et al.* Engineering cryogenic setups for 100-qubit scale superconducting circuit systems. *EPJ Quantum Technology* **6**, 2 (2019).

[42] Krastanov, S. *et al.* Optically Heralded Entanglement of Superconducting Systems in Quantum Networks. *Physical Review Letters* **127**, 040503 (2021).

[43] Mirhosseini, M., Sipahigil, A., Kalaee, M. & Painter, O. Superconducting qubit to optical photon transduction. *Nature 2020 588:7839* **588**, 599–603 (2020).

[44] van Thiel, T. C. *et al.* Optical readout of a superconducting qubit using a piezo-optomechanical transducer. *Nature Physics* **21**, 401–405 (2025).

[45] Jiang, W. *et al.* Optically heralded microwave photon addition. *Nature Physics* **19**, 1423–1428 (2023).

[46] Meesala, S. *et al.* Non-classical microwave–optical photon pair generation with a chip-scale transducer. *Nature Physics* **20**, 871–877 (2024).

[47] Meesala, S. *et al.* Quantum entanglement between optical and microwave photonic qubits. *Physical Review X* **14**, 031055 (2024).

[48] Patel, R. N., Sarabalis, C. J., Jiang, W., Hill, J. T. & Safavi-Naeini, A. H. Engineering Phonon Leakage in Nanomechanical Resonators. *Physical Review Applied* **8**, 041001 (2017).

[49] Ren, H. *et al.* Two-dimensional optomechanical crystal cavity with high quantum cooperativity. *Nature Communications 2020 11:1* **11**, 1–10 (2020).

[50] Fiaschi, N. *et al.* Optomechanical quantum teleportation. *Nature Photonics* **15**, 817–821 (2021).

[51] Kepler, J. *De cometis libelli tres* (Andreæ Apergeri, 1619).

[52] Kini Manjeshwar, S. *et al.* Suspended photonic crystal membranes in AlGaAs heterostructures for integrated multi-element optomechanics. *Applied Physics Letters* **116**, 264001 (2020).

[53] Chen, Y. Macroscopic quantum mechanics: theory and experimental concepts of optomechanics. *Journal of Physics B: Atomic, Molecular and Optical Physics* **46**, 104001 (2013).

[54] Lorenzo, L. A. D. & Schwab, K. C. Superfluid optomechanics: coupling of a superfluid to a superconducting condensate. *New Journal of Physics* **16**, 113020 (2014).

[55] Agarwal, G. S. & Jha, S. S. Theory of optomechanical interactions in superfluid He. *Physical Review A* **90**, 023812 (2014).

[56] Korsch, A. R., Fiaschi, N. & Gröblacher, S. Phononic crystals in superfluid thin-film helium. *Physical Review Applied* **22**, L041005 (2024).

[57] Griffiths, D. J. *Introduction to Electrodynamics* (Cambridge University Press, 2023).

[58] Auld, B. A. *Acoustic Fields and Waves in Solids* (Krieger Pub Co, 1990).

[59] Van Laer, R. *Light-Sound Interaction in Nanoscale Silicon Waveguides.* Ph.D. thesis, Ghent (2016).

[60] Advanced Composite Solar Sail System (ACS3) - NASA. Preprint at https://www.nasa.gov/mission/acs3/.

[61] Volpe, G. *et al.* Roadmap for optical tweezers. *Journal of Physics: Photonics* **5**, 022501 (2023).

[62] Brillouin, L. Diffusion de la lumière et des rayons X par un corps transparent homogène - Influence de l'agitation thermique. *Annales de Physique* **9**, 88–122 (1922).

[63] Mandelstam, L. I. Light scattering by inhomogeneous media. *Zh. Russ. Fiz-Khim. Ova* **58**, 146 (1926).

[64] Wolff, C., Smith, M. J. A., Stiller, B. & Poulton, C. G. Brillouin scattering—theory and experiment: tutorial. *JOSA B* **38**, 1243–1269 (2021).

[65] Kippenberg, T. J., Rokhsari, H., Carmon, T., Scherer, A. & Vahala, K. J. Analysis of Radiation-Pressure Induced Mechanical Oscillation of an Optical Microcavity. *Physical Review Letters* **95**, 033901 (2005).

[66] Cryer-Jenkins, E. A. *et al.* Second-order coherence across the Brillouin lasing threshold. *Optica* **10**, 1432–1438 (2023).

[67] Brubaker, B. M. *et al.* Optomechanical Ground-State Cooling in a Continuous and Efficient Electro-Optic Transducer. *Physical Review X* **12**, 021062 (2022).

[68] Clerk, A. A. Introduction to quantum noise, measurement, and amplification. *Reviews of Modern Physics* **82**, 1155–1208 (2010).

[69] Van Laer, R., Baets, R. & Van Thourhout, D. Unifying Brillouin scattering and cavity optomechanics. *Physical Review A* **93**, 053828 (2016).

[70] Cohen, J. D. *et al.* Phonon counting and intensity interferometry of a nanomechanical resonator. *Nature* **520**, 522–525 (2015).

[71] Mercadé, L., Morant, M., Griol, A., Llorente, R. & Martínez, A. Photonic Frequency Conversion of OFDM Microwave Signals in a Wavelength-Scale Optomechanical Cavity. *Laser & Photonics Reviews* **15**, 2100175 (2021).

[72] Fito, V. *et al.* Experimental Evaluation of All-Optical Up- and Down-Conversion of 3GPP 5G NR Signals Using an Optomechanical Crystal Cavity Frequency Comb. *Journal of Lightwave Technology* **42**, 6825–6831 (2024).

[73] Wendt, A. *et al.* An electrically injected solid-state surface acoustic wave phonon laser. *Nature* **649**, 597–603 (2026).

[74] Weis, S. *et al.* Optomechanically induced transparency. *Science* **330**, 1520–1523 (2010).

[75] Fleischhauer, M., Imamoglu, A. & Marangos, J. P. Electromagnetically induced transparency: Optics in coherent media. *Reviews of Modern Physics* **77** (2005).

[76] Qiu, L. *et al.* Floquet dynamics in the quantum measurement of mechanical motion. *Physical Review A* **100**, 053852 (2019).

[77] Qiu, L. *et al.* Dissipative Quantum Feedback in Measurements Using a Parametrically Coupled Microcavity. *PRX Quantum* **3**, 020309 (2022).

[78] Sonar, S. *et al.* High-efficiency low-noise optomechanical crystal photon-phonon transducers. *Optica* **12**, 99–104 (2025).

[79] Kippenberg, T. J., Schliesser, A. & Gorodetsky, M. L. Phase noise measurement of external cavity diode lasers and implications for optomechanical sideband cooling of GHz mechanical modes. *New Journal of Physics* **15**, 015019 (2013).

[80] Safavi-Naeini, A. H. *et al.* Laser noise in cavity-optomechanical cooling and thermometry. *New Journal of Physics* **15**, 035007 (2013).

[81] Sarabalis, C. J., Hill, J. T. & Safavi-Naeini, A. H. Guided acoustic and optical waves in silicon-on-insulator for Brillouin scattering and optomechanics. *APL Photonics* **1**, 071301 (2016).

[82] Sarabalis, C. J., Dahmani, Y. D., Patel, R. N., Hill, J. T. & Safavi-Naeini, A. H. Release-free silicon-on-insulator cavity optomechanics. *Optica* **4**, 1147–1150 (2017).

[83] Burger, P., Frey, J., Kolvik, J., Hambraeus, D. & Van Laer, R. Design of a release-free piezo-optomechanical quantum transducer. *APL Photonics* **10**, 010801 (2025).

[84] Burger, P., Frey, J., Kolvik, J., Kristensen, M. B. & Laer, R. V. Release-free electro-optomechanical crystal modulator. *Optics Letters* **51**, 3886–3889 (2026).

[85] Frey, J., Burger, P., Haug, T. H., Kolvik, J. & Laer, R. V. Release-free phononic crystal with strong microwave coupling. Preprint at http://arxiv.org/abs/2607.29666 (2026).

[86] Li, Y. Three-dimensional elastic–plastic lattice-spring model based on sapphire crystal structure and its application to impact characterisation studies. *International Journal of Solids and Structures* **306**, 113097 (2025).

[87] Chen, I.-T. *et al.* Intermodal microwave-to-optical transduction using silicon-on-sapphire optomechanical ring resonator. *Science Advances* **11**, eadx6485 (2025).

[88] Rakich, P. T., Reinke, C., Camacho, R., Davids, P. & Wang, Z. Giant enhancement of stimulated Brillouin scattering in the subwavelength limit. *Physical Review X* **2**, 011008 (2012).

[89] Qiu, W. *et al.* Stimulated Brillouin scattering in nanoscale silicon step-index waveguides: a general framework of selection rules and calculating SBS gain. *Optics Express, Vol. 21, Issue 25, pp. 31402-31419* **21**, 31402–31419 (2013).

[90] Qiu, W., Rakich, P. T., Soljacic, M. & Wang, Z. Stimulated brillouin scattering in slow light waveguides. Preprint at http://arxiv.org/abs/1210.0738 (2012).

[91] Safavi-Naeini, A. H. *et al.* Electromagnetically induced transparency and slow light with optomechanics. *Nature* **472**, 69–73 (2011).

[92] Eggleton, B. J., Poulton, C. G., Rakich, P. T., Steel, M. J. & Bahl, G. Brillouin integrated photonics. *Nature Photonics 2019 13:10* **13**, 664–677 (2019).

[93] Iyer, A., Kandel, Y. P., Xu, W., Nichol, J. M. & Renninger, W. H. Coherent optical coupling to surface acoustic wave devices. *Nature Communications* **15**, 3993 (2024).

[94] Kolvik, J., Burger, P., Frey, J. & Van Laer, R. Clamped and sideband-resolved silicon optomechanical crystals. *Optica* **10**, 913–916 (2023).

[95] Safavi-Naeini, A. H. & Painter, O. Optomechanical Crystal Devices. In Aspelmeyer, M., Kippenberg, T. J. & Marquardt, F. (eds.) *Cavity Optomechanics: Nano- and Micromechanical Resonators Interacting with Light*, 195–231 (Springer, Berlin, Heidelberg, 2014).

[96] Safavi-Naeini, A. H., Painter, O. & Watson, T. J. Design of optomechanical cavities and waveguides on a simultaneous bandgap phononic-photonic crystal slab. *Optics Express, Vol. 18, Issue 14, pp. 14926-14943* **18**, 14926–14943 (2010).

[97] Luo, Y. *et al.* Millisecond coherence times in gigahertz-frequency mechanical oscillators. *Nature Physics* 1–7 (2026).

[98] Laermer, F. & Schilp, A. Method of anisotropically etching silicon. Patent US5501893A (US), Robert Bosch GmbH (1996).

[99] Asano, T. *et al.* Photonic crystal nanocavity with a Q factor exceeding eleven million. *Optics Express, Vol. 25, Issue 3, pp. 1769-1777* **25**, 1769–1777 (2017).

[100] MacCabe, G. S. *et al.* Nano-acoustic resonator with ultralong phonon lifetime. *Science* **370**, 840–843 (2020).

[101] Dussart, R., Tillocher, T., Lefaucheux, P. & Boufnichel, M. Plasma cryogenic etching of silicon: from the early days to today's advanced technologies. *Journal of Physics D: Applied Physics* **47**, 123001 (2014).

[102] Jansen, H., Gardeniers, H., De Boer, M., Elwenspoek, M. & Fluitman, J. A survey on the reactive ion etching of silicon in microtechnology. *Journal of Micromechanics and Microengineering* **6**, 14 (1996).

[103] Detter, X. *et al.* Impact of chemistry on profile control of resist masked silicon gates etched in high density halogen-based plasmas. *Journal of Vacuum Science & Technology B: Microelectronics and Nanometer Structures Processing, Measurement, and Phenomena* **21**, 2174 (2003).

[104] Zivari, A. *et al.* A single-phonon directional coupler. *Optica Quantum* **3**, 445–451 (2025).

[105] Mehran, M., Sanaee, Z., Abdolahad, M. & Mohajerzadeh, S. Controllable silicon nano-grass formation using a hydrogenation assisted deep reactive ion etching. *Materials Science in Semiconductor Processing* **14**, 199–206 (2011).

[106] Patel, R. N. *Control and tomography of phonons in cavity optomechanical nanostructures.* Ph.D. thesis, Stanford (2020).

[107] Benedikovic, D. *et al.* High-efficiency single etch step apodized surface grating coupler using subwavelength structure. *Laser & Photonics Reviews* **8**, L93–L97 (2014).

[108] McKenna, T. P. *et al.* Cryogenic packaging of an optomechanical crystal. *Optics Express, Vol. 27, Issue 20, pp. 28782-28791* **27**, 28782–28791 (2019).

[109] Marchetti, R., Lacava, C., Carroll, L., Gradkowski, K. & Minzioni, P. Coupling strategies for silicon photonics integrated chips [Invited]. *Photonics Research* **7**, 201–239 (2019).

[110] Gröblacher, S., Hill, J. T., Safavi-Naeini, A. H., Chan, J. & Painter, O. Highly efficient coupling from an optical fiber to a nanoscale silicon optomechanical cavity. *Applied Physics Letters* **103**, 181104 (2013).

[111] MacCabe, G. S. *Phonon Dynamics and Damping in Three-Dimensional Acoustic Bandgap Cavity-Optomechanical Resonators.* Ph.D. thesis, California Institute of Technology (2019).

[112] Chan, J. *Laser cooling of an optomechanical crystal resonator to its quantum ground state of motion.* Ph.D. thesis, California Institute of Technology (2012).

[113] Probst, S., Song, F. B., Bushev, P. A., Ustinov, A. V. & Weides, M. Efficient and robust analysis of complex scattering data under noise in microwave resonators. *Review of Scientific Instruments* **86**, 024706 (2015).

[114] Tamaki, S., Kristensen, M. B., Martel, T., Braive, R. & Schliesser, A. Two-dimensional gallium phosphide optomechanical crystal in the resolved-sideband regime. *Optics Express* **32**, 48500–48508 (2024).

[115] Jiang, W. *et al.* Lithium niobate piezo-optomechanical crystals. *Optica* **6**, 845–853 (2019).

[116] Xie, T. *et al.* A two-dimensional piezo-optomechanical transducer. Preprint at http://arxiv.org/abs/2607.26161 (2026).

[117] Claps, R., Raghunathan, V., Dimitropoulos, D. & Jalali, B. Influence of nonlinear absorption on Raman amplification in Silicon waveguides. *Optics Express* **12**, 2774–2780 (2004).

[118] Barclay, P. E., Srinivasan, K. & Painter, O. Nonlinear response of silicon photonic crystal microresonators excited via an integrated waveguide and fiber taper. *Optics Express* **13**, 801–820 (2005).

[119] Meenehan, S. M. *et al.* Silicon optomechanical crystal resonator at millikelvin temperatures. *Physical Review A* **90**, 011803 (2014).

[120] Pernice, W. H. P., Schuck, C., Li, M. & Tang, H. X. Carrier and thermal dynamics of silicon photonic resonators at cryogenic temperatures. *Optics Express* **19**, 3290–3296 (2011).

[121] Yang, Y. *et al.* Research on the Evolution of Defects Initiation and the Diffusion of Dopant on the Si/SiO2 Interface. *Advanced Materials Interfaces* **12**, 2400751 (2025).

[122] Poindexter, E. H. *et al.* Electronic traps and Pb centers at the Si/SiO2 interface: Band-gap energy distribution. *Journal of Applied Physics* **56**, 2844–2849 (1984).

[123] Borselli, M., Johnson, T. J., Michael, C. P., Henry, M. D. & Painter, O. Surface encapsulation for low-loss silicon photonics. *Applied Physics Letters* **91**, 131117 (2007).

[124] Zyryanov, P. & Taluts, G. G. On the theory of sound absorption in solids. *J. Exptl. Theoret. Phys. (U.S.S.R.)* **49**, 1326–1330 (1996).

[125] Kolvik, J. *et al.* Optomechanical crystal in light-resilient quantum ground state. Preprint at http://arxiv.org/abs/2510.15724 (2026).

[126] Cahill, D. G. *et al.* Nanoscale thermal transport. *Journal of Applied Physics* **93**, 793–818 (2003).

[127] Cahill, D. G. *et al.* Nanoscale thermal transport. II. 2003–2012. *Applied Physics Reviews* **1**, 011305 (2014).

[128] Chen, G. Non-Fourier phonon heat conduction at the microscale and nanoscale. *Nature Reviews Physics* **3**, 555–569 (2021).

[129] Pobell, F. *Matter and Methods at Low Temperatures* (Springer, Berlin, Heidelberg, 2007).

[130] Bon-Mardion, C. *et al.* Sub-kelvin thermal conductivity of substrates and on-chip routing in quantum integrated systems. Preprint at http://arxiv.org/abs/2605.06146 (2026).

[131] Hao, H.-Y., Neumann, M., Enss, C. & Fleischmann, A. Contactless technique for thermal conductivity measurement at very low temperature. *Review of Scientific Instruments* **75**, 2718–2725 (2004).

[132] Sahling, S., Engert, J., Gladun, A. & Knöner, R. The thermal boundary resistance between sapphire and aluminum monocrystals at low temperature. *Journal of Low Temperature Physics* **45**, 457–469 (1981).

[133] Phillips, W. A. Two-level states in glasses. *Reports on Progress in Physics* **50**, 1657 (1987).

[134] Chen, J., Xu, X., Zhou, J. & Li, B. Interfacial thermal resistance: Past, present, and future. *Reviews of Modern Physics* **94**, 025002 (2022).

[135] Meenehan, S. M. *et al.* Pulsed excitation dynamics of an optomechanical crystal resonator near its quantum ground state of motion. *Physical Review X* **5**, 041002 (2015).

[136] You, M., Lin, Z., Li, X. & Liu, J. Chip-Scale Silicon Ring Resonators for Cryogenic Temperature Sensing. *Journal of Lightwave Technology* **38**, 5768–5773 (2020).

[137] Girardi, M., Helgason, O. B., Lopez-Ortega, C. H., Rebolledo-Salgado, I. & Torres-Company, V. Superefficient microcombs at the wafer level. *Optics Express* **33**, 27451–27460 (2025).

[138] Komma, J., Schwarz, C., Hofmann, G., Heinert, D. & Nawrodt, R. Thermo-optic coefficient of silicon at 1550 nm and cryogenic temperatures. *Applied Physics Letters* **101**, 041905 (2012).

[139] Yu, J., Yuan, S., Gao, J.-Y. & Sun, L. Optical pulse propagation in a Fabry–Perot etalon: analytical discussion. *Journal of the Optical Society of America A* **18**, 2153 (2001).

[140] Natarajan, C. M., Tanner, M. G. & Hadfield, R. H. Superconducting nanowire single-photon detectors: physics and applications. *Superconductor Science and Technology* **25**, 063001 (2012).

[141] Cleland, A. Y., Wollack, E. A. & Safavi-Naeini, A. H. Studying phonon coherence with a quantum sensor. *Nature Communications* **15**, 4979 (2024).

[142] Jiang, W. *et al.* Efficient bidirectional piezo-optomechanical transduction between microwave and optical frequency. *Nature Communications* **11**, 1166 (2020).

[143] Weaver, M. J. *et al.* An integrated microwave-to-optics interface for scalable quantum computing. *Nature Nanotechnology* **19**, 166–172 (2024).

[144] Zhao, H., Chen, W. D., Kejriwal, A. & Mirhosseini, M. Quantum-enabled microwave-to-optical transduction via silicon nanomechanics. *Nature Nanotechnology* **20**, 602–608 (2025).

[145] Drimmer, M. *Bulk Acoustic Quantum Transduction*. Ph.D. thesis, ETH Zürich (2025).

[146] Zhong, C., Han, X. & Jiang, L. Microwave and Optical Entanglement for Quantum Transduction with Electro-Optomechanics. *Physical Review Applied* **18**, 054061 (2022).

[147] Shi, H. & Zhuang, Q. Overcoming the fundamental limit of quantum transduction via intraband entanglement. *Optica Quantum* **2**, 475 (2024).

[148] Gruenke-Freudenstein, R. G. *et al.* Surface and bulk two-level-system losses in lithium niobate acoustic resonators. *Physical Review Applied* **23**, 064055 (2025).

[149] Deng, H. *et al.* Titanium Nitride Film on Sapphire Substrate with Low Dielectric Loss for Superconducting Qubits. *Physical Review Applied* **19**, 024013 (2023).

[150] McEwen, M. *et al.* Resisting High-Energy Impact Events through Gap Engineering in Superconducting Qubit Arrays. *Physical Review Letters* **133**, 240601 (2024).

[151] Haug, T. H., Kockum, A. F. & Van Laer, R. Heralding entangled optical photons from a microwave quantum processor. *Physical Review Applied* **22**, 034068 (2024).

[152] Van Laer, R., Kuyken, B., Van Thourhout, D. & Baets, R. Interaction between light and highly confined hypersound in a silicon photonic nanowire. *Nature Photonics 2015 9:3* **9**, 199–203 (2015).

Appended papers